PREDICTION OF VELOCITIES WITHIN JETS FORMED BY OVERTOPPING STEEP DAMS

Submitted to
Bureau of Reclamation
Reclamation Service Center
Denver Federal Center
Denver, Colorado 80225

Prepared by
Todd M. Lewis
Steven R. Abt
James F. Ruff

Department of Civil Engineering
Colorado State University
Ft. Collins, Colorado 80523

March 1996

Colorado State University

Engineering Research Center
Foothills Campus
Fort Collins, Colorado 80523
(970) 491-8203
FAX: (970) 491-8462

March 22, 1996

Dr. Rodney J. Wittler
U.S. Bureau of Reclamation
Hydraulic Structures Section
D-3751
P.O. Box 25007
Denver, CO 80401

RE: Report Transmittal

Dear Dr. Wittler:

In accordance with our contractual agreement pertaining to the Dam Foundation Erosion project, transmitted herein are two copies of a report entitled "Prediction of Velocities within Jets Formed by Overtopping Steep Dams" by Lewis et al. Also enclosed is a draft (marked) copy of the manuscript per your request. We welcome your review and comments.

Mr. Lewis and I plan to travel to Reclamation on April 23, 1996 to present the findings of this study to you and the research staff at 9:00 am. Please inform us of any changes.

Do not hesitate to contact me if additional information is needed to complete this phase of contract. Thank you.

Respectfully,

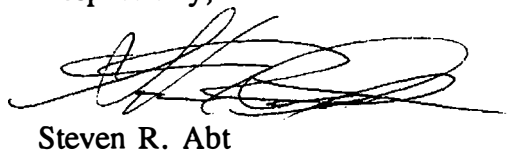

Steven R. Abt
Professor, Director
Hydraulics Laboratory

encl.

ACKNOWLEDGMENTS

Cooperative Agreement 1425-5-FC-81-20350 between the US Bureau of Reclamation and Colorado State University governs funding for the Dam Foundation Erosion research. Funding and technical partners in this multi-year research study include:

- Pacific Gas & Electric Company
- Electric Power Research Institute
- Reclamation Water Technology and Environmental Research Program
- Department of the Interior Dam Safety Program
- Western Area Power Administration
- Golder Associates, Inc.

The Study Team acknowledges Colorado State University and the Colorado Agriculture Experiment Station (Project 1-57151) for their in-kind and financial contributions to the research study.

ABSTRACT

PREDICTION OF VELOCITIES WITHIN JETS FORMED BY OVERTOPPING STEEP DAMS

A method was sought to predict the velocity of a highly turbulent, aerated, broken-up (developed) jet at the point of impact with the plunge pool at the foundation and abutment areas of steep-faced dams. Three techniques were identified to predict jet impact velocities; a technique developed by Ervine and Falvey (1987), a method derived herein based on a dimensional analysis of forces acting on a representative water drop (sphere), and a method formulated through the integration of the differential equations of motion. An experimental facility was constructed to simulate a developed jet from an overtopped, steep-faced dam. Data taken from twenty-seven independent tests were used to evaluate the performance of the three prediction techniques. The dimensional equation impact velocity prediction technique demonstrated good agreement between predicted and observed values. The experimental program validated previous findings that the representative droplet of the jet was approximately 6 mm in diameter. Also, the aerodynamic drag of a fully developed jet must be addressed in a comprehensive analysis. Further, the issuance angle of the jet did not affect impact velocity for angles of zero to thirty degrees from the vertical. The experimental results are presented, along with conclusions and recommendations for further study.

TABLE OF CONTENTS

LIST OF TABLES

LIST OF FIGURES

CHAPTER 1

INTRODUCTION

The stability of dams, particularly when subjected to extreme flood events, is an important factor in preserving the health and safety of the public. Several thousand dam sites in the United States are located immediately upstream of small towns and cities. Dam failure would precipitate an unacceptable loss of life and property.

One of the possible modes of failure for dams is destabilization of the dam at the foundation and abutments areas due to erosion, or scour. Many dams are overtopped during floods. The overtopping flow often results in a jet that impacts the foundation and abutments, dislodging foundation materials and destabilizing the dam. Of 142 dam failures studied in a report by Serafim and Rodrigues (1989), 45 (32%) were due to overtopping. Prevention of dam failure due to overtopping flow is obviously a topic worthy of further research.

Compliance with State and Federal Dam Safety Regulations regarding extreme flood events usually takes two alternate approaches. First, an energy dissipater may be constructed. Examples of energy dissipaters include flip buckets, chute blocks, and hollow jet valves. These structures decrease the amount of kinetic energy in the water, thereby preventing erosion at the foundation areas. The other method of compliance is to allow the dam to overtop. When the dam overtops, an analysis of the potential for erosion

at the dam foundation and abutment areas must be performed. Current methods of predicting the extents of erosion, such as the Veronese method, have a very limited range of applicability and are not valid when applied to dams with hard-rock or cohesive foundation materials. Prediction of the progressive extents of erosion in the foundation and abutment areas below dams requires an understanding of the forces that dislodge and transport foundation materials. The primary force causing displacement and transportation of foundation materials is the velocity of the water column as it impacts the foundation area.

It is necessary to quantify and understand the hydraulics of the water column as it strikes the foundation and abutment areas in order to improve erosion prediction and tracking approaches for overtopping dams. Two distinctly different overtopping scenarios exist. The first is water flowing over the downstream face of the dam, typical of gravity and embankment dams. The second is water flowing over the dam and forming a jet which travels through the air and impinges at the foundation, typical of steep-faced concrete dams.

Two types of jets arise from the second scenario: undeveloped and developed jets. Undeveloped jets consist of a solid core of non-aerated water surrounded by a shell of aerated water. Developed jets consist entirely of a coherent stream of discreet water particles. The solid core of non-aerated water present in undeveloped jets contracts in width as the jet plunges through the air. If the length of fall is sufficient, an undeveloped jet may become a developed jet before striking the foundation and abutment area of a

dam. Both categories of jets are usually turbulent, depending largely on the boundary conditions. The following qualities are attributed to turbulent flows.

- Randomness: Turbulent flows seem irregular, chaotic, and unpredictable.
- Nonlinearity: Turbulent flows are highly nonlinear, which causes the values of nonlinearity parameters such as the Reynolds number to exceed a critical value.
- Diffusivity: Turbulent flows are characterized by a rapid rate of diffusion of momentum and heat.
- Vorticity: Turbulence is characterized by high levels of fluctuating eddies of all sizes. These eddies transfer energy progressively from large to small sized eddies until it can be dissipated effectively by viscous diffusion.
- Dissipation: Once the eddy size of the flow becomes sufficiently small, gradients are wiped out (dissipated) by viscosity. Turbulent flows therefore require a continuous supply of energy to make up for viscous losses.

The objectives of this study are as follows:

1. Develop an equation(s) to predict the velocity of a turbulent, developed jet as it impacts the surface of a plunge pool beneath an overtopping dam.
2. Construct and operate a model of a turbulent, developed jet that simulates an overtopping steep-faced dam.
3. Use data collected from the model to compare actual velocities with those predicted from the equation(s) developed in Objective 1.
4. Modify the equation(s) from Objective 1 to produce results that agree with the experimental data collected in Objective 2.

An extensive review of the available literature focuses on the physical characteristics and processes pertaining to turbulent jets within the context of overtopping dams. A theoretical analysis and derivation leads to a mathematical model for predicting

the impact velocity of a turbulent developed jet at the point of incidence with the plunge pool.

An experimental facility was constructed at the Hydraulics Laboratory of Colorado State University. A testing program using three values of the three primary testing variables: volumetric discharge, vertical plunge length, and emittance angle was conducted for a total of 27 different test configurations. The results of that study are presented herein.

CHAPTER 2

LITERATURE REVIEW

A review of literature regarding the prediction of the velocity profile of a turbulent, developed jet was conducted. Unfortunately, no documented research pertaining to developed jets was found. Instead, documented research on undeveloped jets was cited.

2.1 Overview of Jet Trajectory

The trajectory of the turbulent, undeveloped jet is separated into four distinct zones, each having unique boundary conditions that mandate a different theoretical treatment of the resulting velocity profile. The four zones are the free-fall zone, the free-jet zone, the impingement zone, and the wall-jet zone. Figure 2.1 illustrates these four zones with a frontal view of the entire jet trajectory.

2.2 Free-Fall Zone

The free-fall zone corresponds to the atmospheric portion of the jet trajectory. Coherence, or lack thereof, of the jet during the fall through the atmosphere and

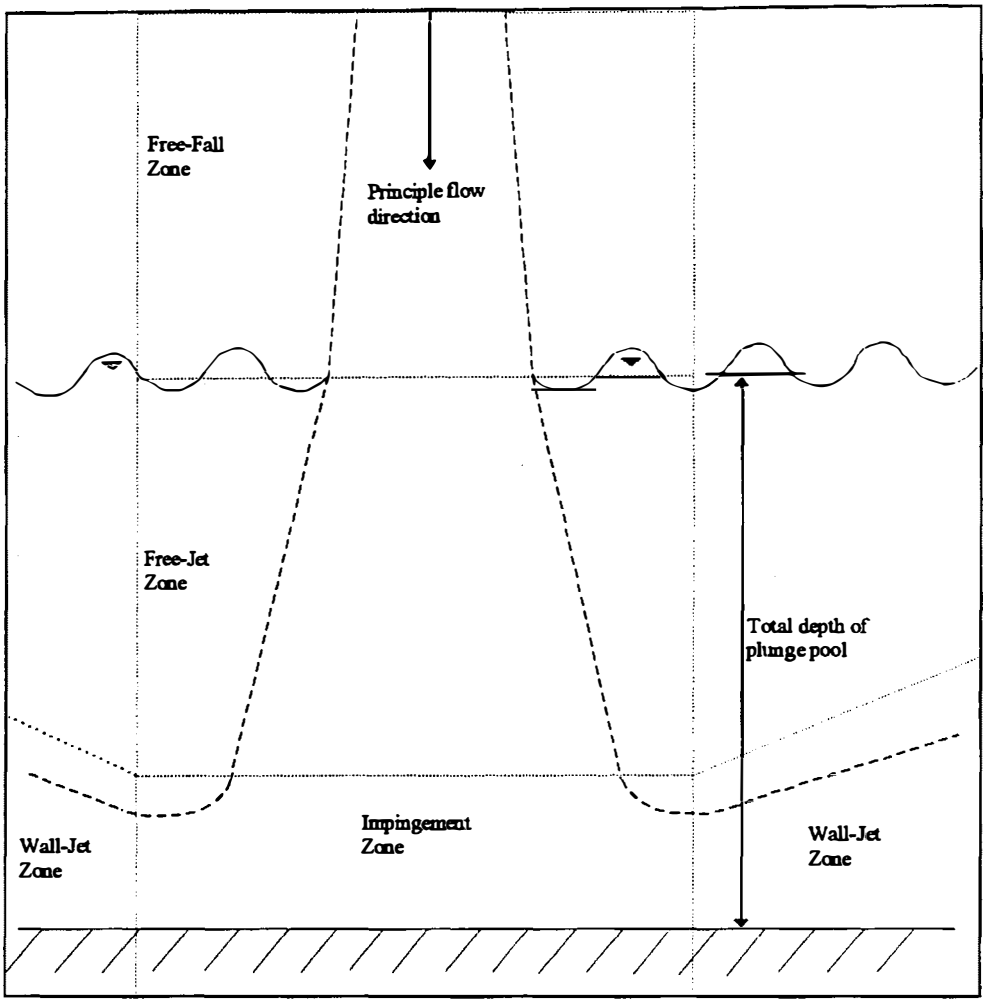

Figure 2.1 Frontal view of jet trajectory delineating flow zones

particularly when striking the water surface helps determine how the impact velocity is predicted, and how the diffusion of the jet in the plunge pool is analyzed. First, the effectiveness of air drag as a decelerating force on the jet increases dramatically as the surface area of falling water increases, causing a corresponding decrease in jet velocity. Second, the non-aerated width of the solid jet core is a crucial boundary condition used in theoretical predictions of velocity in the three ensuing flow zones.

2.2.1 Characteristics of Jet Geometry - Continuous Mass

Ervine and Falvey (1987) examined the entrainment of air and its effect upon turbulent, undeveloped jets through the free-fall zone. They note some of the characteristics of turbulent, undeveloped jets that may effect the velocity distribution within the jet.

a. The aeration capability of turbulent jets varied greatly with the Reynolds number (Re).

b. The surface of the impinging undeveloped jet at the point of contact with the plunge pool does not have a distinct width. Instead an inner core region and an undulating outer region may exist.

c. The undulating outer region may or may not be aerated, and the irregularity of flow in this region will produce surface waves in the plunge pool.

d. The surface waves create a scenario in which well-defined penetrating shear layers cannot exist. The point of origin of the shear layers can vary from instant to instant. This is in sharp contrast to the case of a turbulent jet with a submerged entrance into the plunge pool, where the shear layers and their origin are well-defined.

e. The varying degree of aerated water that is entrained in the pool from the outer region of the plunging jet will cause pressure fluctuations at the bottom of the plunge pool. This creates a situation in which the impingement region will not be steady, but rather, will expand and contract dynamically.

f. So long as the length of fall through the atmosphere was sufficiently small, a solid core of water remained within the center of the jet. This core contains a disproportionately large amount of the total momentum of the jet.

Ervine and Falvey treated the jet in their experiments as a continuous mass, with a solid core carrying the majority of the jet's momentum into the plunge pool. They theorized that air drag had a negligible effect upon the velocity of the solid core jet in the

free-fall zone. Accordingly, they held that the ballistic equations of constant gravitational acceleration were sufficient to describe the velocity of the jet through the atmosphere.

Ervine and Falvey also hypothesized that the width of the solid jet core of the undeveloped jet at the point of contact with the plunge pool surface was the boundary condition that would enable a shift to the consideration of velocity profiles within the pool. This width is analogous to the width of the entrance nozzle in the case of a submerged turbulent jet. Figure 2.2 shows the aforementioned features of Ervine and Falvey's jet in the free-fall zone.

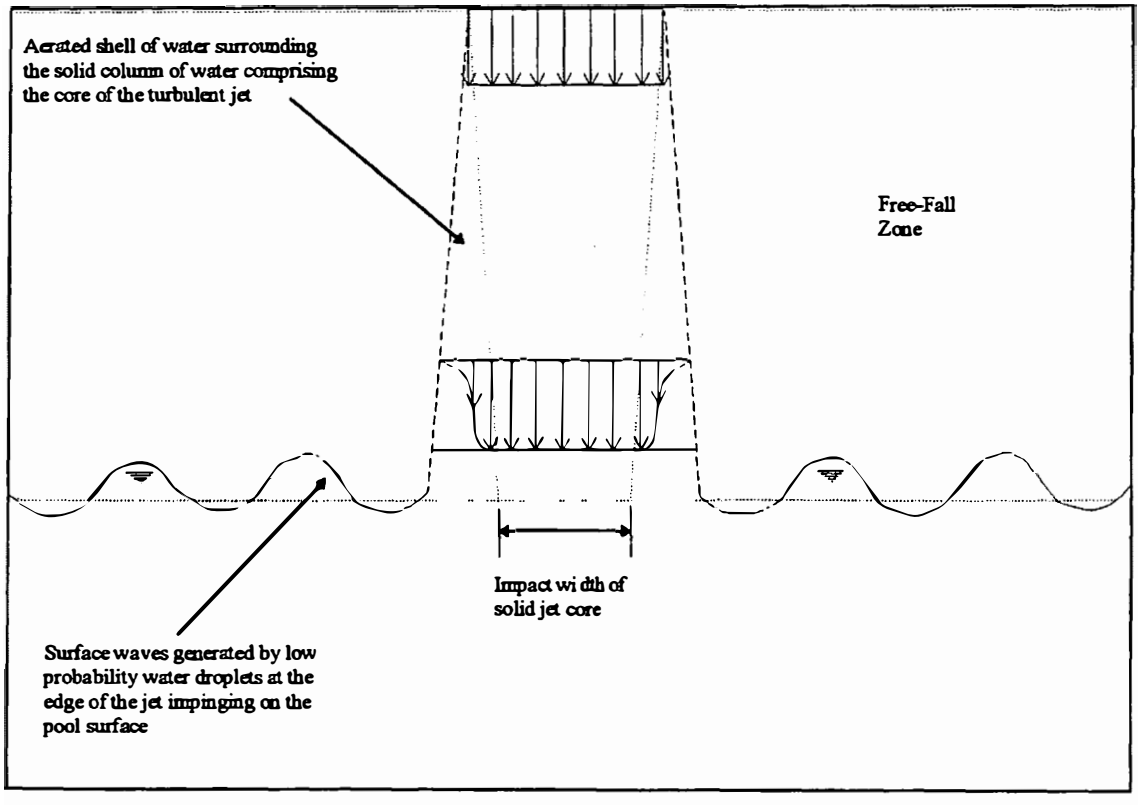

Figure 2.2 Frontal view of jet: free-fall zone

2.2.2 The Ballistic Motion Assumption

If air drag is negligible, as Ervine and Falvey have suggested, the horizontal and vertical components of the jet velocity in the free-fall zone are expressed, respectively, as:

$$V_x = V_o \sin\phi \tag{2.1}$$

and

$$V_y = \left(\sqrt{V_o^2 + 2gy}\right)\cos\phi \tag{2.2}$$

where

V_x = the horizontal velocity component of the jet (L/T),

V_y = the vertical velocity component of the jet (L/T),

V_o = the original velocity of the jet upon discharge (L/T),

ϕ = the angle the trajectory of the jet makes with the vertical (°),

g = acceleration due to gravity (L/T^2), and

y = vertical distance traveled by the jet, measured from discharge (L).

The vector impact velocity at the plunge pool surface is determined by applying the Pythagorean Theorem:

$$V_i = \sqrt{V_y^2 + V_x^2}\Big|_{y=H_d} = \sqrt{V_o^2\left(\cos^2\phi + \sin^2\phi\right) + 2gH_d\cos^2\phi} \tag{2.3}$$

where

H_d = the vertical distance from jet discharge to the pool surface (L), and

V_i = the velocity of the jet at impact with the pool surface (L/T).

Using the trigonometric identity: $\cos^2\phi + \sin^2\phi = 1$ and assuming that ϕ is small, Equation 2.3 can be simplified to:

$$V_i = \sqrt{V_o^2 + 2gH_d} \tag{2.4}$$

which is Ervine and Falvey's estimate of the velocity of the solid core of a turbulent, undeveloped jet when it impacts the surface of the plunge pool.

2.2.3 Characteristics of Jet Geometry - Discrete Water Drops

If the undeveloped jet falls for a sufficient distance, the jet loses its coherence due to air entrainment. Instead of a core of solid water with an aerated "shell" of water around it, the jet becomes a conglomeration of individual water drops, each having separate acceleration vectors. The acceleration of this group of water particles is not constant due to the interactions, namely collisions and splitting, of the particles with each other. The boundary width of the jet at the plunge pool surface is not a solid core in the case of a developed jet, instead, individual water drops strike the water surface like the pellets of a shotgun.

The deceleration caused by air drag becomes a significant accountable factor in the free-fall zone when the jet loses its coherence. In order to account for the effects of air drag, two approaches were taken; a dimensional analysis of the forces acting on a single water particle, and an integration of the differential equations of motion. These approaches are discussed in the following sections.

2.2.4 Incorporation of Air Drag via Dimensional Analysis

A water drop traveling through the air has two significant forces acting upon it, a gravitational force acting vertically downward and an aerodynamic drag force acting opposite to the direction of motion. The aerodynamic drag force can be expressed as:

$$F_d = \frac{1}{2} C_d \rho_a V^2 A \tag{2.5}$$

where

C_d = drag coefficient (nondimensional),

F_d = drag force (ML/T^2),

ρ_a = air density (M/L^3),

V = velocity (L/T), and

A = surface area of object (L^2).

After a dimensional analysis was performed, it appeared reasonable to modify Equation 2.4 by subtracting a term, f, that is a function of the distance traveled, size of drop, and the amount of resistance generated by aerodynamic drag. The general form of the revised equation is:

$$V_i = \sqrt{V_o^2 + 2gH_d} - f \tag{2.6}$$

For dimensional consistency, the drag term must have dimensions of L/T. One possible dimensionally consistent grouping using F_d, H_d, ρ_w, and Vol was found to be:

$$f = \sqrt{\frac{(F_d)(H_d)}{\rho_w (\mathrm{Vol})}} \tag{2.7}$$

where

ρ_w = water density (M/L^3), and

Vol = volume of a representative drop (L^3).

By substituting Equation 2.5 into the drag term, Equation 2.7, the following expression is obtained:

$$f = \sqrt{\frac{\left(\frac{1}{2} C_d \rho_a V^2 A\right)(H_d)}{\rho_w (\text{Vol})}} \tag{2.8}$$

Substituting the geometric formulas for the surface area, $A = \pi d^2$, and the volume, $\text{Vol} = \frac{1}{6}\pi d^3$, of a sphere into Equation 2.8, the following expressed is obtained:

$$f = \sqrt{\frac{\left(\frac{\rho_a}{2} C_d V^2 \pi d^2\right) H_d}{\rho_w \left(\frac{\pi d^3}{6}\right)}} \tag{2.9}$$

where

d = diameter of a sphere having the same volume as a water drop (L).

Simplifying Equation 2.9, we end up with the following expression:

$$f = \sqrt{3 C_d \left(\frac{\rho_a}{\rho_w}\right)\left(\frac{H_d}{d}\right) V^2} \tag{2.10}$$

Substituting the simplified drag term, Equation 2.10, into Equation 2.6 results in an approximation of the velocity of a turbulent, developed jet at the point of incidence with the water surface.

$$V_i = \sqrt{V_o^2 + 2gH_d} - \sqrt{3C_d\left(\frac{\rho_a}{\rho_w}\right)\left(\frac{H_d}{d}\right)V_o^2} \qquad (2.11)$$

Drag coefficients for spheres have been computed experimentally as a function of Reynolds number and are illustrated in Figure 2.3.

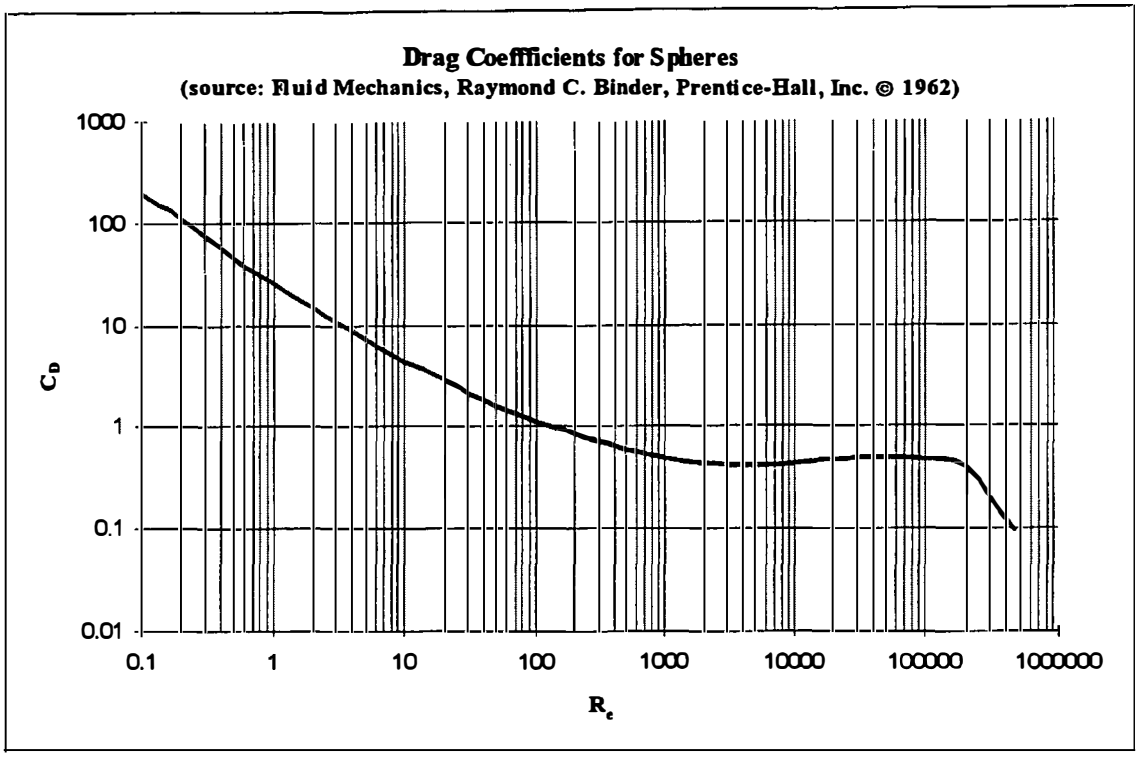

Figure 2.3 Drag coefficients for spheres

2.2.5 Incorporation of Air Drag via Integration of Free-Fall Equations

The drag coefficient is a function of the Reynolds number for rigid bodies. For water drops, the drag coefficient can be greater than that for a rigid sphere because the leading surface of the drop deforms (flattens) as it falls, causing greater drag. In the case

of water drops that deform at high velocities, the drag coefficient depends on the Reynolds number, a ratio of inertial forces to viscous forces, and the Weber number. The Weber number is a ratio of inertial forces to surface tension forces.

One approach that accounts for the deceleration caused by air drag while allowing for drop deformation, is to integrate the component acceleration equations of motion numerically, assuming that the acceleration is constant over small increments of time. An empirically-derived drag coefficient is computed at each time step, allowing the effective drag force to vary over the trajectory of the jet in air.

Seginer (1965) proposed that the drag acceleration could be approximated by a power function for small intervals of the trajectory:

$$a_D \approx C_n V^n \qquad (2.12)$$

where

a_D = acceleration due to aerodynamic drag forces (L/T^2),

V = the instantaneous velocity of the jet (L/T),

n = an experimentally determined exponent (nondimensional), and

C_n = an empirical drag coefficient (L^{1-n}, T^{n-2}).

Seginer then modified the differential equation describing vertical acceleration by subtracting the acceleration due to aerodynamic drag from the gravitational acceleration constant.

$$\frac{dV}{dt} = g - C_n V^n \qquad (2.13)$$

At terminal velocity, $dV/dt = 0$ and C_n is:

$$C_n = \frac{g}{V_T^n} \tag{2.14}$$

where

V_T = terminal velocity of deforming water droplets in air (L/T).

Seginer stated that a value of $n = 2$ would be suitable for predicting the velocity of raindrops and sprinkler drops. However, a method for computing the terminal velocity of falling water drops in air was absent from Seginer's work.

A study by Wang and Pruppacher (1977) addressed the calculation of the terminal velocity of falling water drops. They formulated the following equations from which the terminal velocity can be computed:

$$P = \frac{\sigma_w^3 \rho_a^2}{\mu_a^4 (\rho_w - \rho_a) g} \tag{2.15}$$

$$B_o = \frac{d^2 (\rho_w - \rho_a) g}{\sigma_w} \tag{2.16}$$

$$X = \ln\left(\frac{3}{4} B_o P^{1/6}\right) \tag{2.17}$$

$$Y = b_0 + b_1 X + b_2 X^2 + b_3 X^3 + b_4 X^4 + b_5 X^5 \tag{2.18}$$

$$Re_T = P^{1/6} \exp(Y) \tag{2.19}$$

$$V_T = \frac{\mu_a Re_T}{d \rho_a} \tag{2.20}$$

where

P = Physical property number (nondimensional),

B_o = Bond number (nondimensional),

σ_w = surface tension of water (M/T^2),

μ_a = dynamic viscosity of air (M/LT),

b_0 - b_5 = experimentally derived constants (nondimensional), and

Re_T = the Reynolds number at terminal velocity (nondimensional).

Seginer's differential equation, Equation 2.13, only addressed the vertical motion of water droplets. The more general case was examined by Bernuth and Gilley (1984), who resolved Seginer's differential equation into horizontal and vertical components.

$$\frac{dV_x}{dt} = -C_n V^{n-1} V_x \tag{2.21}$$

$$\frac{dV_y}{dt} = g - C_n V^{n-1} V_y \tag{2.22}$$

Hinkle (1991) showed that Seginer's drag function exponent (n) was not constant. Instead, the exponent was found to vary with both drop size and the ratio of the drop velocity to the terminal velocity, i.e.: $n = f(d, V/V_T)$. A linear regression equation was fit satisfactorily to Hinkle's data in the form:

$$n = b_6 + b_7\left(\frac{V}{V_T}\right) \tag{2.23}$$

where

b_6 - b_7 = experimentally derived constants (nondimensional).

Equations 2.21 and 2.22 can be integrated using numerical techniques to determine the position and velocity of water drops as they deform in air over the entire range of the free-fall zone. One such method is the Euler method, which can be formulated for this scenario by the following equations:

$$V_{x,t+1} = V_{x,t} + \frac{dV_{x,t}}{dt}(\Delta t) \tag{2.24}$$

$$V_{y,t+1} = V_{y,t} + \frac{dV_{y,t}}{dt}(\Delta t) \tag{2.25}$$

$$x_{t+1} = x_t + V_{x,t}(\Delta t) + \frac{1}{2}\frac{dV_{x,t}}{dt}(\Delta t)^2 \tag{2.26}$$

$$y_{t+1} = y_t + V_{y,t}(\Delta t) + \frac{1}{2}\frac{dV_{y,t}}{dt}(\Delta t)^2 \tag{2.27}$$

The results from these studies can be combined into a numerical model for predicting the velocity and trajectory of water drops as they fall through air. An iterative scheme is employed using a small time increment. The iterative process is as follows:

a. Calculate resultant velocity from known velocity components $V = \sqrt{V_x^2 + V_y^2}$,

b. Calculate terminal velocity using Equations 2.15 - 2.20,

c. Calculate n using Equation 2.23,

d. Calculate C_n using Equation 2.14,

e. Calculate the horizontal and vertical acceleration components with Equations 2.21 and 2.22, and

f. Calculate new velocities and coordinate positions using Equations 2.24 - 2.27.

When the vertical position component equals or slightly exceeds the known distance between the jet emitter and the water surface, the iteration is terminated. The instantaneous impact velocity V_i is the velocity of the water drop at this point.

2.3 Free-Jet Zone

The free-jet zone is the region of the turbulent jet trajectory that extends from the surface of the plunge pool to a depth where additional pressure from jet stagnation increases the local pressure above hydrostatic. In this zone, a significant portion of the kinetic energy of the undeveloped jet is translated into turbulence, and finally dissipated as heat. The primary mechanism of energy transfer is viscous shear. The process by which the energy is transferred can best be described as a momentum exchange, with the outer edges of the jet forming a velocity distribution that weakens as it spreads to entrain more water.

2.3.1 The Submerged Free Jet

To study the free-jet zone, it is informative to look at a different type of turbulent jet. A two-dimensional slot jet with a submerged entrance, and an infinite pool in which to diffuse, is similar to the free-jet zone portion of the undeveloped jet trajectory. The submerged free-jet is more easily studied because the geometry of the shear layers that form as the jet diffuses into the surrounding medium remain constant. Once the behavior of the submerged free-jet is understood, it may be possible to determine how the fluctuating conditions at the water surface in the case of a undeveloped jet effect the spread of velocity profiles in the pool. Figure 2.4 is a profile view of a submerged, two-dimensional, free-jet.

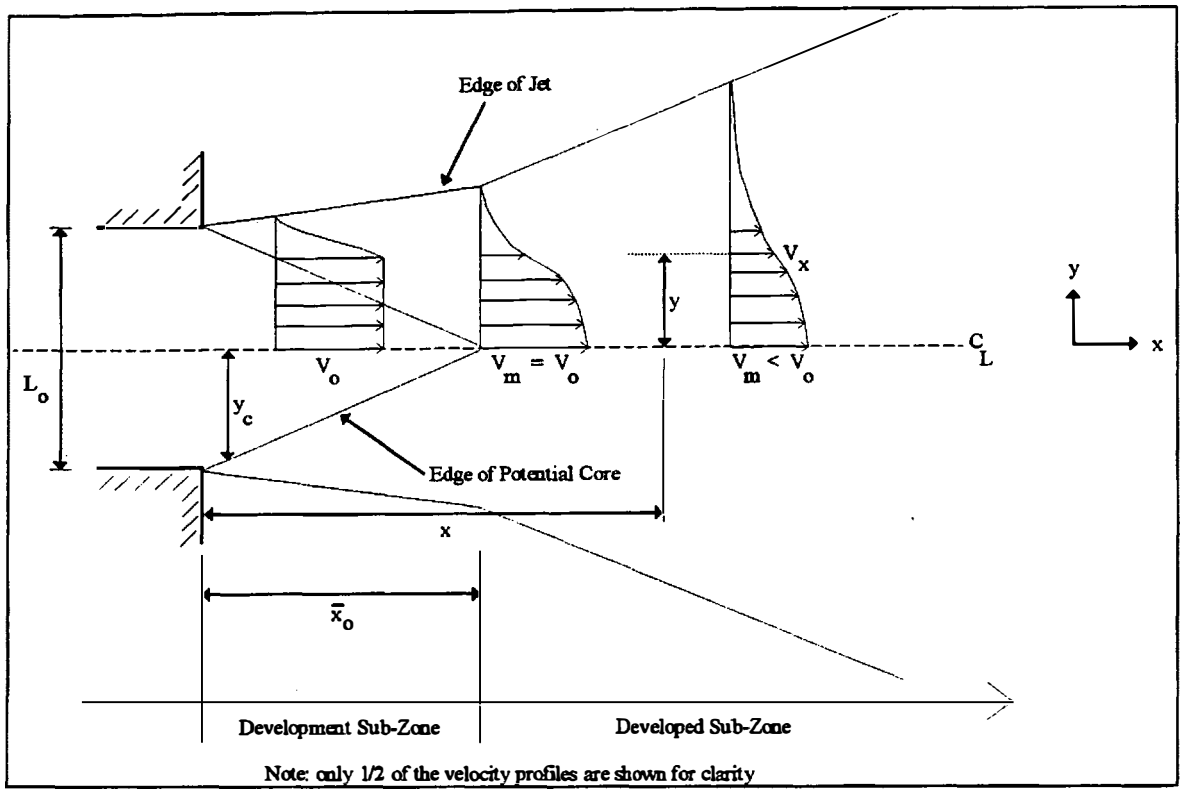

Figure 2.4 Submerged, two-dimensional, free jet

Descriptions of the velocity distribution of a submerged free-jet generally consist of two parts; the axial variation of the maximum velocity with increasing distance from the jet origin, and the transverse variation of velocity from the maximum at any given distance from the jet origin. Two sub-zones exist, the development sub-zone and the developed sub-zone.

Within the development sub-zone, the axial velocity remains constant and is equal to the original velocity of the jet. A triangular-shaped region, known as the potential core, is part of the development sub-zone. The potential core is characterized by the entrance

width of the jet and the axial length of the core. The velocity at all points inside of the potential core is equal to the original jet velocity. Outside of the potential core, within the development sub-zone, velocity decays with increasing distance perpendicular from the centerline axis.

Once the developed sub-zone is attained, the maximum velocity, that is equal to the original jet velocity, decays along the centerline of the jet as it continues along its original trajectory into the surrounding pool. Traveling perpendicularly from the centerline axis, velocity decays from the maximum velocity at that distance from the jet outlet. The transverse decay of velocity in both the development and developed sub-zones can be described by the same similarity curve.

2.3.2 Formulation of the Equations of Motion - Axial Variation of Velocity

Albertson (1950) provided one of the earliest descriptions of the axial variation of velocity away from the submerged entrance of the jet. His derivation of an axial velocity function included the following assumptions:

a. The background pressure distribution is hydrostatic. This assumption leads to the conclusion that tangential viscous shear is the sole force decelerating the jet in the mixing region. Mathematically, this can be expressed through the statement that the momentum flux is constant in the mixing region:

$$\frac{M}{M_o} = \frac{\int_0^\infty V_x^2 dA}{V_o^2 A_o} = 1 \qquad (2.28)$$

where

M = momentum flux (ML/T),

M_o = initial momentum flux (ML/T),

V_x = axial velocity of submerged, two-dimensional, free-jet (L/T),

V_o = initial axial velocity of the jet (L/T),

A = cross sectional area of the jet (L^2), and

A_o = the initial cross sectional area of the jet (L^2).

b. The diffusion process is dynamically similar under all conditions. Albertson justified this assumption with experimental data. Use of this assumption allowed the use of a single mean velocity distribution equation throughout the mixing region.

c. The jet diffuses into an infinite fluid. By making this assumption, he negated any possible boundary effects on the mean flow pattern that could have been caused by the geometry of the plunge pool.

With these assumptions, and empirical evidence, Albertson formulated the following equations describing the axial variation of the maximum velocity of a two-dimensional, submerged free-jet.

$$V_m = V_o \text{ for } x \le \bar{x}_o \tag{2.29}$$

$$\frac{V_m}{V_o} = 2.28\sqrt{\frac{L_o}{x}} \text{ for } x > \bar{x}_o \tag{2.30}$$

where

V_m = the maximum velocity at any distance from the outlet (L/T),

L_o = the width of the jet entrance outlet (L),

x = axial distance from the submerged jet outlet (L), and

$\bar{x}_o$ = the length of the potential core (L).

Albertson found that the length of the potential core was expressed as:

$$\bar{x}_o = 5.176 L_o \tag{2.31}$$

A more recent examination of the submerged free-jet was performed by Rajaratnam (1976). He found that the maximum velocity in the potential core was the same as presented in Equation 2.29. Rajaratnam also found that the length of the potential core was expressed as:

$$\bar{x}_o = 5.955 L_o \tag{2.32}$$

After studying the reports of several other researchers, Rajaratnam determined that in general, the equation describing the decay of the maximum axial velocity past the end of the potential core could be expressed as:

$$\frac{V_m}{V_o} = \frac{C_1}{\sqrt{\frac{x}{L_o} + C_*}} \tag{2.33}$$

where

C_1 = an experimental constant (nondimensional), and

C_* = another experimental constant (nondimensional).

Rajaratnam reported values of the two experimental constants found by other researchers. The values of C_1 and C_* are presented in Table 2.1.

Table 2.1 Experimental Coefficients

Researcher	C_1	C_*	Notes
Goertler (1942)	2.40	0	
Zijnen (1958)	2.49	0.6	(small nozzle)
Zijnen (1958	2.21	1.2	(large nozzle)
Abramovich (1963)	2.67	0	

Rajaratnam recommended the two experimental constants: $C_1 = 2.47$ and $C_* = 0$.

2.3.3 Formulation of the Equations of Motion - Transverse Variation of Velocity

Utilizing the Reynolds equations of motion in the Cartesian coordinate system and the continuity equation, it is possible to derive the equations of motion for the transverse velocity distribution of a submerged free-jet for points outside of the potential core. Rajaratnam (1976) presented this derivation in full detail. The following assumptions were made in his derivation:

a. The mean flow is two-dimensional and steady,

b. Velocity gradients transverse to the x direction are negligible,

c. Laminar shear stresses are negligible, and

d. The pressure gradient in the axial direction is negligibly small.

After considerable manipulation, Rajaratnam demonstrated that the equations of motion were:

$$\frac{1}{\rho}\left(\frac{\partial \tau}{\partial y}\right) = V_x\left(\frac{\partial V_x}{\partial x}\right) + V_y\left(\frac{\partial V_x}{\partial y}\right) \tag{2.34}$$

and

$$\frac{\partial V_x}{\partial x} + \frac{\partial V_y}{\partial y} = 0 \tag{2.35}$$

with

V_y = transverse velocity (L/T),

ρ = water density (M/L^3),

τ = turbulent shear stress (M/LT^2), and

y = transverse distance from the centerline of the submerged jet outlet (L).

Another equation is needed before a solution can be attempted, because the system is indeterminate with two equations and three unknowns; V_x, V_y, and τ.

Tollmien (1926) used Equations 2.34 and 2.35 along with the Prandtl mixing length relation to determine a non-linear, second-order ordinary differential equation that could be solved numerically to provide the transverse variation in the velocity gradient at any given axial distance from the entrance. The Prandtl mixing length theorem is expressed as:

$$\tau = \rho l^2 \left(\frac{\partial V_x}{\partial y}\right)^2 \tag{2.36}$$

where

l = Prandtl's mixing length (L).

Tollmien assumed that the mixing length, l, was proportional to the length scale b, which is the value of y where $V_x = \frac{1}{2}V_m$. Tollmien was able to integrate his differential equation numerically and present his results in a graphical format as displayed in Figure 2.5.

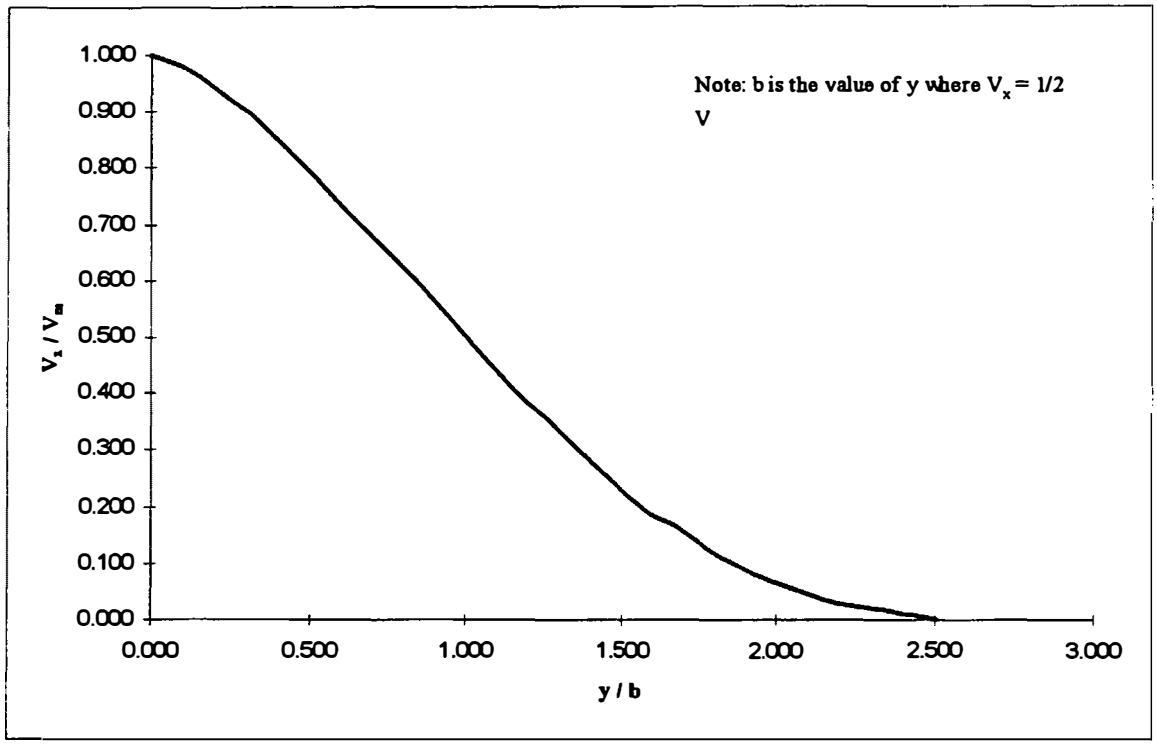

Figure 2.5 Tollmien's solution to Equations 2.34 - 2.36

Goertler (1942) used Equations 2.34 and 2.35 along with the second Prandtl equation to arrive at a solution for the transverse variation in the velocity gradient at increasing axial distance from the entrance. The second Prandtl equation is expressed as:

$$\tau = \rho\varepsilon\left(\frac{\partial V_x}{\partial y}\right) \qquad (2.37)$$

where

ε = coefficient of kinematic eddy viscosity (L/T).

Goertler assumed that the eddy viscosity was proportional to the product of the local maximum velocity and the length scale, thus $\varepsilon \propto V_m b$. Goertler was able to formulate and integrate a non-linear, first-order differential equation for an analytical result that plots similarly to Tollmien's solution. Figure 2.6 is a graphical representation of Goertler's solution.

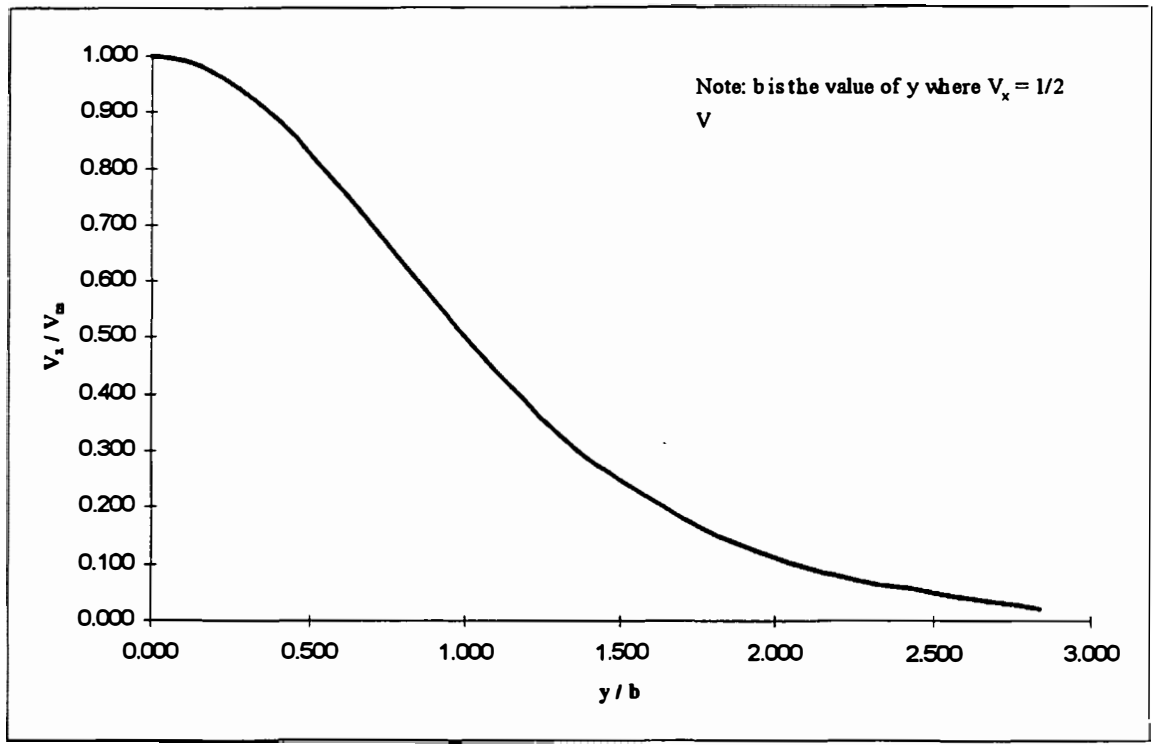

Figure 2.6 Goertler's solution to Equations 2.34, 2.35, and 2.37

Zijnen (1958) found that a Gaussian curve approximated the transverse variation of the velocity distribution. The Gaussian relationship is expressed mathematically as:

$$\frac{V_x}{V_m} = \exp\left(-0.693\left(\frac{y}{b}\right)^2\right) \tag{2.38}$$

with

b = scale length (L): the value of y at which $V_x = \frac{1}{2}V_m$.

Figure 2.7 presents a pictorial representation of Equation 2.38.

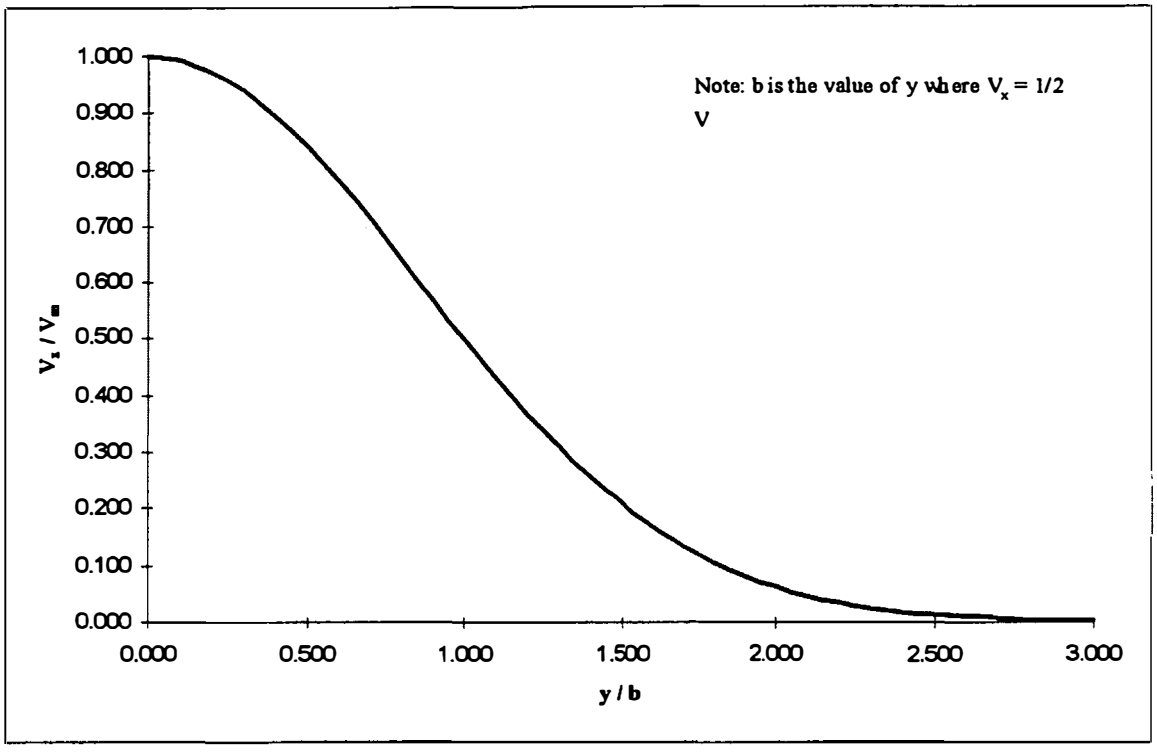

Figure 2.7 Gaussian velocity distribution

Comparing Figure 2.5 - 2.7, the solutions of Zijnen, Goertler, and Tollmien appear to verify each other.

2.4 Wall-Jet Zone

The wall-jet zone is the region of the turbulent, undeveloped jet trajectory that extends along the bottom of the plunge pool from the point where the background pressure returns to hydrostatic from the elevated state that was induced by excess stagnation pressure from the vertical impingement of the jet to infinity. The mean direction of the jet in the wall-jet zone is horizontal instead of vertical. In the wall-jet zone, viscous shear is important in controlling the rate of momentum transfer (energy dissipation), but an additional boundary-layer effect caused by the bottom of the plunge pool must also be recognized.

2.4.1 The Submerged Wall-Jet

The majority of existing research pertaining to the wall-jet zone concerns a set of boundary conditions that are simpler than those encountered in this study. The simplified case consists of a two-dimensional, turbulent jet with a submerged entrance, and an infinite pool above a bottom boundary that extends from the jet outlet to infinity. Figure 2.8 is a profile view of a submerged, two-dimensional, wall-jet.

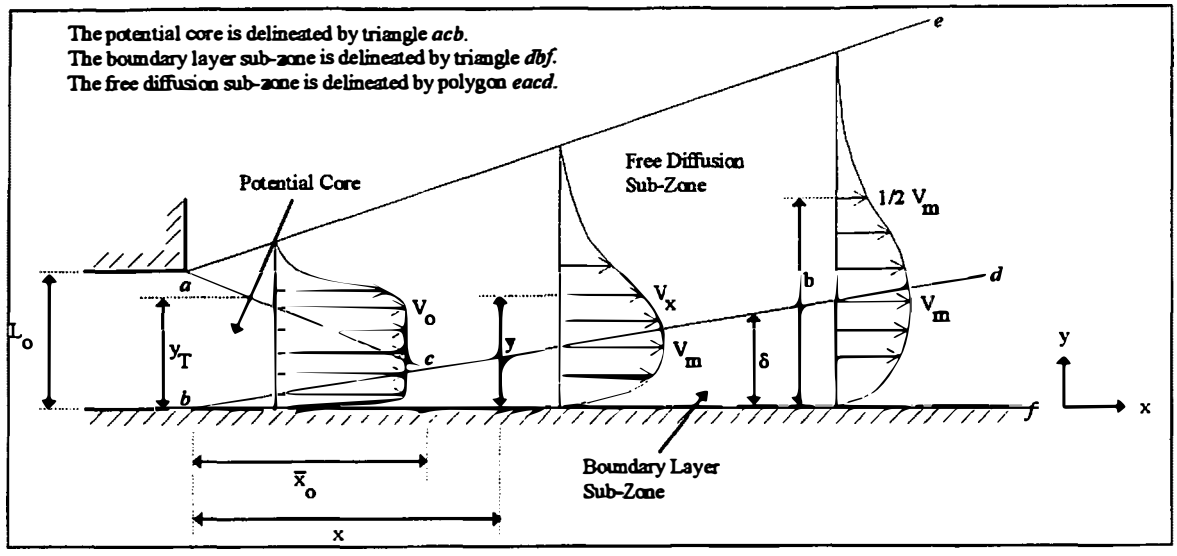

Figure 2.8 Submerged, two-dimensional, wall jet

Three distinct regions of interest occur in the case of the submerged, two-dimensional wall-jet; the potential core, the boundary layer sub-zone, and the free diffusion sub-zone. The potential core of the wall-jet zone is characterized by a uniform velocity distribution equal to the initial velocity of the jet at the entrance. It is bounded by two shear layers. The top layer is caused by viscous shear with the surrounding fluid and is similar to the shear layers found in the potential core of the submerged free-jet. The bottom layer is dominated by the boundary effect occurring near the wall. The boundary layer sub-zone is located between the lower shear layer of the potential core and the bottom of the plunge pool. Velocity behavior is dominated by wall roughness effects. The free diffusion sub-zone is located above the potential core and the boundary-layer sub-zone. Turbulent mixing similar to that observed with a submerged free-jet occurs in this area. The concept of momentum exchange is exploited to determine equations describing the velocity distribution.

2.4.2 Formulation of the Equations of Motion - Variation of Maximum Velocity

The variation of the maximum velocity in the submerged wall-jet is similar to that observed in the submerged free-jet; constant in the potential core and decreasing at distances beyond the end of the potential core. Unlike the submerged free-jet, where the maximum velocity occurs along the centerline of the jet, the maximum velocity in the submerged wall jet past the potential core occurs along the top of the boundary layer.

As in the potential core of the submerged free-jet, the maximum velocity, V_m, is equal the original velocity, V_o. Rajaratnam (1976) derived an equation for determining the length of the potential core by assuming that the velocity distribution in the boundary layer followed the Blasius law:

$$tan(5°)\bar{x}_o + 0.37\left(\frac{\nu}{V_o}\right)^{\frac{1}{5}} \bar{x}_o^{\frac{4}{5}} = L_o \qquad (2.39)$$

where

ν = kinematic viscosity of water (L^2/T).

The lower boundary of the potential core was delineated by making the same Blasius law assumption as in Equation 2.39:

$$\delta = 0.37\left(\frac{\nu}{V_o}\right)^{\frac{1}{5}} x^{\frac{4}{5}} \qquad (2.40)$$

where

δ = the height of the boundary layer (L).

The upper boundary of the potential core is a line connecting the upper edge of the jet outlet and the height of the boundary layer evaluated at the end of the potential core, $\bar{x}_o$.

Rajaratnam experimented with submerged wall-jets to determine how the variation of the maximum velocity past the end of the potential core. He determined that the equation best fitting the observed data was:

$$\frac{V_m}{V_o} = 3.50\sqrt{\frac{L_o}{x}} \tag{2.41}$$

2.4.3 Formulation of the Equations of Motion - Transverse Variation of Velocity

Myers (1961) found that a logarithmic law fit the transverse velocity variation data in the boundary layer sub-zone beneath the potential core better than a one-seventh power Blasius law. He developed the following expression:

$$\frac{V_x}{u_*} = 5.6\log_{10}\left(\frac{yu_*}{\nu}\right) + 4.9 \tag{2.42}$$

where

u_* = shear velocity, normally defined as $\sqrt{\frac{\tau_o}{\rho}}$, (L/T).

It is possible to derive the equations of motion for the transverse velocity distribution of a submerged wall-jet beyond of the potential core by integrating the Reynolds equations of motion in the Cartesian coordinate system and the continuity

equation. Rajaratnam (1976) presented this derivation based upon the following assumptions:

a. The mean flow is two-dimensional and steady,

b. Velocity gradients transverse to the x direction are negligible,

c. Laminar shear stresses are negligible, and

d. The pressure gradient in the axial direction is negligibly small.

Rajaratnam showed that the equations of motion were:

$$\frac{1}{\rho}\left(\frac{\partial \tau}{\partial y}\right) + \nu\frac{\partial^2 V_x}{\partial y^2} = V_x\left(\frac{\partial V_x}{\partial x}\right) + V_y\left(\frac{\partial V_x}{\partial y}\right) \tag{2.43}$$

and

$$\frac{\partial V_x}{\partial x} + \frac{\partial V_y}{\partial y} = 0 \tag{2.44}$$

Förthmann (1934) integrated Equations 2.43 and 2.44 numerically to obtain the transverse velocity variation in a dimensionless form. His solution is presented in Figure 2.9.

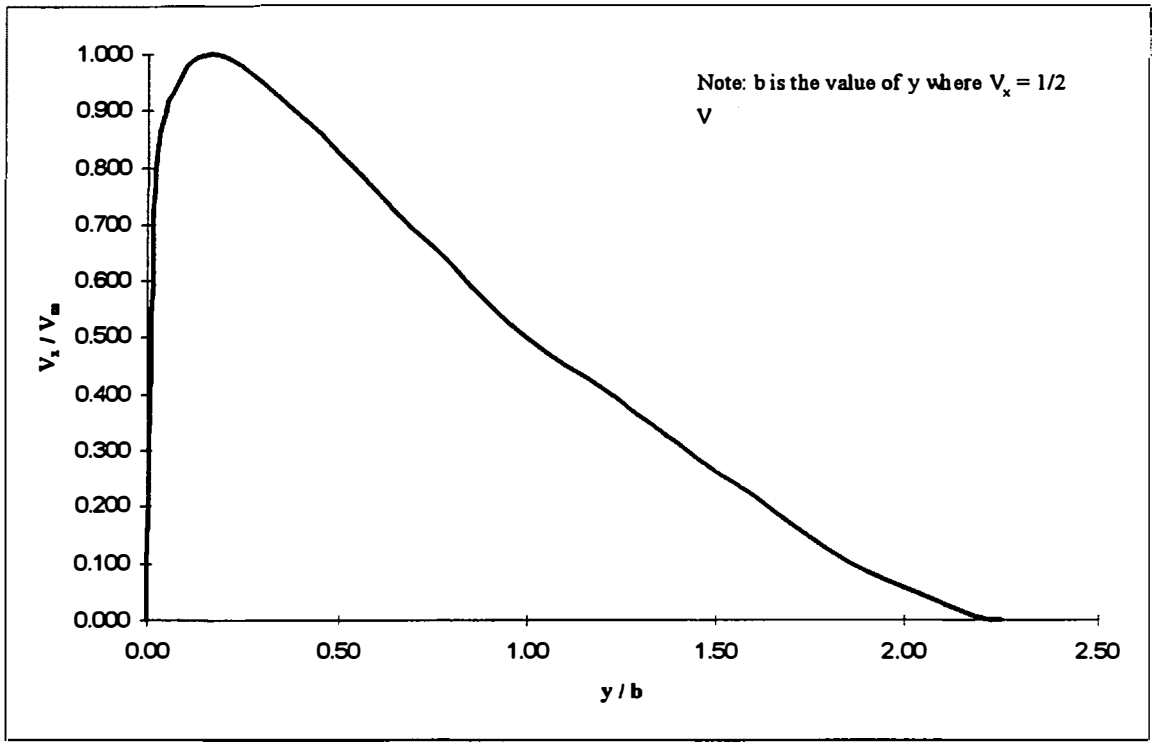

Figure 2.9 Förthmann's solution to Equations 2.43 and 2.44

Verhoff (1963) found a closed-form empirical solution to Equations 2.43 and 2.44 by using a statistical error function. His solution is expressed as:

$$\frac{V_x}{V_m} = 1.48\left(\frac{y}{b}\right)^{\frac{1}{7}}\left[1 - \text{erf}\left(0.68\frac{y}{b}\right)\right] \tag{2.45}$$

where

erf = the error function, defined as: $\text{erf}(x) = \frac{2}{\sqrt{\pi}}\int_0^x \exp\left(-t^2\right)dt$.

For computational ease, a common approximation of the error function can be developed by performing a Taylor-series expansion.

$$\text{erf}(x) \cong \frac{2}{\sqrt{\pi}}\left(x - \frac{x^3}{3} + \frac{1}{2!}\cdot\frac{x^5}{5} - \frac{1}{3!}\cdot\frac{x^7}{7} + \cdots\right) \tag{2.46}$$

Verhoff's solution, Equation 2.45, is plotted in Figure 2.10.

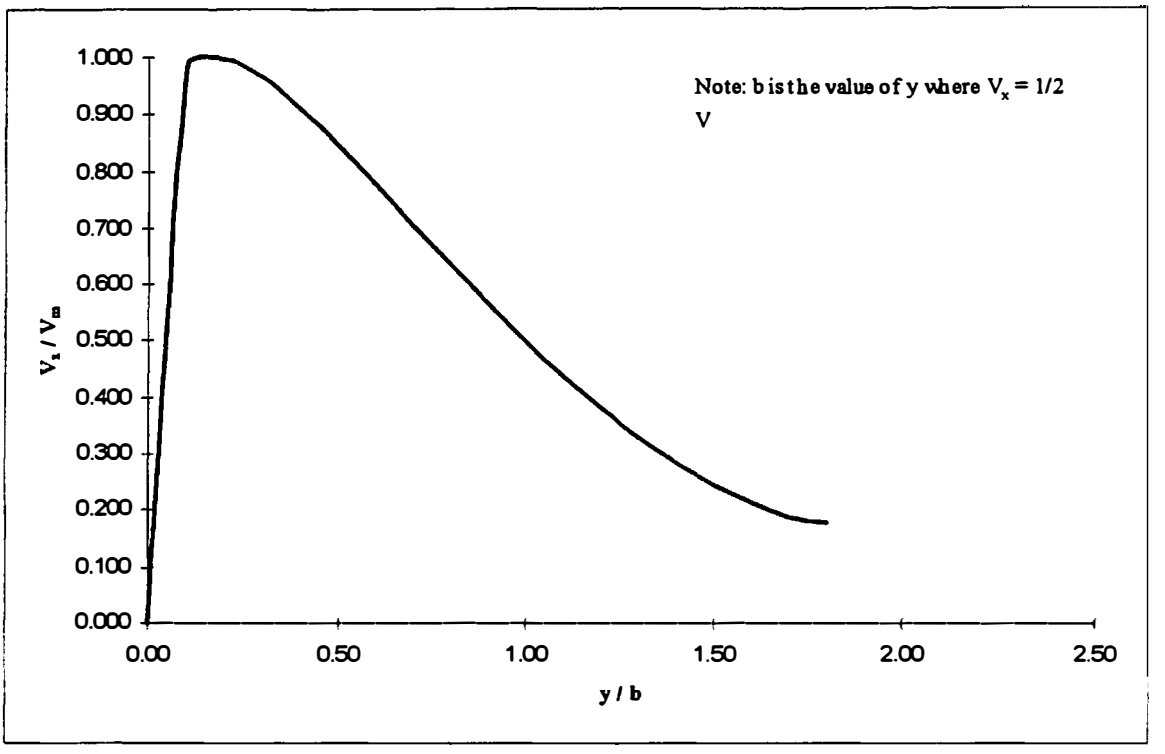

Figure 2.10 Verhoff's solution - Equation 2.45

2.5 Impingement Zone

The impingement zone is the portion of the turbulent, undeveloped jet trajectory near the point at which the jet's vertical motion stagnates and is translated to horizontal motion along the plunge pool floor. The background pressure in the impingement zone is elevated above hydrostatic due to the excess stagnation pressure from the impingement of the jet.

In the impingement zone, viscous shear and a boundary-layer effect are important factors controlling the rate of momentum transfer to the pool, but the most profound influence is caused by the additional stagnation pressure. The additional pressure build-up violates the negligible pressure variation assumption used in the formulation of equations with which to describe the velocity distribution of the jet in both the submerged free- and wall-jets.

When the impingement zone is considered, the free-jet and wall-jet zones can no longer be treated as separate processes. Instead, the impingement zone serves as a transition region, where the vertical motion of the jet is translated to horizontal motion along the pool floor. A consideration of the velocity distribution within the impingement zone requires a description of the variation of the velocity distribution within the impingement zone, and an explanation of the modifications necessary to the theoretical descriptions of velocity within the preceding and ensuing flow zones.

To delineate the vertical and horizontal motion of the jet in the impingement zone, an additional coordinate system is required. Variables given the subscript "1" will refer to horizontal motion along the pool floor. Figure 2.11 presents the two coordinate systems.

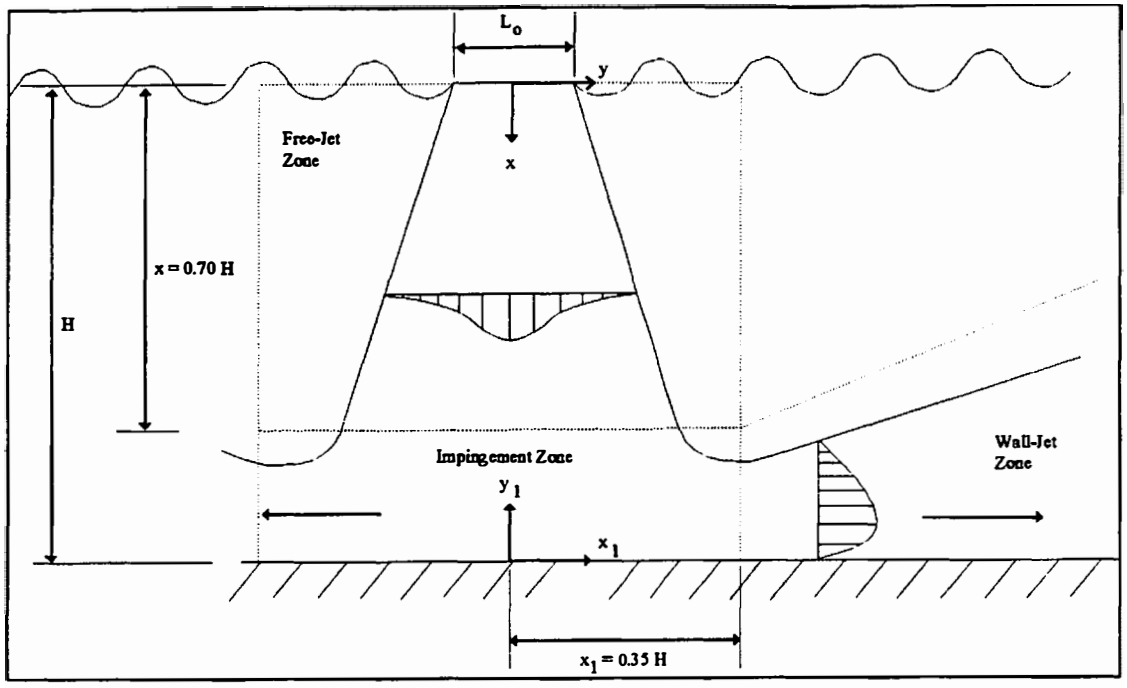

Figure 2.11 Coordinate systems in the plunge pool

2.5.1 Modifications to Velocity Equations within the Free-Jet Zone

The effect of the impingement zone upon the free-jet zone was examined by Belatos (1973). He noted that the region where the free-jet zone ends can be defined either in terms of pressure or velocity. In terms of pressure, the end of the free-jet zone occurs when the pressure change with increasing depth deviates from that predicted by a hydrostatic medium. In terms of velocity, the end of the free-jet zone occurs when the maximum vertical velocity of the jet, V_m, decreases to zero faster than predicted by Equation 2.33. Belatos, who was Rajaratnam's student, decided that the velocity criterion better described the boundary between the free-jet and impingement zones because the observed scatter in his velocity data was less than that of the pressure data. After close

analysis of his results, Belatos decided that the boundary between the free-jet and impingement zones was the point described by:

$$\frac{x}{H} = 0.70 \tag{2.47}$$

where

x = vertical distance measured from the plunge pool surface (L), and

H = the total depth of the plunge pool (L).

Starting with the variation of the maximum axial velocity in the free-jet zone, Belatos employed a dimensional analysis along with the integration of the conservation of momentum equation and test data to formulate an equation describing the variation of the maximum velocity in the free-jet zone. His equation was similar to that predicted by Rajaratnam, Equation 2.33, but with a different coefficient.

$$\frac{V_m}{V_o} = 2.50\sqrt{\frac{L_o}{x}} \tag{2.48}$$

where

V_m = the maximum vertical downward velocity of the jet at any depth (L/T),

V_o = the downward velocity of the jet at the plunge pool surface (L/T), and

L_o = the width of the "solid" jet core at the plunge pool surface (L).

Considering the transverse variation of velocity within the free-jet zone, Belatos determined that the Gaussian relationship, Equation 2.38, was functional. However, he adjusted the diffusion constant and formulated an explicit means for calculating the scale length, b.

$$\frac{V_x}{V_m} = \exp\left(-\left(\frac{0.834y}{b}\right)^2\right) \tag{2.49}$$

as:

$$b = 0.10x + 0.015H \tag{2.50}$$

with

V_x = vertical downward velocity away from the jet centerline (L/T),

y = horizontal distance from the centerline of the jet (L), and

b = scale length (L): the value of y at which $V_x = \frac{1}{2}V_m$.

2.5.2 Axial Variation of Velocity within the Impingement Zone

When Belatos examined the variation of the maximum velocity of the jet as it approached the pool floor in the vertical direction, he was able to find an empirical equation to fit his observed data. The equation form was similar to that presented by Rajaratnam in Equation 2.33, but included different coefficients and a term to measure the dimensionless distance from the pool floor.

$$\frac{V_m}{V_o} = 5.50\sqrt{\left(\frac{L_o}{H}\right)\left(1-\frac{x}{H}\right)} \tag{2.51}$$

Due to the increase in background pressure, the transverse velocity profiles did not follow a Gaussian curve. Belatos was unable to determine a method for predicting these profiles.

Belatos then focused on the transition between the impingement zone and the wall-jet zone. His arguments did not include a method to predict the transverse variation of the

local velocity component, V_{x1}. Belatos derived an equation for describing the variation of the maximum horizontal velocity of the jet in the impingement zone after accounting for the variation of excess pressure, (which could be fit by a Gaussian curve), by performing a similarity analysis and implementing the integral momentum equation:

$$\frac{V_{m1}}{V_o} = 2.77\sqrt{\left(\frac{L_o}{H}\right)\left(1-\exp\left(-38.5\left(\frac{x_1}{H}\right)^2\right)\right)} \tag{2.52}$$

where

V_{m1} = the maximum horizontal velocity of the jet (L/T), and

x_1 = horizontal distance measured from the centerline of the original jet (L).

Belatos was able to establish a boundary between the impingement and wall-jet zones. He set the boundary as:

$$\frac{x_1}{H} = 0.35 \tag{2.53}$$

2.5.3 Modifications to Velocity Equations within the Wall-Jet Zone

Belatos did not investigate the transverse velocity variations in great detail past the impingement zone, but his measurements did confirm that the transverse variation of the velocity with respect to the maximum velocity component at that position (x_1, y_1) followed the theoretical description of a wall-jet. Measurements conducted by Cola (1965) also agree with this result.

Belatos was able to derive an expression for the variation of the maximum velocity component in the wall-jet zone by performing a similarity analysis using the local skin friction coefficient and a group of empirically-derived constants:

$$\frac{V_{m1}}{V_o} = C\left(\frac{x_1}{L_o} - C_o\right)^a \tag{2.54}$$

$$a = -\frac{1}{2}\left(1+1.786C_f\right) \tag{2.55}$$

$$C_f = \frac{2\tau_o}{\rho(V_{m1})^2} \tag{2.56}$$

where

C = an empirical coefficient (nondimensional),

C_o = an empirical coefficient (nondimensional),

C_f = the skin-friction coefficient (nondimensional), and

τ_o = wall shear stress (M/LT^2).

The constants in Equation 2.54 require empirical calibration. Belatos' research indicated that in general; a ranged from -0.60 to 0.52, C_o ranged from 0 to 30, and C ranged from 2.0 to 2.7.

CHAPTER 3

DEVELOPMENT OF EQUATIONS

Upon completion of the literature review, a series of equations was formulated to predict the velocity distribution of a turbulent, developed jet as it travels through the air and impacts the plunge pool formed by an overtopping dam. These equations are based upon theoretical predictions for a two-dimensional, planar, undeveloped jet. The equations are divided into two groups corresponding to the different prediction techniques discussed in Chapter 2.

3.1 Coordinate System

A universal coordinate system was established to track the motion of the jet in the atmosphere. Figures 3.1 and 3.2 present profile and frontal views, respectively, of the entire jet trajectory with the coordinate system delineated.

The universal coordinate system (x, y, z) is used in the free-fall zone. The origin of the coordinate system is located at the centerline of the jet outlet with x extending horizontally downstream, y extending down, and z following the right-hand rule.

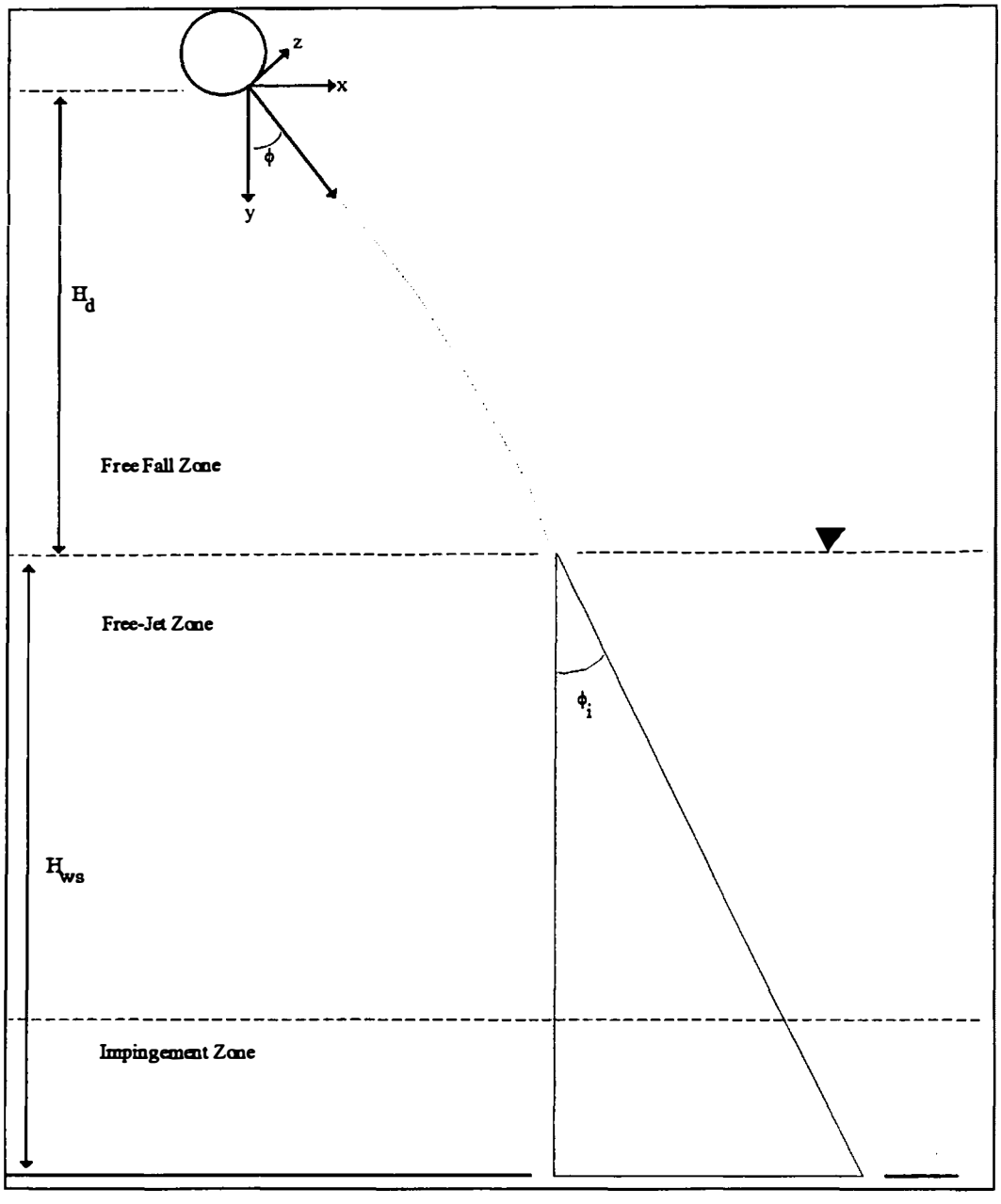

Figure 3.1 Profile view of jet trajectory -w- coordinate system shown

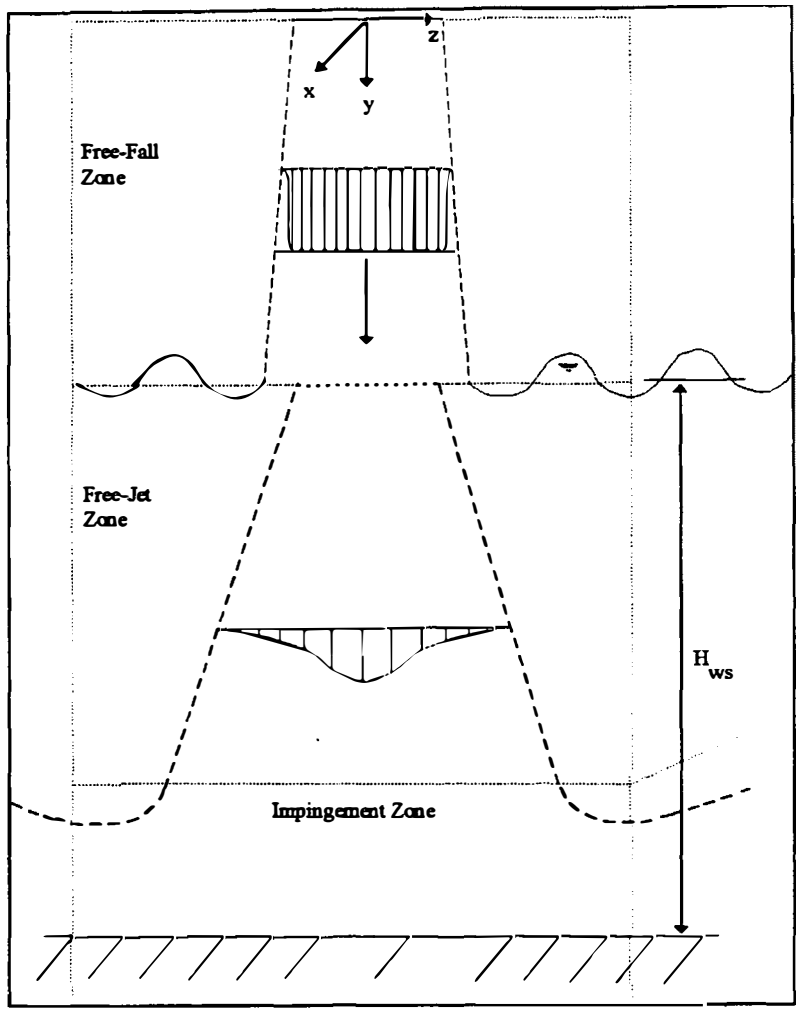

Figure 3.2 Frontal view of jet trajectory -w- coordinate system shown

Four separate variables are used to delineate specific geometric measurements pertaining to the model jet. Figure 3.1 illustrates the variables as:

H_d = the vertical distance from the outlet to the surface of the pool (L),

H_{ws} = the vertical distance from the pool surface to the floor of the pool (L),

ϕ_t = the impact angle the jet makes with the pool surface (°), and

ϕ = the issuance angle of the jet, measured from the vertical (°).

3.2 Differential Equation Technique

The prediction technique discussed in Section 2.2.5, hereafter referenced as the differential equation technique, utilizes a numerical integration of the componentized ballistic motion equation over small time increments. The following assumptions are made:

1. The developed jet is comprised entirely of discreet water particles that do not interact with each other.
2. The velocity of the entire jet can be approximated by the velocity of any of the discreet water particles comprising the jet.
3. The diameter of any water particle, which is defined as the volume of a sphere having the same volume as the particle, does not change over the free-fall trajectory of the jet.
4. The diameter of the representative water particle can be approximated by the maximum stable droplet size as predicted by irrigation sprinkler theory.
5. The drag coefficient of a water particle not moving at terminal velocity is the same as a smaller water particle moving at terminal velocity, provided the Reynolds numbers of the two water particles are equal.
6. The acceleration of the jet over a small time increment (0.001 seconds) is constant.

The differential equation technique is comprised of the following equations:

$$V = \sqrt{V_x^2 + V_y^2} \tag{3.1}$$

$$P = \frac{\sigma_w^3 \rho_a^2}{\mu_a^4 (\rho_w - \rho_a) g} \tag{3.2}$$

$$B_o = \frac{d^2 (\rho_w - \rho_a) g}{\sigma_w} \tag{3.3}$$

$$X = \ln\left(\frac{3}{4} B_o P^{1/6}\right) \tag{3.4}$$

$$Y = b_0 + b_1 X + b_2 X^2 + b_3 X^3 + b_4 X^4 + b_5 X^5 \tag{3.5}$$

$$Re_T = P^{1/6} \exp(Y) \tag{3.6}$$

$$V_T = \frac{\mu_a Re_T}{d\rho_a} \tag{3.7}$$

$$n = b_6 + b_7\left(\frac{V}{V_T}\right) \tag{3.8}$$

$$C_n = \frac{g}{V_T^n} \tag{3.9}$$

$$\frac{dV_x}{dt} = -C_n V^{n-1} V_x \tag{3.10}$$

$$\frac{dV_y}{dt} = g - C_n V^{n-1} V_y \tag{3.11}$$

$$V_{x,t+1} = V_{x,t} + \frac{dV_{x,t}}{dt}(\Delta t) \tag{3.12}$$

$$V_{y,t+1} = V_{y,t} + \frac{dV_{y,t}}{dt}(\Delta t) \tag{3.13}$$

$$x_{t+1} = x_t + V_{x,t}(\Delta t) + \frac{1}{2}\frac{dV_{x,t}}{dt}(\Delta t)^2 \tag{3.14}$$

$$y_{t+1} = y_t + V_{y,t}(\Delta t) + \frac{1}{2}\frac{dV_{y,t}}{dt}(\Delta t)^2 \tag{3.15}$$

where

V = the instantaneous velocity of the jet (L/T),

V_x = the horizontal velocity component of the jet (L/T),

V_y = the vertical velocity component of the jet (L/T),

P = Physical property number (nondimensional),

σ_w = surface tension of water (M/T^2),

ρ_w = density of water (M/L^3),

ρ_a = density of air (M/L^3),

μ_a = dynamic viscosity of air (M/LT),

g = acceleration due to gravity (L/T^2),

B_o = Bond number (nondimensional),

d = diameter of a sphere having the same volume as a water drop (L),

b_0 = -5.0015, an experimentally derived constant (nondimensional),

b_1 = 5.23778, an experimentally derived constant (nondimensional),

b_2 = -2.04914, an experimentally derived constant (nondimensional),

b_3 = 0.475294, an experimentally derived constant (nondimensional),

b_4 = -0.0542819, an experimentally derived constant (nondimensional),

b_5 = 0.00238449, an experimentally derived constant (nondimensional),

b_6 = 2.024, an experimentally derived constant (nondimensional),

b_7 = 1.058, an experimentally derived constant (nondimensional),

Re_T = the Reynolds number at terminal velocity (nondimensional),

V_T = terminal velocity of deforming water droplets in air (L/T),

n = an experimentally determined exponent (nondimensional),

C_n = an empirical drag coefficient (L^{1-n}, T^{n-2}),

x_t = horizontal position coordinate at current time increment (L),

x_{t+1} = horizontal position coordinate at next time increment (L),

y_t = vertical position coordinate at current time increment (L), and

y_{t+1} = vertical position coordinate at next time increment (L).

A computer program was written to predict the impact velocity of a turbulent, developed jet at the point of impact with the plunge pool surface with the following iterative scheme:

a. Calculate resultant velocity from known velocity components with Equation 3.1,

b. Calculate terminal velocity using Equations 3.2 - 3.7,

c. Calculate the drag function exponent, n, using Equation 3.8,

d. Calculate the empirical drag coefficient, C_n, using Equation 3.9,

e. Calculate the horizontal and vertical acceleration components with Equations 3.10 and 3.11, and

f. Calculate new component velocities and coordinate positions using Equations 3.12 - 3.15.

When the vertical position coordinate of the falling water particle is level with the known plunge pool surface elevation, the computer program terminates. The instantaneous velocity of the jet at impact with the water surface, V_i, is the velocity of the water particle at this point. Additional information pertaining to the computer program is presented in Appendix A.

3.3 Dimensional Equation Technique

An alternate prediction technique was developed in Section 2.2.4 by incorporating an aerodynamic drag deceleration term into Ervine and Falvey's (1987) estimate of the velocity of the solid core of a turbulent, undeveloped jet when it impacts the surface of the plunge pool, Equation 2.4. This technique is hereafter referenced as the dimensional equation technique. The following assumptions are made:

1. The developed jet is comprised entirely of discreet water particles that do not interact with each other.
2. The velocity of the entire jet can be approximated by the velocity of any of the discreet water particles comprising the jet.
3. The shape of any water particle within the jet does not change over the free-fall trajectory of the jet.
4. The diameter of the representative water particle can be approximated by the maximum stable droplet size as predicted by irrigation sprinkler theory.
5. The drag coefficient of the representative water particle can be approximated by the drag coefficient of a sphere of water traveling at the initial velocity of the jet upon emittance.
6. The drag coefficient of the representative water particle is fixed over its fall through the atmosphere.
7. The effective distance the representative water drop travels can be approximated by the drop height, H_d.

The dimensional equation technique consists of a single equation:

$$V_i = \sqrt{V_o^2 + 2gH_d} - \sqrt{3C_d\left(\frac{\rho_a}{\rho_w}\right)\left(\frac{H_d}{d}\right)V_o^2} \qquad (3.16)$$

where

C_d = drag coefficient (nondimensional),

ρ_a = air density (M/L^3),

ρ_w = water density (M/L^3),

H_d = the vertical distance from the outlet to the surface of the pool (L),

d = diameter of a sphere having the same volume as a water drop (L),

g = acceleration due to gravity (L/T^2),

V_o = initial velocity of the jet (L/T), and

V_i = impact velocity of the jet at the plunge pool surface (L/T).

3.4 Comparison of Prediction Techniques

The two impact velocity prediction techniques that have been presented, the differential equation technique and the dimensional equation technique, offer viable methods by which the velocity of a turbulent, developed jet can be approximated at impact with the plunge pool. A side-by-side comparison of the two techniques may illustrate the possible advantages and limitations inherent in each. Table 3.1 presents the aforementioned comparison.

Table 3.1 - Comparison of Techniques

Comparison Category	Dimensional Equation Technique	Differential Equation Technique
Drag Force	Disadvantage: assumed to be constant over trajectory	Advantage: allowed to vary over trajectory
Droplet Shape	Disadvantage: assumed to remain constant (spherical)	Advantage: allowed to vary over trajectory
Applicability	Advantage: single equation, may be hand-calculated	Disadvantage: requires a computer for calculation
Information Required	Advantage: only requires: V_o, H_d, d, ρ_a, and ρ_w	Disadvantage: requires: V_o, H_d, d, ρ_a, ρ_w, ϕ, μ_a, μ_w, and σ_w
Distance over which drag force is applied	Disadvantage: assumes the fall length to be the vertical distance from the dam top to the plunge pool	Advantage: variable parabolic trajectory takes into account entire fall distance

One possible factor that may limit the accuracy of the differential equation technique is that it was originally developed for sprinklers having jets with small diameter water drops of less than 6 mm. A primary assumption of the differential equation technique is that the drag coefficient of a larger water particle not moving at terminal velocity is the same as that of a smaller water particle, provided that the Reynolds numbers of the two jets are identical. If this assumption is incorrect, it would be reasonable to expect larger drag coefficients, compelling a recalibration of the mathematical model utilized by the differential equation technique.

An element that may effect the accuracy of both techniques is the assumption that the droplet size is the maximum stable droplet size suggested by sprinkler theory, which is about 6 mm. It may be possible that the water droplets comprising the developed jet may not have yet reached a stable size and are in fact larger upon impact with the plunge pool surface.

After comparing the two prediction techniques, it is not readily apparent which method is more appropriate in the dam overtopping scenario. Both techniques appear to be equally valid. In order to determine the more appropriate prediction technique, it will be necessary to use experimental data to test the validity of each.

CHAPTER 4

TEST FACILITY & PROCEDURES

In order to validate the different impact velocity prediction techniques, an experimental facility was required that could model a turbulent, developed jet similar to those expected at overtopping steep faced dams. A description of the test facility, test procedures, and instrumentation will be presented in this chapter.

4.1 Location of Model

The dam overtopping model was constructed in the Hydraulics Laboratory, Engineering Research Center, Colorado State University. The Engineering Research Center is located immediately northwest of Fort Collins, Colorado and is situated at the base of Horsetooth Reservoir. Water is conveyed from Horsetooth Reservoir and stored in a one acre-foot capacity sump (43,560 ft^3 or 1,233.5 m^3) located beneath the main Hydraulics Laboratory floor. Recirculating pumps draw water from the sump for use in the dam overtopping model.

4.2 Model Construction and Calibration

The dimensions of the dam overtopping facility were scaled from a proposed prototype facility. The reduction followed a 1:3 Froude scaling criterion. Features of the facility include the water supply system, 8 inch delivery pipe, orifice and orifice assembly, wasteway, and viewing platform. The right wall (looking downstream) of the test basin is constructed of Plexiglas facilitating observation of the test basin and water jet. Plans of the facility are shown in Figures 4.1 - 4.4.

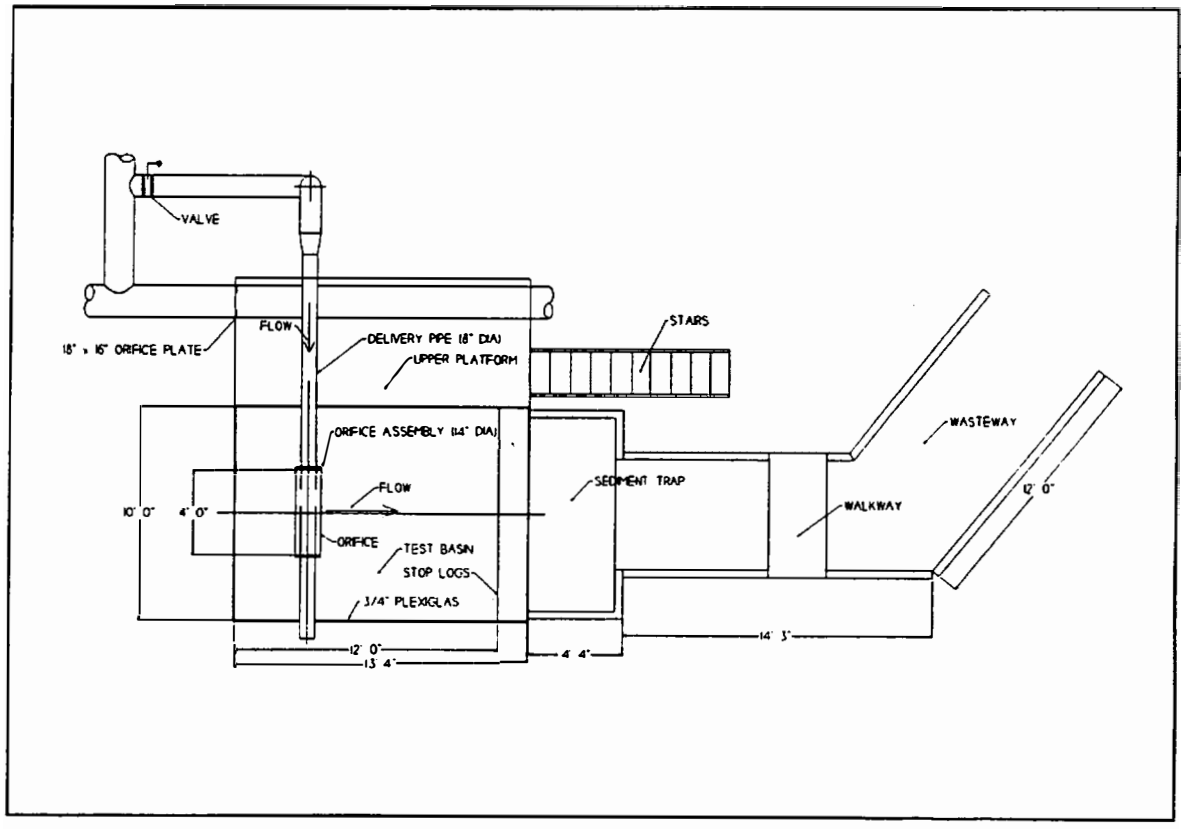

Figure 4.1 Plan view of facility with features indicated

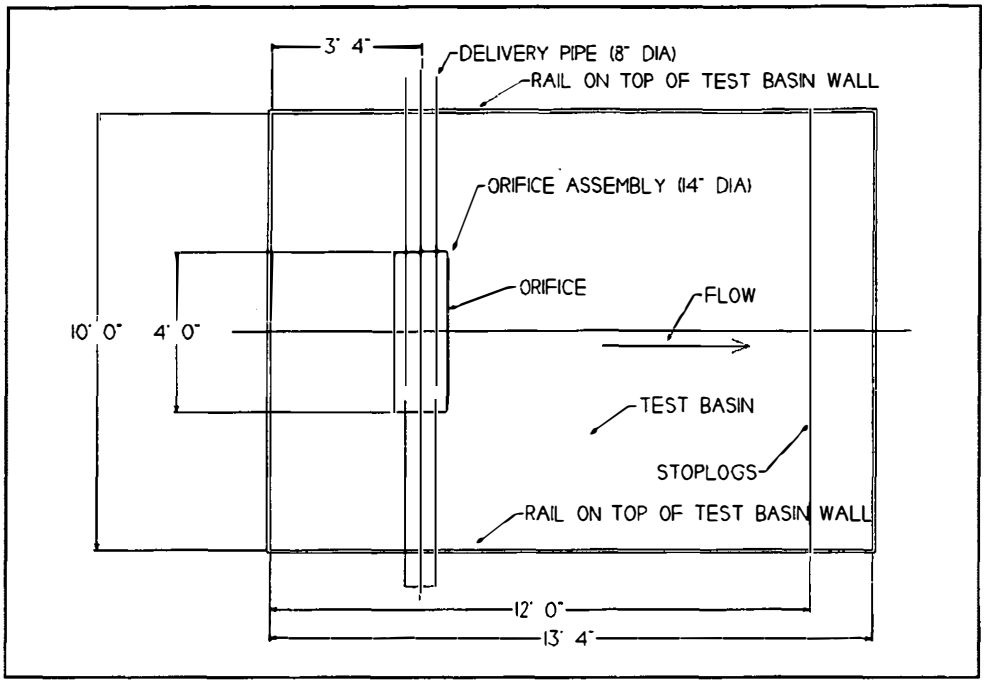

Figure 4.2 Plan view of test basin

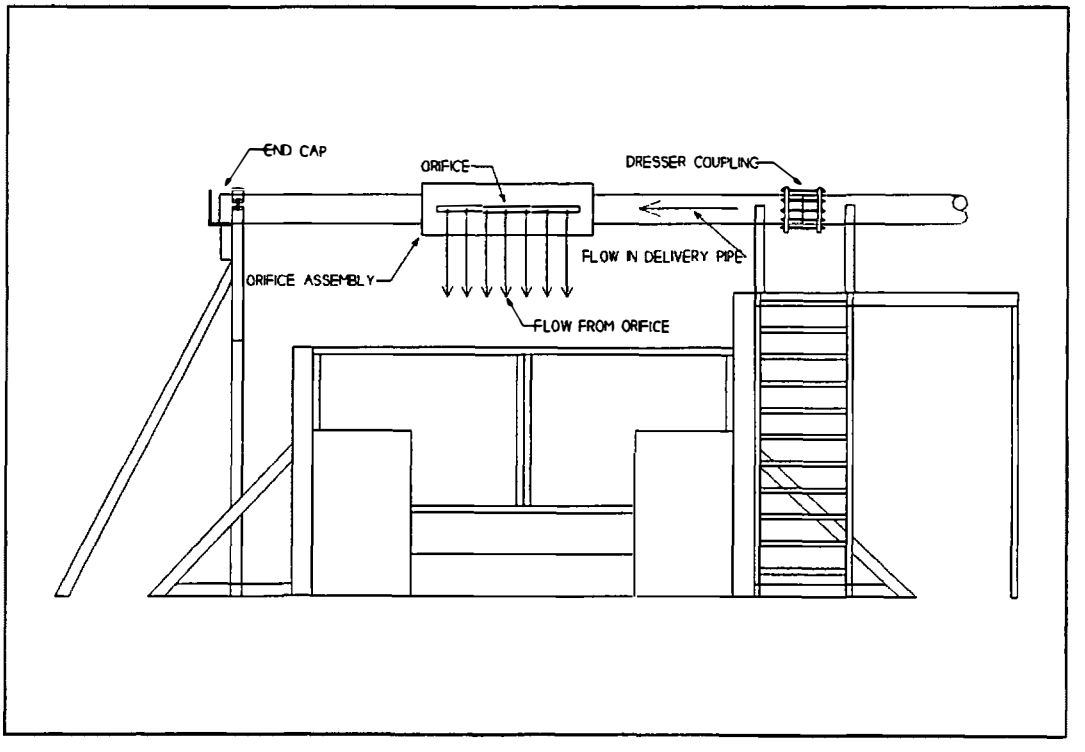

Figure 4.3 Elevation of test facility from wasteway (downstream) perspective

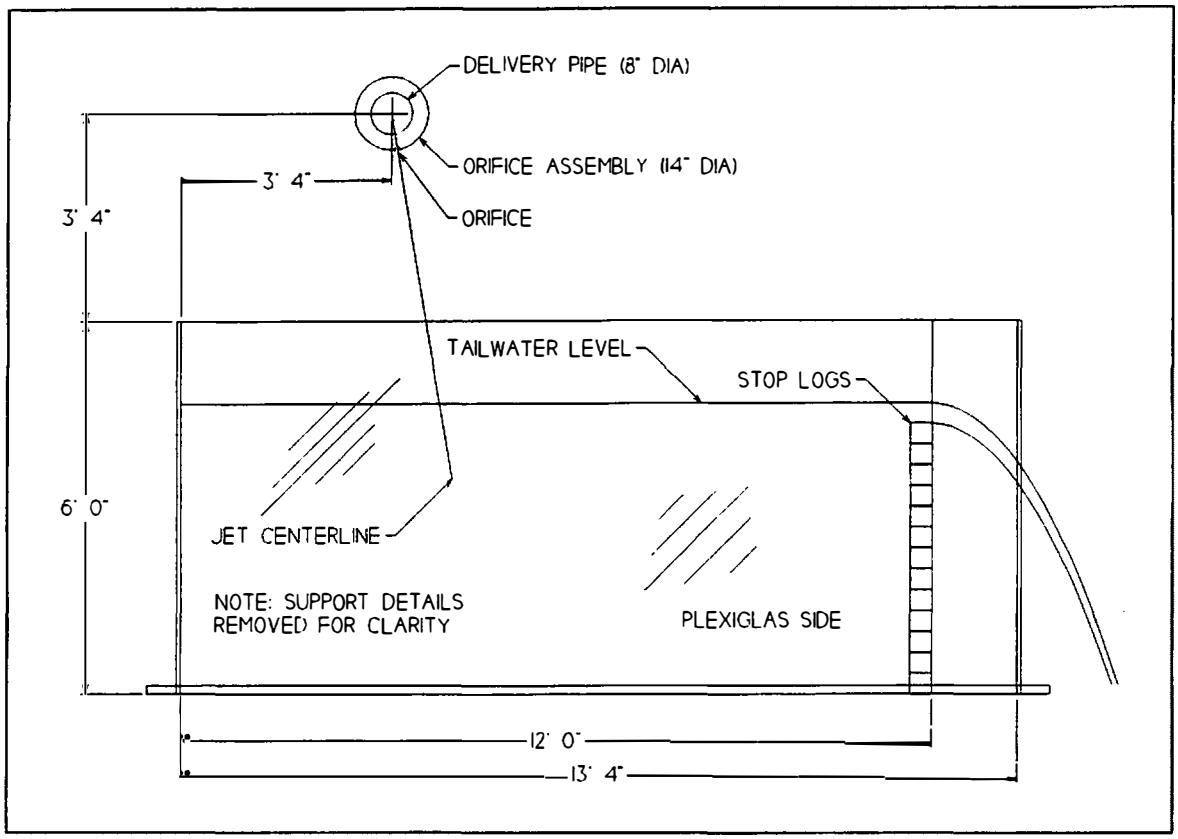

Figure 4.4 Side elevation of test facility with orifice

Rails were constructed on the top of the test basin walls perpendicular to the main delivery pipe. The rails were used to guide a "H" beam that was fitted with wheels at its ends. The "H" beam extended across the top of the test basin walls parallel to the main delivery pipe. The "H" beam could traverse the confines of the test basin and serve as a support system for a movable point-gage assembly. The point-gage assembly served as a mounting device for the instruments that were operated in the plunge pool. The "H" beam and the movable point-gage assembly allowed for the positioning of the mounted probes

throughout the test basin. Movable catwalks were constructed to allow access to the point-gage assembly.

4.3 Development of Orifice Assembly

In order to model a developed jet in the dam overtopping facility, an orifice assembly was designed to allow the initial angle of jet issuance to vary from 0° (straight down) to 90° (horizontal). The hydraulic dresser coupling shown in Figure 4.3 allows rotation of the delivery pipe. A stamped vernier scale was placed on the delivery pipe at the dresser coupling to monitor the jet issuance angle. The delivery pipe was capped at the end and a hole pattern was cut into the upstream side of the delivery pipe. The hole pattern was centered 180° from the centerline of the orifice assembly. Figure 4.5 illustrates the initial hole pattern cut into the delivery pipe.

A 14 inch diameter orifice assembly was fabricated and placed around the hole pattern. The orifice assembly guides flow from the holes around the delivery pipe and to a sharp-edged orifice. The length of the sharp-edged orifice was fixed at 40 inches, while the width was varied between 0.4 and 2.8 inches. Figure 4.6 shows the orifice assembly mounted on the delivery pipe.

Flow issues through the orifice assembly and falls into the tailwater basin. Figure 4.7 illustrates the dam overtopping model in operation.

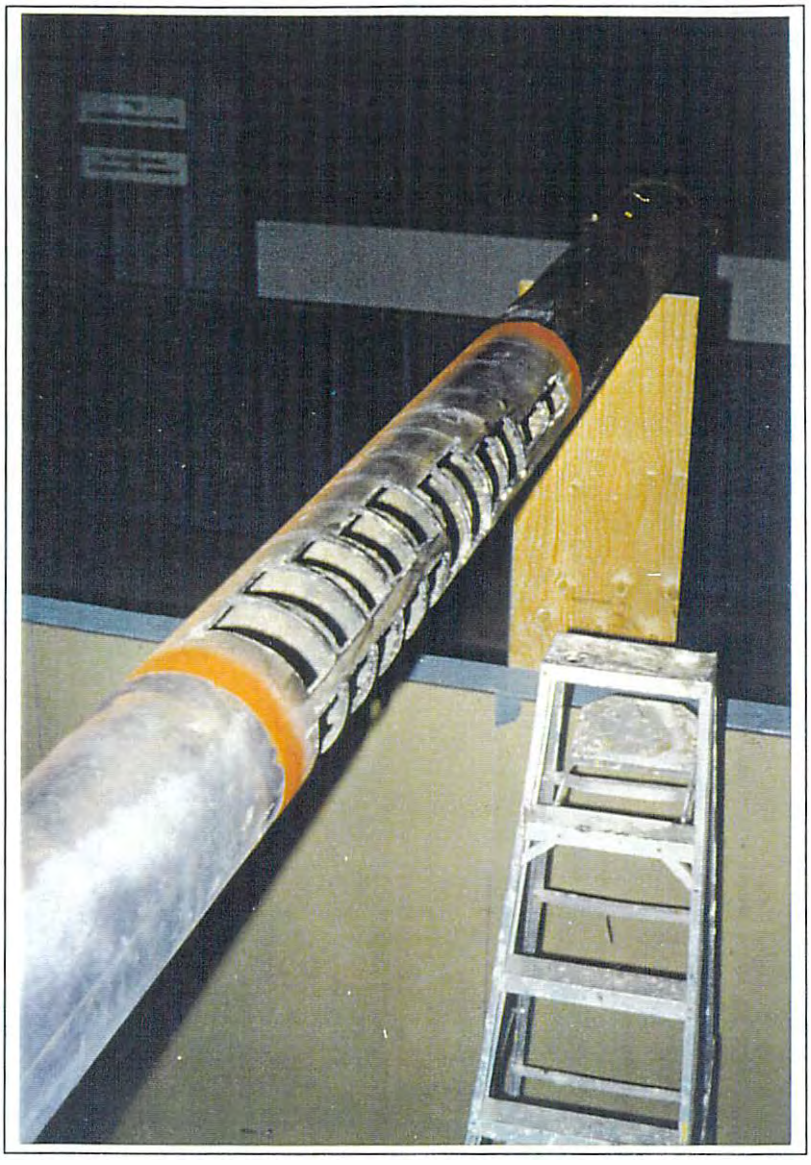

Figure 4.5 Hole pattern in delivery pipe

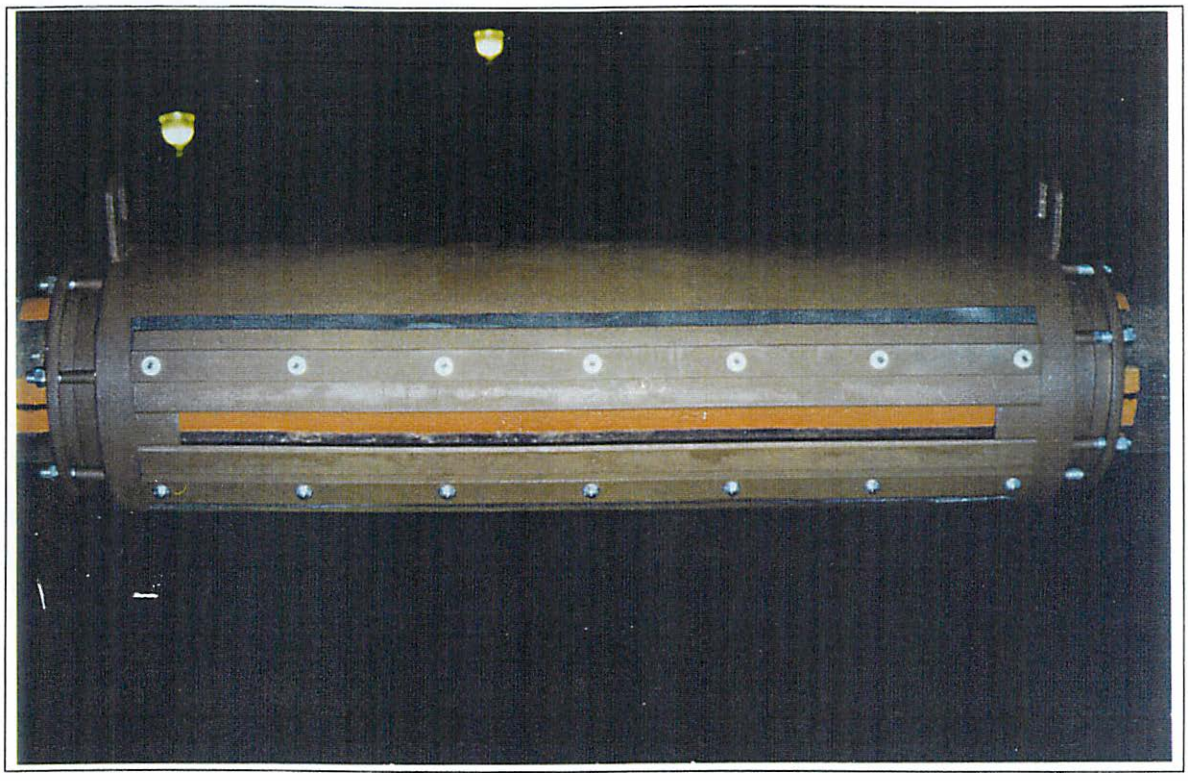

Figure 4.6 Orifice assembly

Figure 4.7 Dam overtopping model in operation

Due to the complex hydraulic interactions occurring within the orifice assembly, it was difficult to accurately calculate the size and placement of the holes in the delivery pipe to generate a uniform pressure distribution. (A uniform pressure distribution inside the orifice assembly will generate a uniform jet.) An initial hole pattern was designed using sprinkler manifold sizing theory. This pattern was then altered in an experimental testing series to develop a pattern which generated a uniform, non-skewing jet. Additional information pertaining to the orifice assembly design testing series is presented in

Appendix B. The final design specifications of the orifice assembly are illustrated in Figures 4.8 - 4.12.

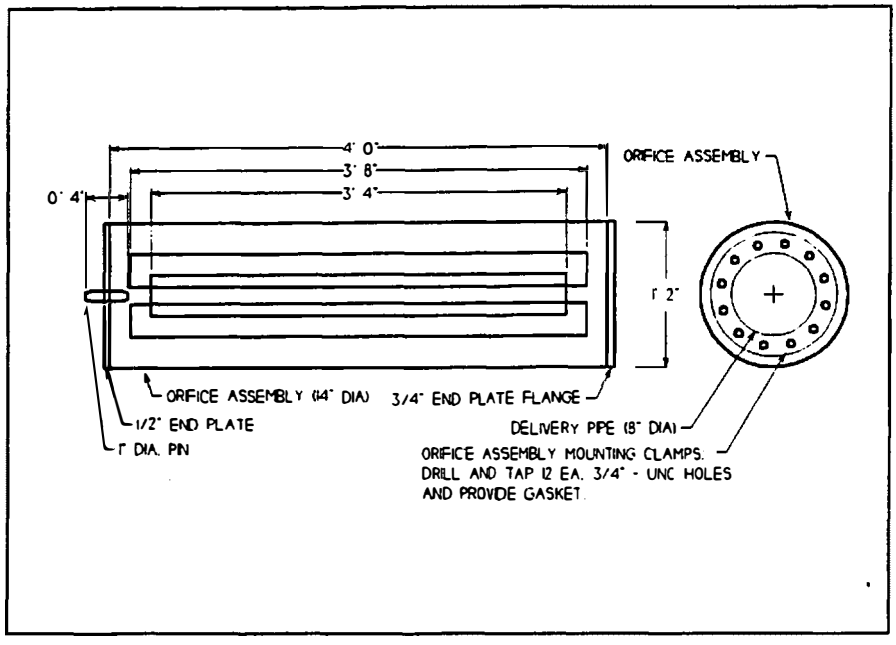

Figure 4.8 Orifice assembly

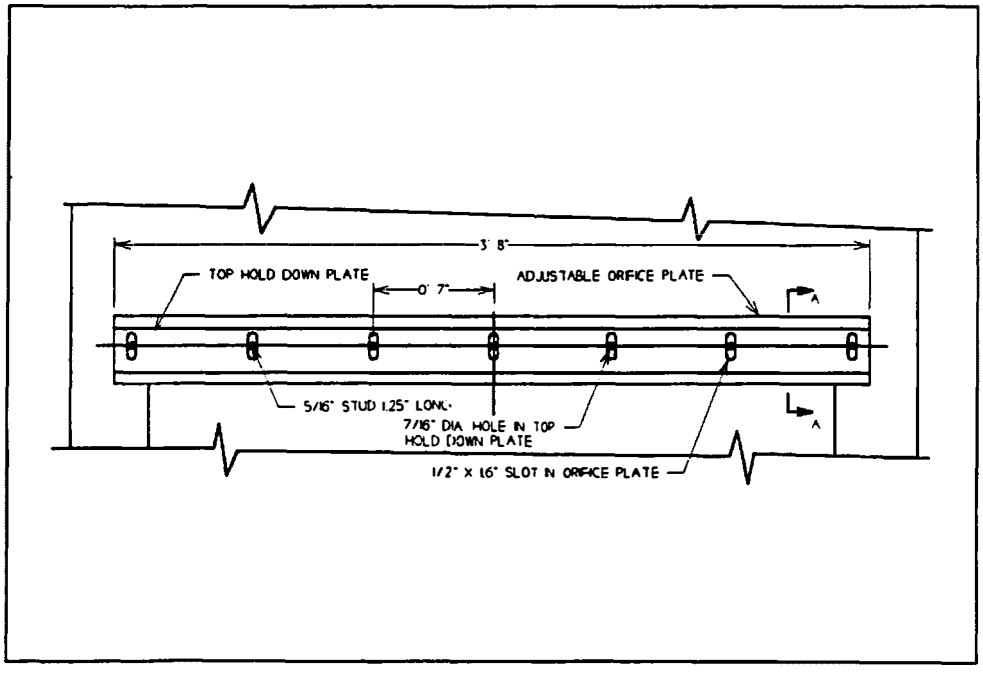

Figure 4.9 Orifice blade detail

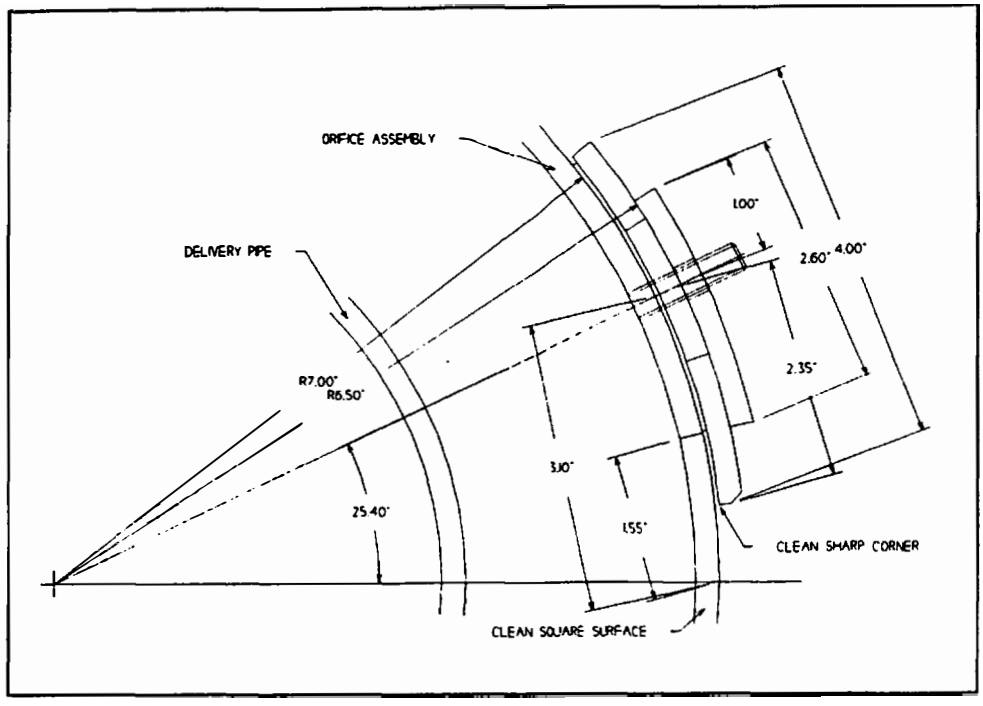

Figure 4.10 Mounting detail for orifice blade

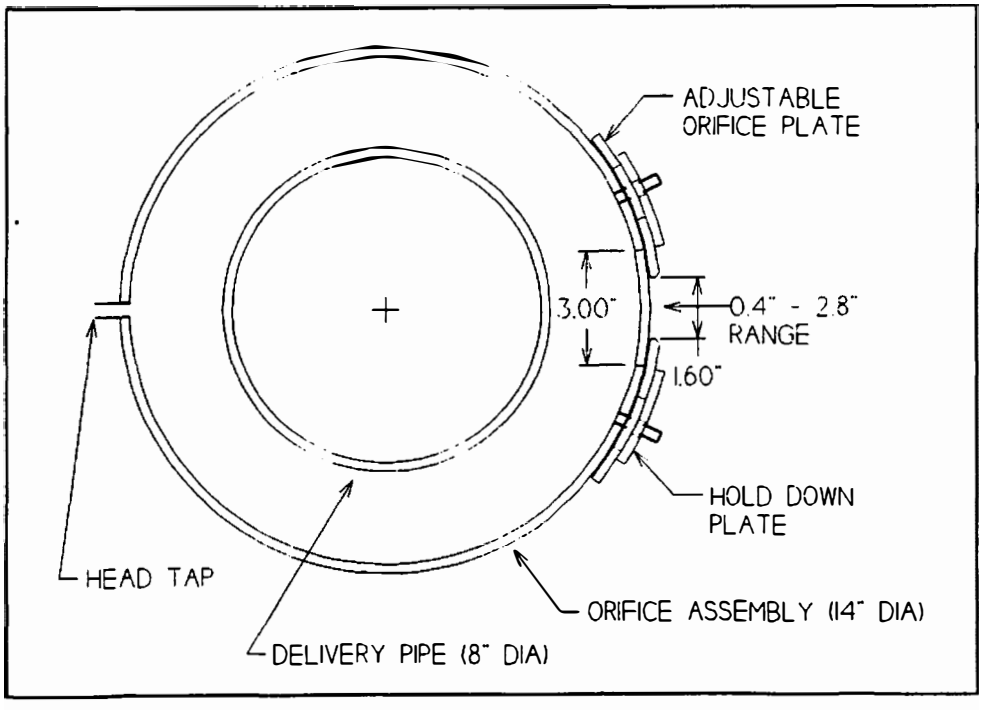

Figure 4.11 Cross section of orifice assembly

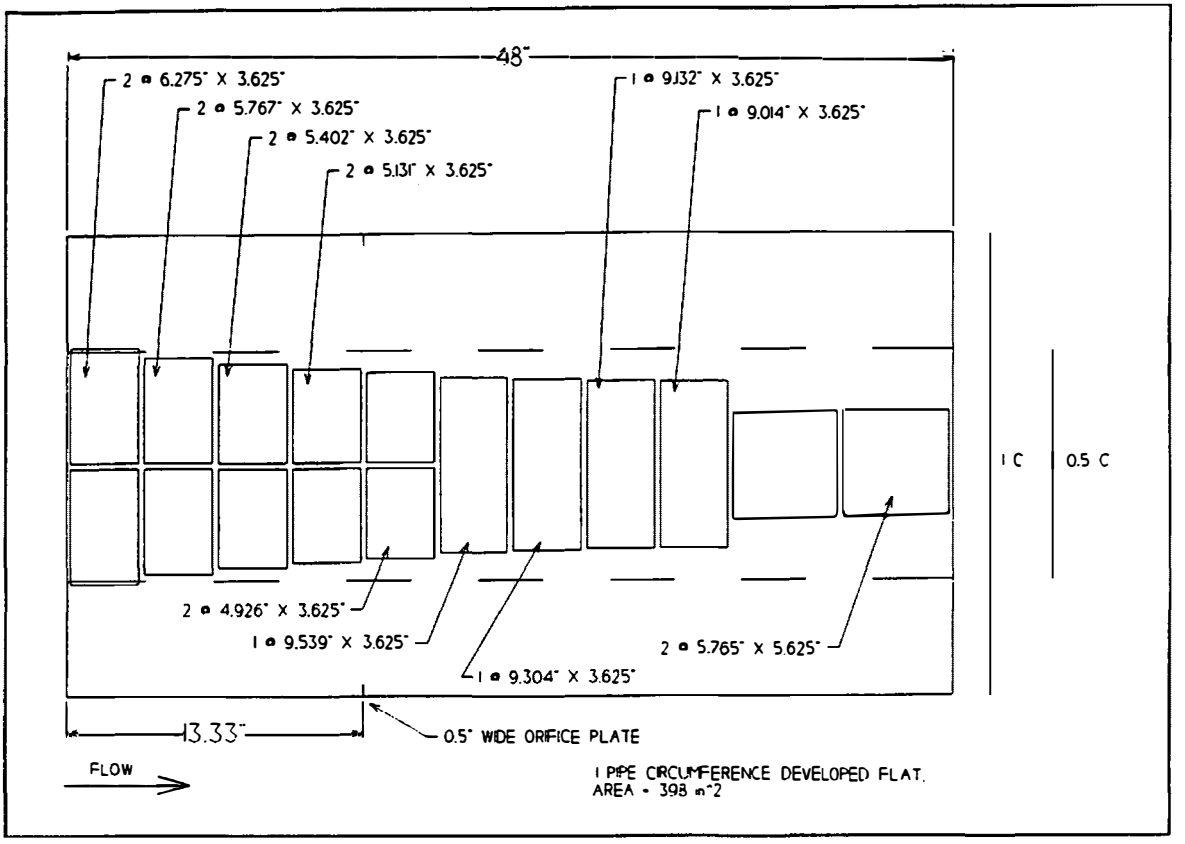

Figure 4.12 Final configuration of 8" delivery pipe hole pattern

4.4 Instrumentation

The instruments used in the dam overtopping model included a calibrated orifice plate with water manometer, a pitot tube, a back-flushing pitot-static tube, an air concentration probe, and an acoustic Doppler velocimeter. Each instrument will be described and its purpose discussed.

4.4.1 Orifice Plate

A calibrated orifice plate was placed in the water supply pipeline upstream from the control valve shown in Figure 4.1. Total volumetric discharge is measured with the orifice plate. The orifice plate serves to contract the walls of the pipe and establish a pressure differential across the front and back sides of the plate. The orifice plate was calibrated to establish an equation relating the pressure head differential across the plate and the volumetric discharge:

$$Q = 8.3552\sqrt{\Delta h} \tag{4.1}$$

where

Q = the volumetric flow rate (ft^3/s), and

Δh = the pressure head differential (ft).

The accuracy of the orifice plate for discharge measurement has been investigated by Stearns, Johnson, Jackson, and Larson (1951). With experimental data, they showed that orifice plates yield discharge measurements that are accurate to ±2%.

4.4.2 Pitot Tube

A pitot tube was utilized to accurately determine the initial velocity of the developed jet at the point of issuance from the orifice assembly. A graduated rod and clamp system was developed to allow the positioning of the tip of the pitot tube anywhere in front of the orifice. Figure 4.13 illustrates the pitot tube with the rod and clamp system.

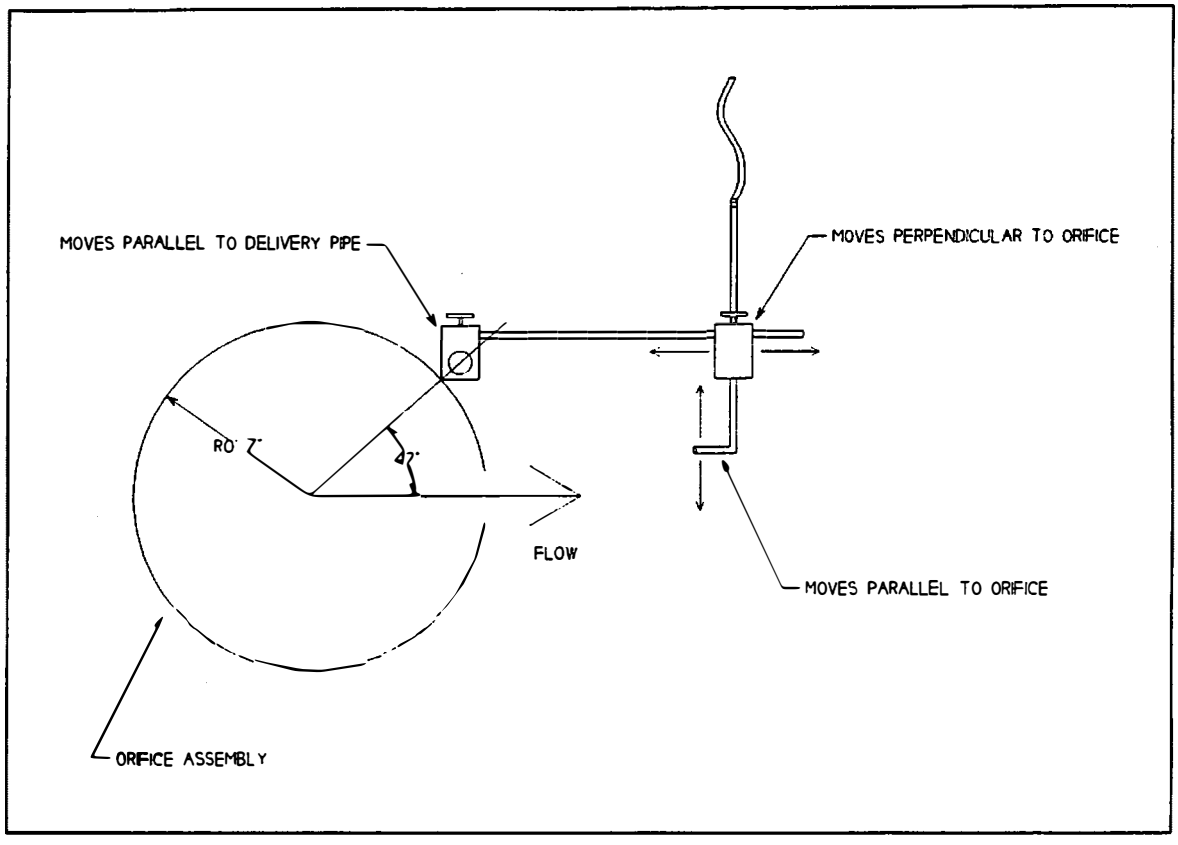

Figure 4.13 Pitot tube with rod and clamp system

The equation governing simple pitot tube measurement is expressed as:

$$V = \sqrt{2g\Delta h} \tag{4.2}$$

where

V = the velocity of the flow (L/T),

g = the acceleration due to gravity (L/T^2), and

Δh = the pressure head differential (L).

In order to measure the full pressure head differential with a simple pitot tube, the tip of the pitot tube must be placed at the vena-contracta, or point of minimum thickness, of the jet. The background pressure of the vena-contracta of an issuing jet into the atmosphere is atmospheric. Therefore the measured pressure head differential is attributed to the stagnation of the jet at the tip of the probe. Care must be taken to properly align the pitot tube or an alignment error may result. To quantify the potential alignment error, a streamline orientation investigation was performed. The results of the investigation indicated that the maximum error due to misalignment of the pitot tube from the true streamline orientation of the issuing jet, up to $\pm 15°$, was approximately 2%. When this error is combined to the possible measurement error detailed by Cheremisinoff (1979), the pitot tube can be expected to yield point velocity measurements accurate to ±5%.

All pitot tube readings were obtained in a plane parallel to the orifice opening at the vena-contracta of the jet, with the pitot probe tip oriented perpendicularly inward to the orifice opening. Pressure head differential readings were measured with a water standpipe that was connected to the pitot tube. Approximately 45 pitot tube measurements were taken during each test. These measurements were averaged to determine the initial velocity of the jet at issuance, V_o.

4.4.3 Back-Flushing Pitot-Static Tube

A back-flushing pitot-static tube developed by the United States Bureau of Reclamation (Reclamation) was used to measure the impact velocity of the jet at the

surface of the plunge pool. The pitot-static tube, which was originally intended for mounting on the fuselage of an airplane, was attached to a variable-angle mount fabricated at the Colorado State University Engineering Research Center. The mount allowed the probe to be positioned at any desired orientation, from 0° to 90°. Figure 4.14 shows the back-flushing pitot-static tube and the variable angle mount.

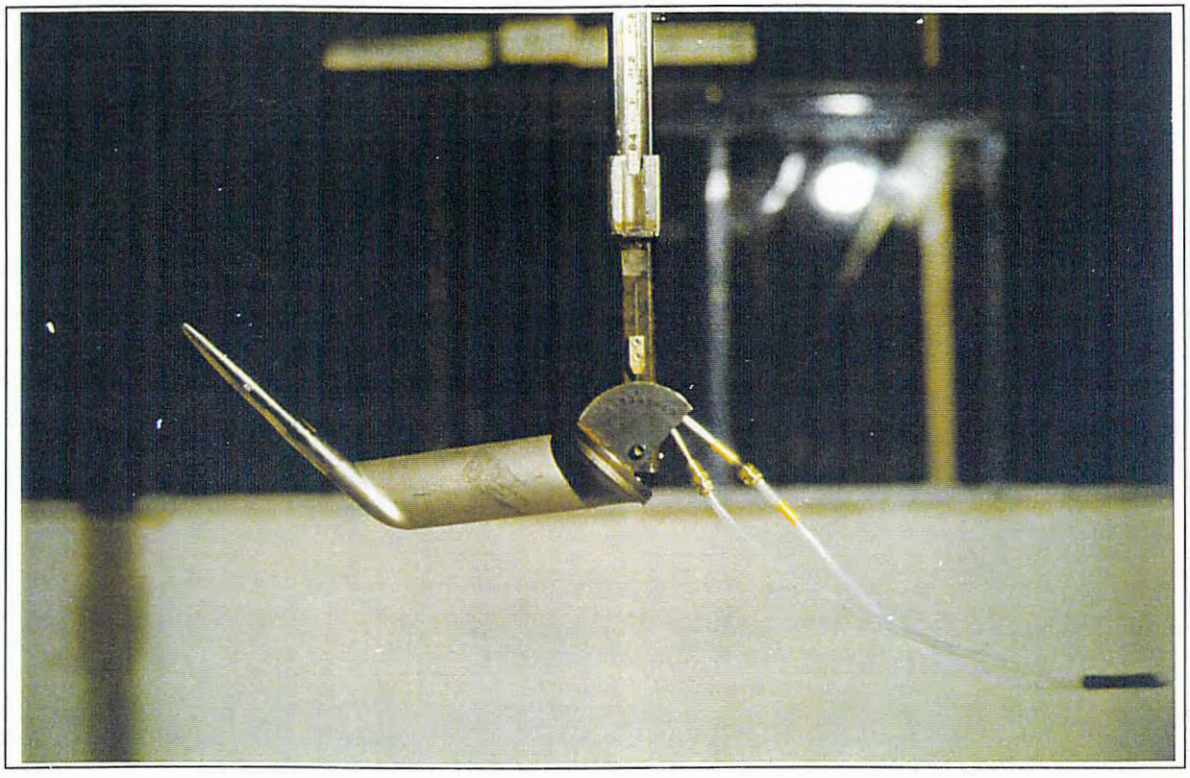

Figure 4.14 Back-flushing pitot-static tube -w- variable-angle mount

Flow is conveyed into the back-flushing pitot-static tube from a constant head source to both the total and static pressure ports. The flow provides continuous back flushing of the pitot tube during operation to maintain a fluid of known density (in this case, water) within the pitot tube and tubing. The pressure supplied to the back-flushing system must be greater than the maximum expected velocity stagnation pressure at the

probe tip in order to keep the highly aerated water in the developed jet from passing air bubbles into the back-flushing system. The constant head supply pressure is maintained with a pressure regulating gage. The back-flushing flow rate to the two pressure ports is controlled by low-flow-rate rotometers. The back-flushing flow rate was 4 l/hr. This rate was sufficient to maintain a continuous flow of water in the back-flushing system and to prevent air bubbles from forming at the pressure ports while the back-flushing pitot-static probe tip was submerged.

A Stathium PM399 differential pressure transducer was employed to measure the pressure difference between the static and total head pressure ports. The voltage output from the pressure transducer was transmitted to a Hewlett Packard 8875 Differential Amplifier. The amplified voltage output traveled to a DAS-1600 data collection board housed inside a 386-25 MHz computer. A software interface created with the Keithley ViewDac data acquisition system integrated the amplified voltage output and determined the average voltage. The pressure transducer calibration was used in a Microsoft Excel spreadsheet to convert the average voltage into a pressure differential. The spreadsheet shifted the converted pressure data to a common origin by subtracting the baseline pressure, which was measured during each test after the back-flushing flow rate was set in air. By subtracting the baseline pressure, the measurements were kept independent of the back-flushing flow rate. Figure 4.15 illustrates the components of the back-flushing pitot-static tube system.

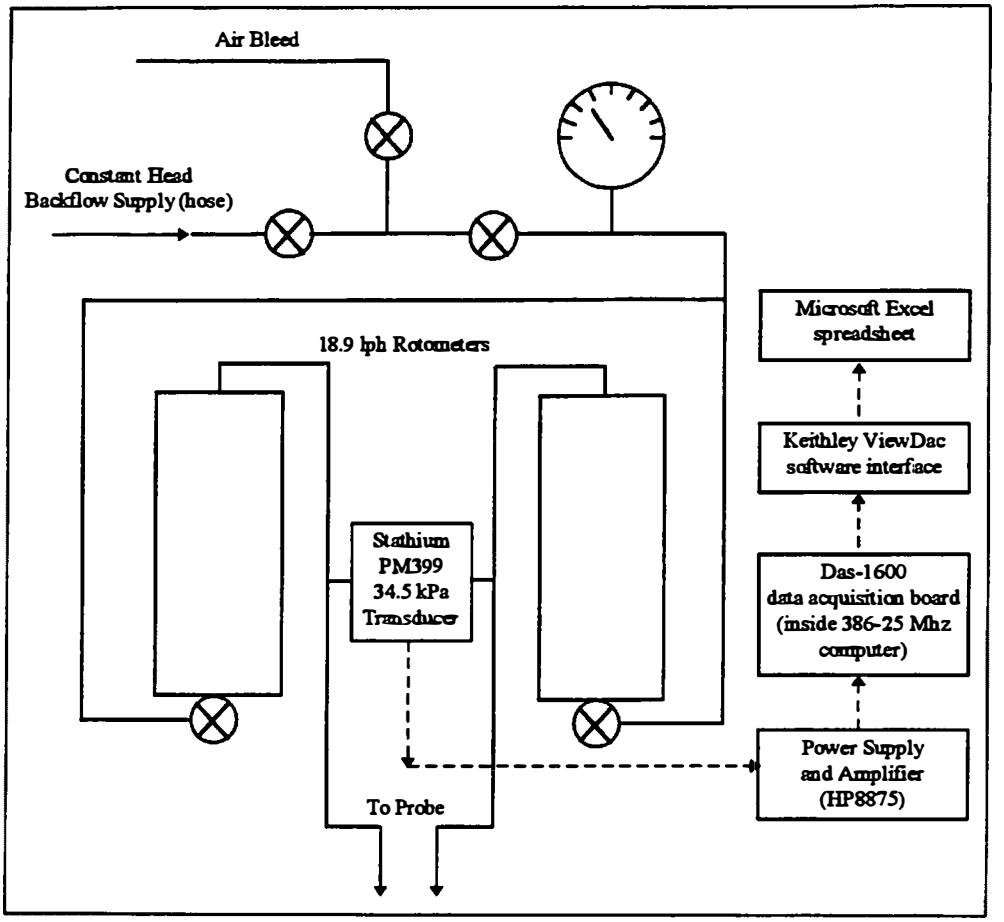

Figure 4.15 Back-flushing velocity probe components

The velocity is then derived from the measured pressure differential of the back-flushing pitot-static tube by:

$$V = \sqrt{\frac{2\Delta p}{\rho}} \tag{4.3}$$

where

V = the velocity of the flow (L/T),

Δp = the measured pressure differential (M/LT), and

ρ = the fluid density (M/L^3).

The pitot tube velocity measurement is dependent on fluid density, as illustrated in Equation 4.3. The developed jet contains a significant amount of entrained air at the point of impact with the plunge pool. As the amount of entrained air varies, so does the density of the two-phase air-water mixture comprising the developed jet. In order to obtain a reliable velocity measurement, it is necessary to calibrate the back-flushing pitot-static tube as a function of air concentration. An investigation of the accuracy of point velocity measurements with the back-flushing pitot-static probe combined with the air concentration meter by Frizell, Ehler, and Mefford (1994) resulted in an error range of ±8%. Additional information regarding the calibration of the back-flushing pitot-static tube and the pressure transducer is presented in Appendix C.

4.4.4 Air Concentration Probe

An air concentration probe developed by Reclamation was used to determine air concentrations at the points where pressure measurements were made with the back-flushing pitot-static tube. The air concentration probe was mounted on the same variable-angle mount used with the back-flushing pitot-static tube. Figure 4.16 shows the air concentration probe along with the variable-angle mount. The air probe serves as an air bubble detector. The air concentration is based on the electrical resistivity difference between air and water. The air probe is comprised of two conductors, a tip of a small insulated platinum wire encased in a stainless steel sleeve. If an air bubble (0.2 mm in

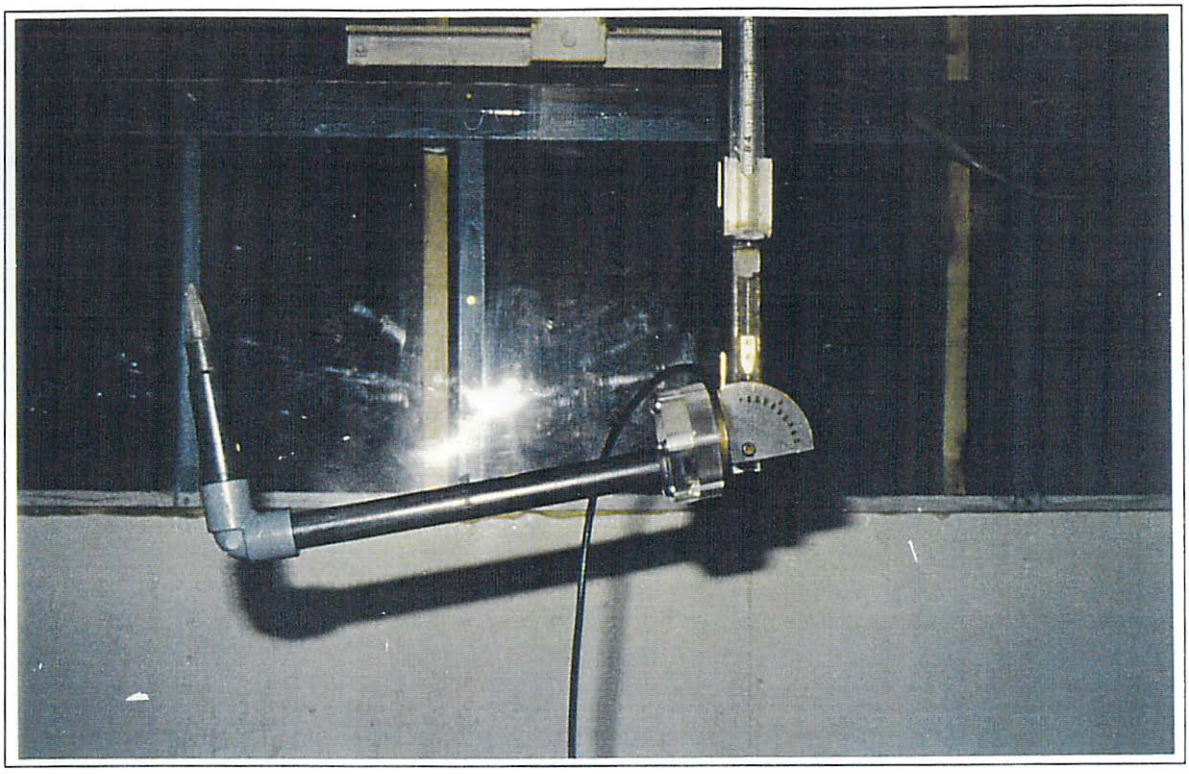

Figure 4.16 Air concentration probe with variable-angle mount

diameter or less) passes across the probe tip, the current between the two conductors is disrupted. When the current is disrupted, the resistance of the circuit increases, simultaneously lowering the voltage across the probe. The probability of encountering air in the air-water mixture is then determined by integrating the resulting signal over a finite period of time. The signal integration is performed by an air concentration meter.

Before the air probe can be operated, two tasks must be completed: first, the anti-plating signal from the air meter must be balanced to prevent the tip of the air probe from acquiring a charge, and second, the gain of the air meter must be adjusted for the conductivity of the water. Once these tasks are accomplished, positioning the air

concentration probe anywhere in the flow field will yield a measurement of the air concentration at that point. Additional information pertaining to the calibration of the air concentration meter is presented in Appendix C.

4.4.5 Acoustic Doppler Velocimeter

A SonTek acoustic Doppler velocimeter was used to make initial measurements of the three-dimensional velocity flow field in the plunge pool. The instrument consists of three modules: an acoustic measurement probe, a signal conditioning module housed inside a waterproof canister, and a signal processing module that is incorporated on a data acquisition board inside a 386-25 MHz computer. The acoustic measurement probe consists of one transmit transducer and three receive transducers as illustrated in Figure 4.17. The receive transducers are mounted on short arms around the transmit transducer at 120° azimuth intervals. The beams of acoustic energy are oriented so that the receive beams intercept the transmit beam at a point located 5 cm below the sensor. The signal conditioning module is connected to the measurement probe by a 1 m long waterproof cable. When in use, the probe and the signal conditioning module are mounted to the point gage positioning system as shown in Figure 4.18. While not in use, the conditioning module and probe tip are removed from the point gage mount and stored for safekeeping. Figure 4.19 shows the signal conditioning module and the acoustic measurement probe.

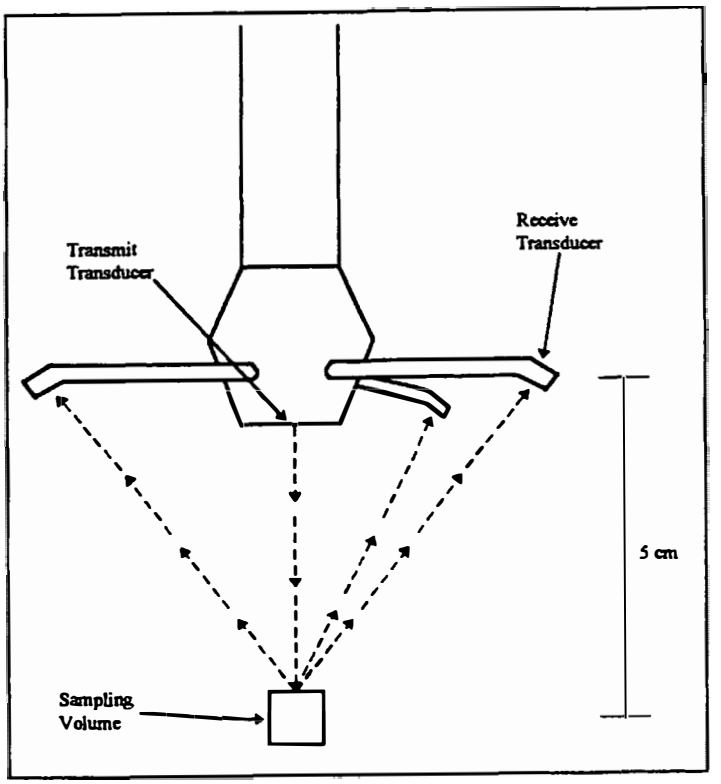

Figure 4.17 Acoustic measurement probe

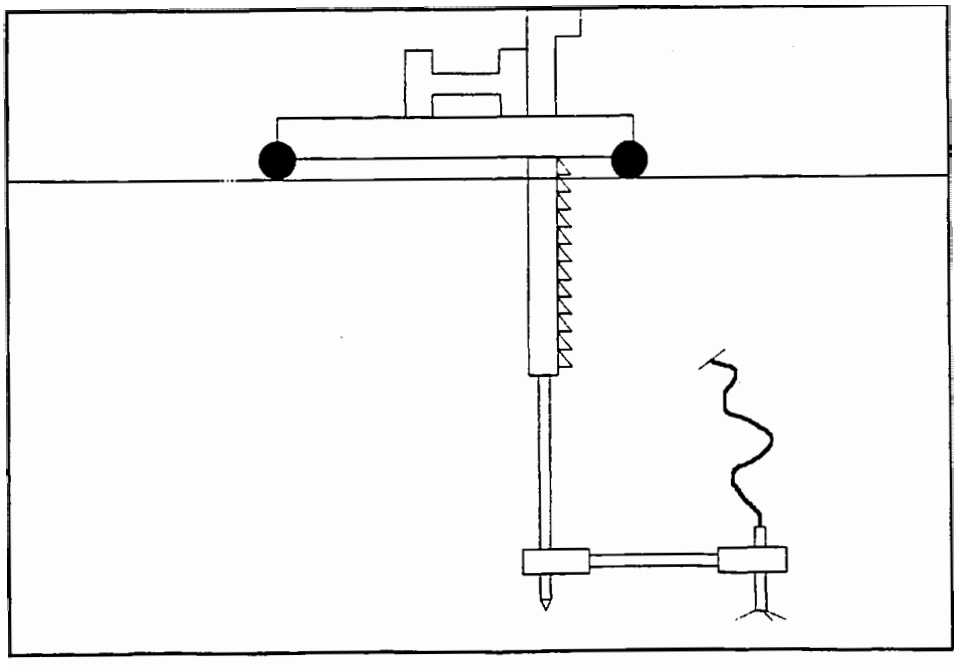

Figure 4.18 Signal conditioning module and acoustic probe on point gage mount

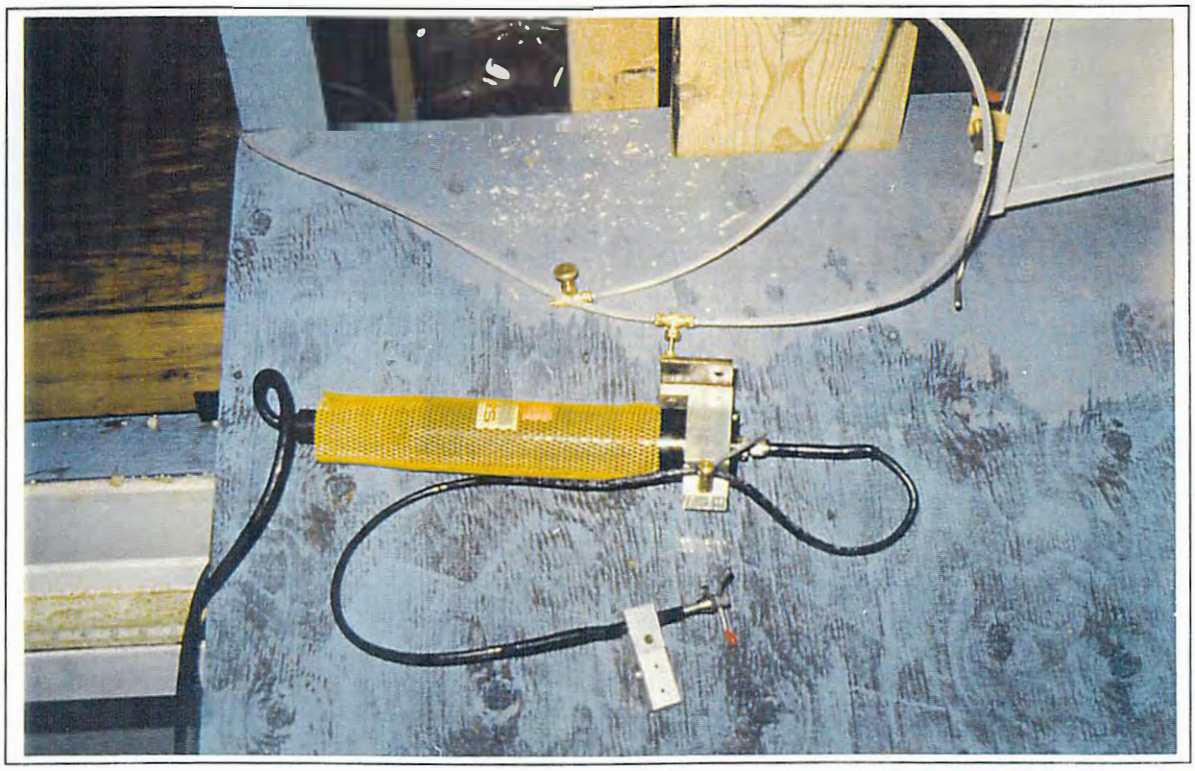

Figure 4.19 Signal conditioning module and acoustic probe

The Doppler shift created by small impurities in the water from a transmitted acoustic energy pulse is measured along three mutually orthogonal axes. The acoustic Doppler velocimeter then calculates a three-dimensional velocity vector from the measured Doppler shift. The sampling duration and rate were chosen to be 1 minute at 5 Hz for each spatial sampling point after performing a frequency / duration analysis. This analysis minimized the amount of data required at each spatial sample point to determine an accurate average velocity. The information from the probe (velocities, signal-to-noise ratios, signal correlations, and standard deviation of velocities in the x, y, and z directions) is stored in compressed binary files on the data acquisition computer. Decompression

programs provided by SonTek were used to extract the velocity, signal-to-noise ratio, and signal correlation information from these files. The average x, y, and z velocity measurements at each spatial sampling point were determined from the extracted velocity data. A study performed by Lohrmann, Cabrera, and Kraus (1994) showed that point velocity measurements taken with the acoustic Doppler velocimeter were accurate to ±2% or less.

4.5 Test Grid and Procedures

The primary variables for the tests performed in the dam overtopping model were the system discharge, Q, vertical fall distance, H_d, and the issuance angle of the jet, ϕ. The system discharge was controlled by a bypass valve diverting water away from the water supply system. The number of stoplogs placed in the steel frame comprising the outlet wall of the test basin established the depth of the plunge pool and subsequent vertical fall distance. The issuance angle of the jet was controlled by loosening the hydraulic dresser coupling on the 8 in supply pipe and rotating the entire section of pipe over the test basin, along with the orifice assembly. Three values of each of the primary variables were selected for a total of 27 independent tests. Table 4.1 illustrates the values of the primary variables used in the testing series.

Table 4.1 Configuration Information for Tests 1-27

Test #	Issuance Angle, ϕ (°)	Discharge, Q (m^3/s)	Fall Distance, H_d (m)
1	15	0.08530	1.45
2	15	0.08530	1.88
3	15	0.08530	1.13
4	15	0.11347	1.86
5	15	0.11347	1.45
6	15	0.11347	1.05
7	15	0.14196	1.86
8	15	0.14196	1.45
9	15	0.14196	1.08
10	0	0.08530	1.87
11	0	0.08530	1.47
12	0	0.08530	1.11
13	0	0.11347	1.85
14	0	0.11347	1.43
15	0	0.11347	1.09
16	0	0.14196	1.84
17	0	0.14196	1.42
18	0	0.14196	1.08
19	30	0.14196	1.82
20	30	0.14196	1.41
21	30	0.08530	1.08
22	30	0.11347	1.83
23	30	0.11347	1.42
24	30	0.11347	1.07
25	30	0.14196	1.85
26	30	0.14196	1.43
27	30	0.14196	1.08

The duration of each test ranged from 8 to 10 hours. Each test consisted of twelve distinct phases which are listed below.

1. Set the jet issuance angle and the number of stoplogs to be used for the test.

2. Turn on the recirculating pump.

3. Set system discharge by checking the pressure measurement at the orifice plate and adjusting the bypass valve as necessary.

4. Using the standard pitot tube mounted on the orifice assembly, profile the vena-contracta of the jet.

5. Using the point gage mounting system without any probes, measure the depth of the plunge pool. (The vertical drop height can be determined from this measurement, the jet issuance angle, and the total distance from the bottom of the orifice assembly to the plunge pool floor.)

6. Bleed the air from the back-flushing pitot-static tube system.

7. Initialize the ViewDac software interface for the back-flushing system and take the zero-offset pressure reading in the air.

8. Obtain pressure readings using the back-flushing pitot-static tube at the plunge pool surface in the impact zone.

9. Balance the anti-plating signal of the air concentration meter and adjust the conductivity gain.

10. Obtain air concentration readings at sample locations used in step 8.

11. Initialize the acoustic Doppler velocimeter computer interface.

12. Obtain acoustic Doppler velocity readings in the plunge pool.

CHAPTER 5

DATA ANALYSIS

An analysis was conducted on the information gathered during the experimental test series to determine which of the three impact velocity predictors; Ervine and Falvey's (1987) method, the differential equation method, or the dimensional equation method more accurately predicted the impact velocity of the model jet at the surface of the plunge pool. In addition, evaluations were performed to determine the validity of the water drop diameter assumption and whether the dimensional equation method should be modified.

5.1 Data Reduction

The data gathered from the experimental testing series was compiled into a database using a spreadsheet interface, Microsoft Excel. The pitot tube measurements obtained at the orifice assembly were averaged to determine the initial velocity, V_o, for each test. An additional analysis was performed to determine if the numerical average accurately quantified the initial velocity. The details of this analysis are presented in Appendix D. The net result was that the numerical average of the individual velocity measurements taken in the plane of the vena-contracta during any given test was

a sufficient quantification of the initial velocity of the jet. The measurements obtained with the back-flushing pitot-static tube and air concentration probe were used to calculate impact velocities. These discreet velocity measurements, 15 for each test, were then averaged to yield the impact velocity of the jet, V_i. Figures 5.1 and 5.2 illustrate profile and frontal views of the model jet, with the location of the sampling planes indicated. Point impact velocities were measured at the intersection of the sampling planes and the water surface.

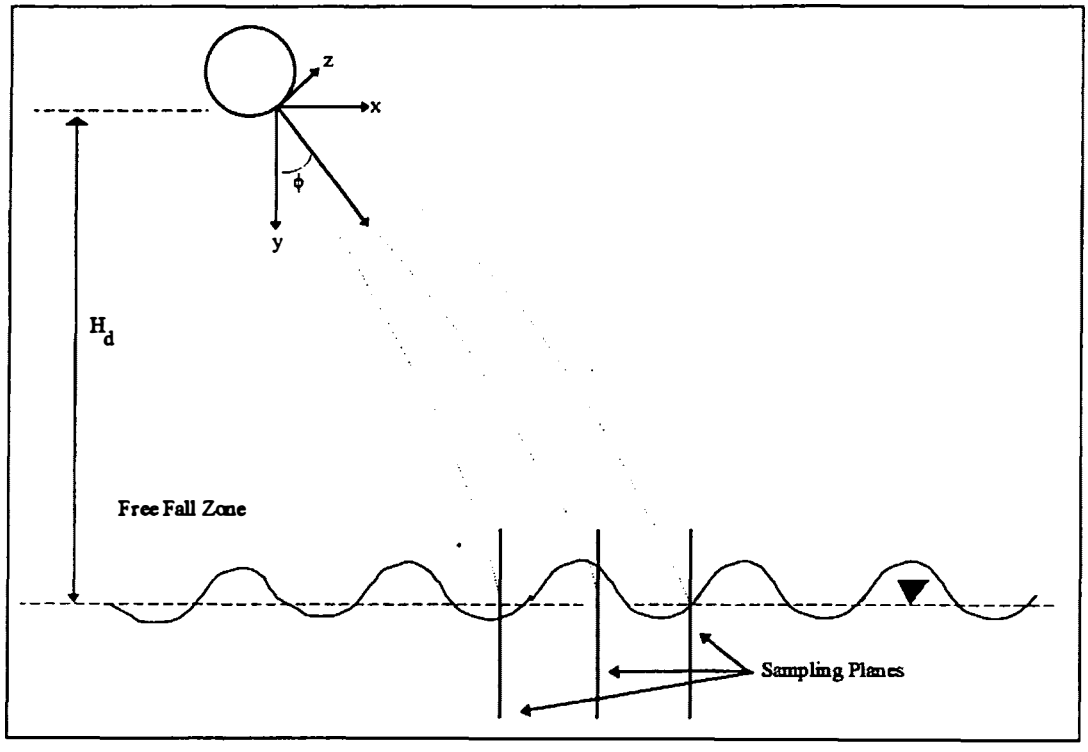

Figure 5.1 Profile view of jet trajectory -w- sampling planes shown

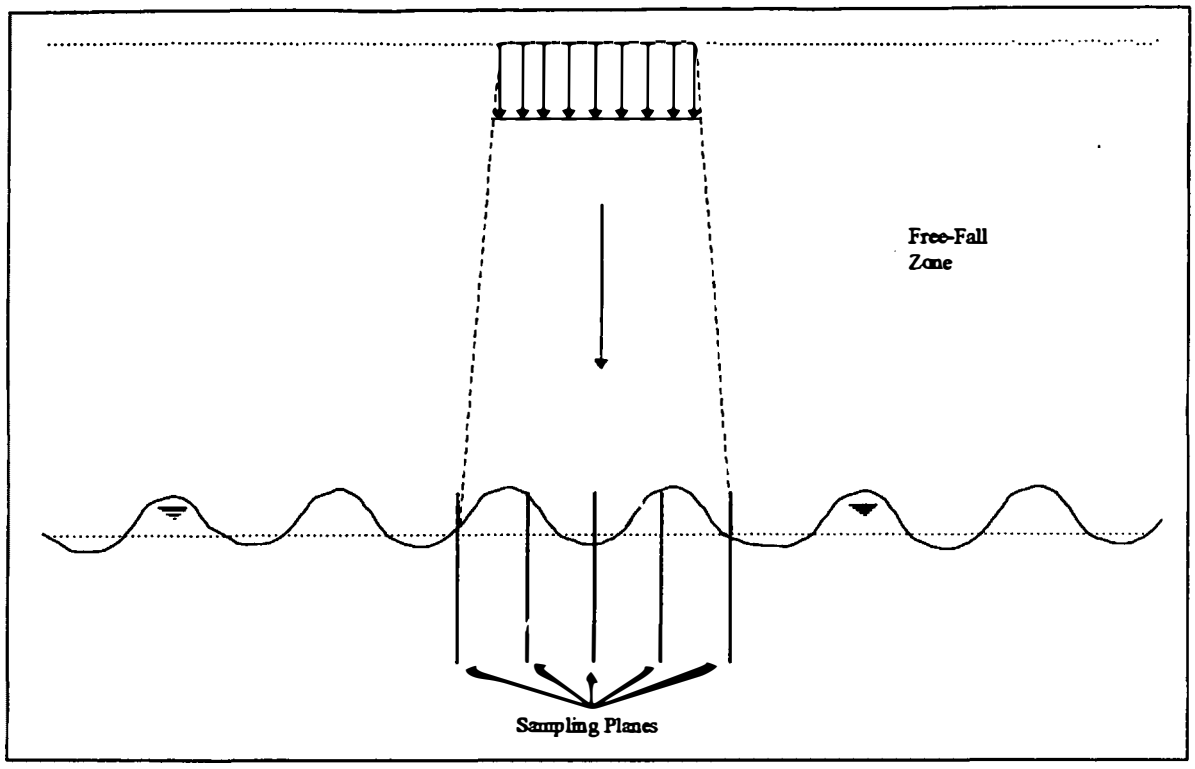

Figure 5.2 Frontal view of jet: impact velocity sampling planes

One of the preliminary results of examining the compiled database was the determination that the data collected using the acoustic Doppler velocimeter was unreliable in the turbulent region beneath the impact area. The poor performance of the acoustic Doppler velocimeter was attributed to the high turbulence level and the large amount of air entrained in the region (the water surface and ensuing flow zones). A summary of the data collected using the pitot tube, back-flushing pitot-static tube, orifice plate, and air concentration probe is presented in Table 5.1.

Table 5.1 Summary of Collected Data

Test #	Volumetric Discharge Q (m3/s)	Jet Issuance Angle ϕ (°)	Vertical Drop Height H_d (m)	Initial Average Velocity V_o (m/s)	Initial Maximum Velocity max V_o (m/s)	Initial Minimum Velocity min V_o (m/s)	Standard Deviation Of Initial Velocity σV_o (m/s)	Measured Impact Velocity V_i (m/s)	Maximum Impact Velocity max V_i (m/s)	Minimum Impact Velocity min V_i (m/s)	Standard Deviation Of Impact Velocity σV_i (m/s)
1	0.08530	15	1.45	2.64	3.24	2.05	0.38	3.70	4.89	3.03	0.83
2	0.08530	15	1.88	2.70	3.08	2.02	0.32	4.09	4.82	3.45	0.54
3	0.08530	15	1.13	2.63	3.08	1.92	0.36	1.70	2.30	1.03	0.45
4	0.11347	15	1.86	4.10	4.65	3.06	0.49	4.22	4.51	3.96	0.25
5	0.11347	15	1.45	3.93	4.42	3.11	0.43	1.80	2.93	0.84	1.04
6	0.11347	15	1.05	4.00	4.48	3.16	0.42	0.79	0.85	0.73	0.06
7	0.14196	15	1.86	4.89	5.71	1.95	0.81	4.99	6.14	4.07	0.79
8	0.14196	15	1.45	4.70	5.48	1.95	0.81	4.80	5.14	4.48	0.28
9	0.14391	15	1.08	4.79	5.58	1.98	0.83	4.44	4.80	4.11	0.33
10	0.08530	0	1.87	2.86	3.34	1.94	0.40	3.96	4.31	3.44	0.35
11	0.08530	0	1.47	2.75	3.21	1.94	0.37	3.87	5.30	3.24	0.82
12	0.08530	0	1.11	2.72	3.19	1.94	0.38	3.90	4.68	3.17	0.64
13	0.11347	0	1.85	3.78	4.42	2.03	0.58	4.63	5.94	3.90	0.86
14	0.11347	0	1.43	3.79	4.42	2.03	0.58	3.57	5.12	2.67	0.87
15	0.11347	0	1.09	3.97	4.48	3.17	0.42	4.40	6.11	3.27	1.14
16	0.14196	0	1.84	4.96	5.61	3.97	0.53	3.61	5.01	2.64	1.03
17	0.14196	0	1.42	5.12	5.81	4.08	0.56	4.06	6.16	3.00	1.14
18	0.14196	0	1.08	5.00	5.65	4.00	0.54	4.53	7.28	2.84	1.75
19	0.14196	30	1.82	2.95	3.36	2.37	0.33	3.80	4.56	3.17	0.60
20	0.14196	30	1.41	2.90	3.32	2.33	0.33	2.99	3.65	2.39	0.44
21	0.08530	30	1.08	2.83	3.23	2.25	0.32	4.08	5.29	3.39	0.68
22	0.11347	30	1.83	4.21	4.73	3.39	0.45	3.57	4.08	3.32	0.26
23	0.11347	30	1.42	4.03	4.53	3.24	0.43	4.04	5.29	3.57	0.47
24	0.11347	30	1.07	3.87	4.39	3.07	0.41	4.20	4.78	3.68	0.37
25	0.14196	30	1.85	5.07	5.72	4.14	0.53	4.38	6.38	3.53	1.10
26	0.14196	30	1.43	4.97	5.60	4.08	0.51	3.49	4.40	3.10	0.45
27	0.14196	30	1.08	4.79	5.43	3.94	0.50	3.34	4.41	2.71	0.56

Table 5.1 Summary of Collected Data

Test #	Volumetric Discharge	Jet Issuance Angle	Vertical Drop Height	Initial Average Velocity	Initial Maximum Velocity	Initial Minimum Velocity	Standard Deviation Of Initial Velocity	Measured Impact Velocity	Maximum Impact Velocity	Minimum Impact Velocity	Standard Deviation Of Impact Velocity
	Q (m3/s)	ϕ (°)	H_d (m)	V_o (m/s)	$\max V_o$ (m/s)	$\min V_o$ (m/s)	σV_o (m/s)	V_i (m/s)	$\max V_i$ (m/s)	$\min V_i$ (m/s)	σV_i (m/s)
1	0.08530	15	1.45	2.64	3.24	2.05	0.38	3.70	4.89	3.03	0.83
2	0.08530	15	1.88	2.70	3.08	2.02	0.32	4.09	4.82	3.45	0.54
3	0.08530	15	1.13	2.63	3.08	1.92	0.36	1.70	2.30	1.03	0.45
4	0.11347	15	1.86	4.10	4.65	3.06	0.49	4.22	4.51	3.96	0.25
5	0.11347	15	1.45	3.93	4.42	3.11	0.43	1.80	2.93	0.84	1.04
6	0.11347	15	1.05	4.00	4.48	3.16	0.42	0.79	0.85	0.73	0.06
7	0.14196	15	1.86	4.89	5.71	1.95	0.81	4.99	6.14	4.07	0.79
8	0.14196	15	1.45	4.70	5.48	1.95	0.81	4.80	5.14	4.48	0.28
9	0.14391	15	1.08	4.79	5.58	1.98	0.83	4.44	4.80	4.11	0.33
10	0.08530	0	1.87	2.86	3.34	1.94	0.40	3.96	4.31	3.44	0.35
11	0.08530	0	1.47	2.75	3.21	1.94	0.37	3.87	5.30	3.24	0.82
12	0.08530	0	1.11	2.72	3.19	1.94	0.38	3.90	4.68	3.17	0.64
13	0.11347	0	1.85	3.78	4.42	2.03	0.58	4.63	5.94	3.90	0.86
14	0.11347	0	1.43	3.79	4.42	2.03	0.58	3.57	5.12	2.67	0.87
15	0.11347	0	1.09	3.97	4.48	3.17	0.42	4.40	6.11	3.27	1.14
16	0.14196	0	1.84	4.96	5.61	3.97	0.53	3.61	5.01	2.64	1.03
17	0.14196	0	1.42	5.12	5.81	4.08	0.56	4.06	6.16	3.00	1.14
18	0.14196	0	1.08	5.00	5.65	4.00	0.54	4.53	7.28	2.84	1.75
19	0.14196	30	1.82	2.95	3.36	2.37	0.33	3.80	4.56	3.17	0.60
20	0.14196	30	1.41	2.90	3.32	2.33	0.33	2.99	3.65	2.39	0.44
21	0.08530	30	1.08	2.83	3.23	2.25	0.32	4.08	5.29	3.39	0.68
22	0.11347	30	1.83	4.21	4.73	3.39	0.45	3.57	4.08	3.32	0.26
23	0.11347	30	1.42	4.03	4.53	3.24	0.43	4.04	5.29	3.57	0.47
24	0.11347	30	1.07	3.87	4.39	3.07	0.41	4.20	4.78	3.68	0.37
25	0.14196	30	1.85	5.07	5.72	4.14	0.53	4.38	6.38	3.53	1.10
26	0.14196	30	1.43	4.97	5.60	4.08	0.51	3.49	4.40	3.10	0.45
27	0.14196	30	1.08	4.79	5.43	3.94	0.50	3.34	4.41	2.71	0.56

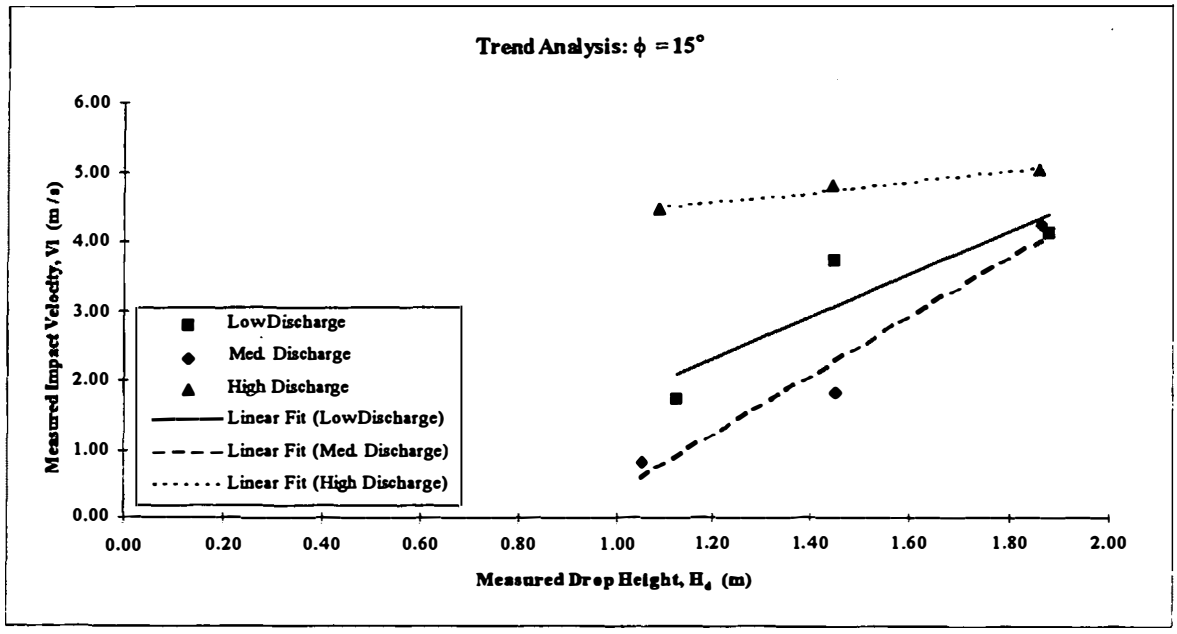

Figure 5.4 Trend analysis between H_d and V_i at $\phi = 15°$

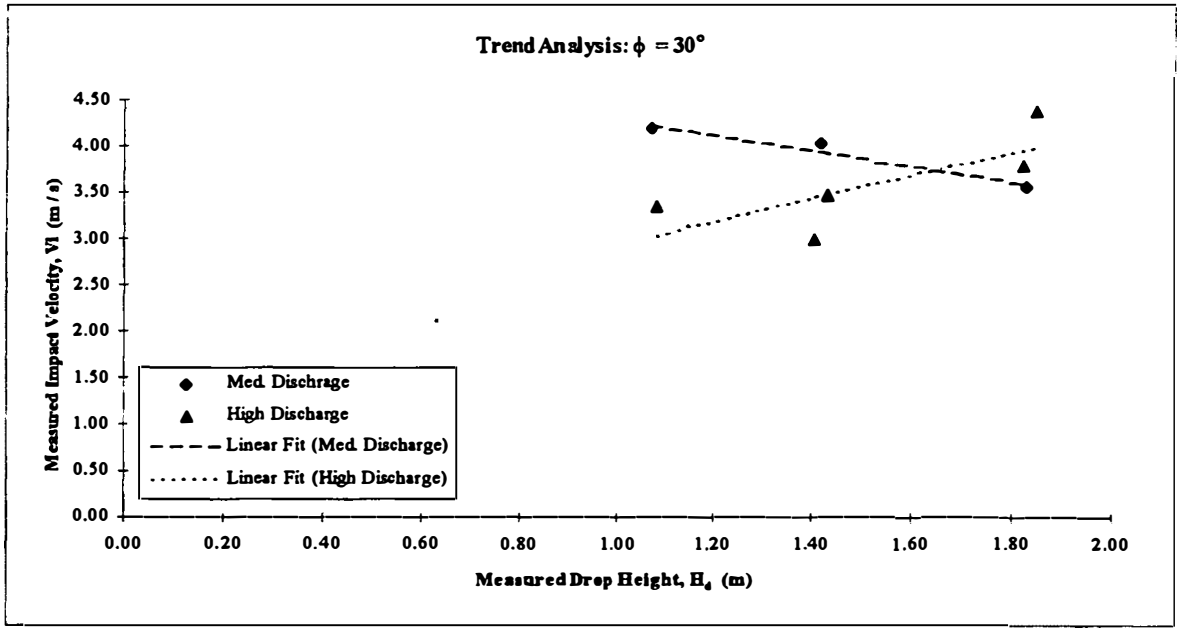

Figure 5.5 Trend analysis between H_d and V_i at $\phi = 30°$

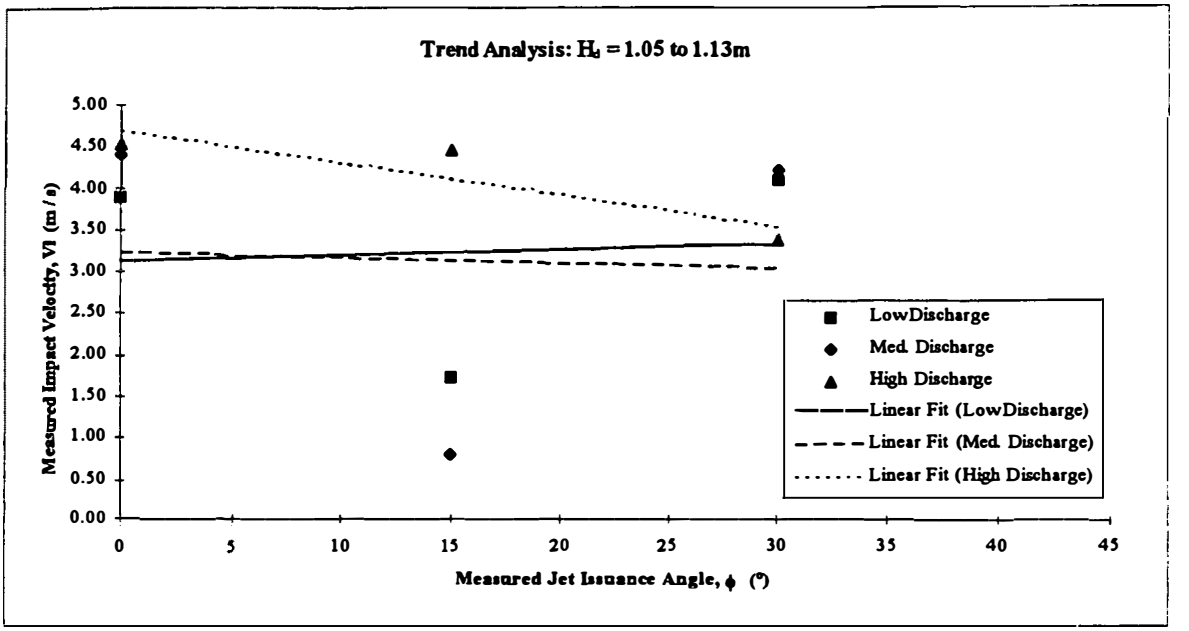

Figure 5.6 Trend analysis between ϕ and V_i at H_d = 1.05 to 1.13 m

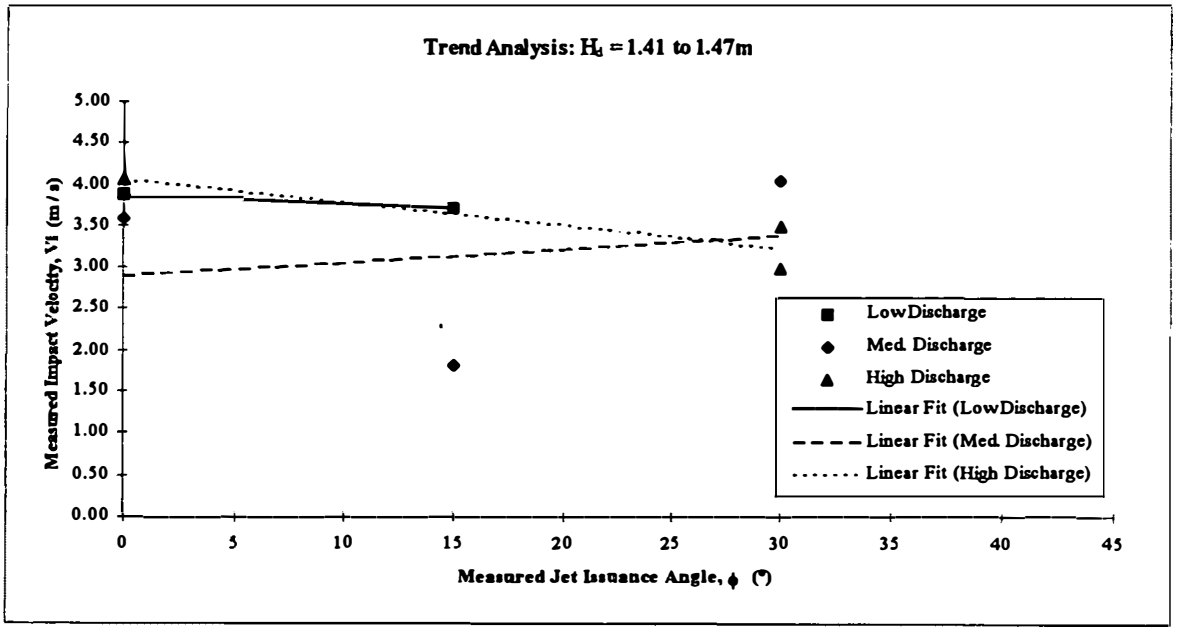

Figure 5.7 Trend analysis between ϕ and V_i at H_d = 1.41 to 1.47 m

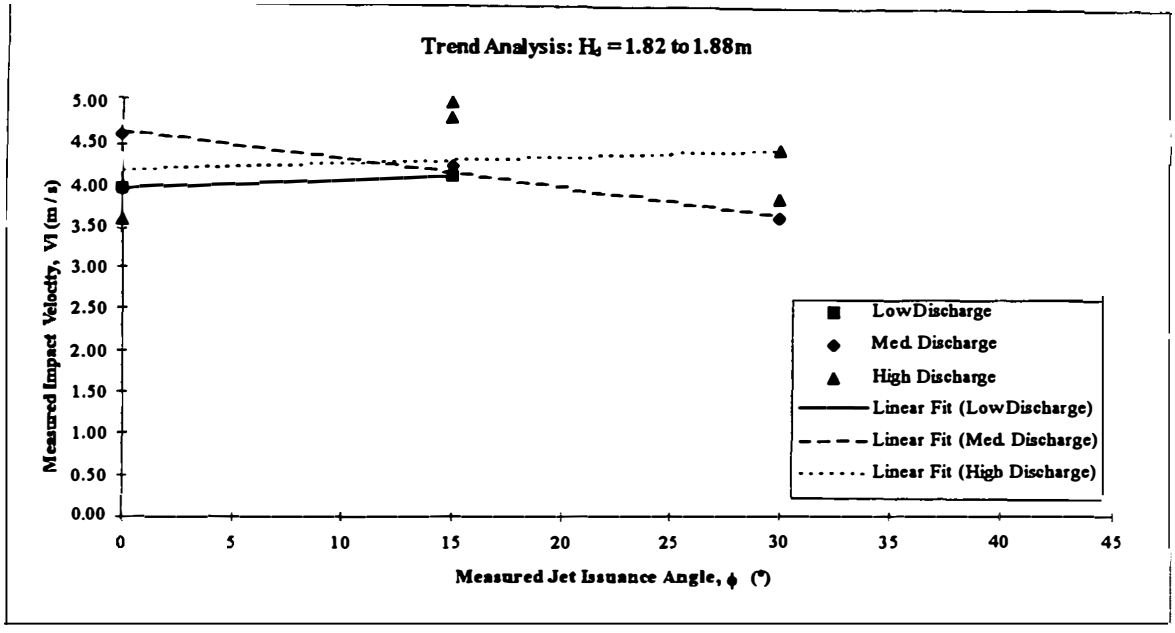

Figure 5.8 Trend analysis between ϕ and V_i at H_d = 1.82 to 1.88 m

In Figures 5.3 through 5.5, there appears to be a general correlation between the impact velocity and the drop height. From Newton's second law of motion, the sum of the forces acting on any body is equivalent to the product of the mass of the body and the acceleration produced by the forces acting on that body. In all 27 tests, the impact velocity of the plunging jet was observed to be substantially less than the terminal velocity calculated using the differential prediction method. Since terminal velocity had not been reached in any of the tests, the correlation between impact velocity with increasing drop height aligns with Newton's second law. The trend lines with negative slopes observed in Figure 5.3 and Figure 5.5 are the results of averaging a single impact velocity; the standard deviations of the computed impact velocities are of the same order as the range of the trend.

Observation of Figures 5.6 through 5.8 indicates that a correlation does not exist between issuance angle and impact velocity for the range of angles tested. The jet trajectory length through the air is essentially the same for the vertical drop height and jet fall path between the orifice and the water surface. As shown in Figure 5.9, the trajectory length can be approximated by the vertical drop height and the issuance angle.

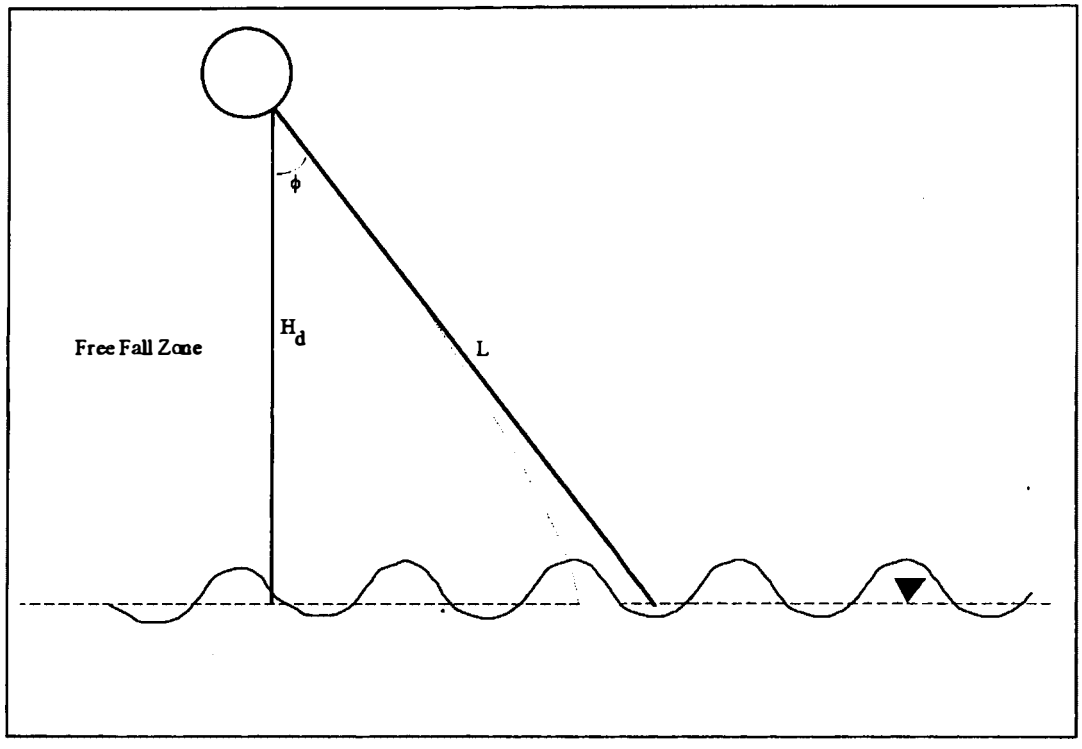

Figure 5.9 Trigonometric approximation of jet trajectory length

A first-order approximation of the error introduced in trajectory length can be calculated. The trigonometric relationship applied to Figure 5.9 is

$$L = H_d \sec(\phi) \tag{5.1}$$

where

L = the approximated jet trajectory length (L),

H_d = the vertical drop height (L), and

ϕ = the issuance angle of the jet (°).

At the largest issuance angle tested, $\phi = 30°$, the approximate jet trajectory length is only 15.5% greater than the vertical drop height. Since the true jet trajectory length is parabolic, the maximum error in using the drop height instead of the jet trajectory as the travel length, as assumed in the dimensional method and Ervine and Falvey's method, is less than the first-order approximation. Care must be applied when using the results of these experiments to situations with issuance angles larger than 30° because the trajectory length assumption may no longer be valid.

5.3 Predicted vs. Observed Results for Velocity Predictors

Impact velocities were calculated for all 27 tests using the dimensional equation predictor (Equation 3.16), the differential equation predictor (Equations 3.1 - 3.15), and Ervine and Falvey's (1987) dragless predictor (Equation 2.4). A summary of measured and calculated impact velocities, V_i, is presented in Table 5.2. The values in Table 5.2 illustrate the effective differences between the three different impact velocity predictors.

Table 5.2 Comparison of Measured & Predicted Impact Velocities

Test #	Measured Impact Velocity V_i (m/s)	Calculated Impact Velocity (Erv. & Fal.) V_i^* (m/s)	Calculated Impact Velocity (Dim. Eq.) V_i^* (m/s)	Calculated Impact Velocity (Diff. Eq.) V_i^* (m/s)	Calculated Impact Velocity (Mod. Dim. Eq.) V_i^* (m/s)
1	3.70	5.95	4.23	5.20	4.28
2	4.09	6.64	4.64	5.58	4.71
3	1.70	5.38	3.88	4.84	3.92
4	4.22	7.31	4.28	5.94	4.32
5	1.80	6.63	4.07	5.63	4.10
6	0.79	6.06	3.84	5.35	3.86
7	4.99	7.77	4.17	6.17	4.19
8	4.80	7.10	4.05	5.92	4.07
9	4.44	6.65	3.95	5.76	3.96
10	3.96	6.70	4.58	5.62	4.58
11	3.87	6.03	4.23	5.25	4.23
12	3.90	5.41	3.85	4.86	3.86
13	4.63	7.11	4.33	5.85	4.33
14	3.57	6.51	4.07	5.58	4.07
15	4.40	6.10	3.86	5.38	3.86
16	3.61	7.79	4.15	6.20	4.16
17	4.06	7.36	4.06	6.10	4.06
18	4.53	6.80	3.99	5.88	3.99
19	3.80	6.67	4.52	5.58	4.76
20	2.99	6.00	4.14	5.21	4.35
21	4.08	5.41	3.82	4.84	4.00
22	3.57	7.32	4.25	5.91	4.39
23	4.04	6.64	4.05	5.60	4.17
24	4.20	6.00	3.84	5.27	3.94
25	4.38	7.88	4.15	6.16	4.22
26	3.49	7.27	4.05	5.96	4.11
27	3.34	6.65	3.95	5.70	4.00

Ervine and Falvey's method (1987) has no provision for deceleration of the developed jet due to air drag. As a result, velocities predicted using Ervine and Falvey's method are on average 18.5% greater than those predicted by the differential method and 62.5% greater than those predicted by the dimensional method. The differential method computed velocities are 36.9% greater than those calculated by the dimensional method and 41.9% greater than measured in the model. The assumption of constant drag over the fall length used by the dimensional method has the greatest velocity dampening effect of the three velocity predictors.

In order to determine which of the three velocity predictors most accurately estimated the measured impact velocities, two approaches were considered; a numerical analysis and a graphical analysis.

The numerical analysis was conducted by computing the percent differences between the measured impact velocities and the estimated impact velocities from the three estimation methods; Ervine and Falvey's (1987) method, the differential method, and the dimensional method. The percent difference between the observed impact velocity and the estimated impact velocity, expressed as a percentage of the observed impact velocity can be computed from:

$$D = \frac{B - A}{A} * 100 \qquad (5.2)$$

where

D = percent difference (dimensionless),

A = the observed impact velocity (L/T), and

B = the estimated impact velocity (L/T).

Standard statistical measures (mean, maximum, minimum, and sample standard deviation) were then calculated for each of the three samples (the collected percent differences for each estimation method). These statistical measures are presented in Table 5.3:

Table 5.3 Numerical Analysis of Measured & Predicted Impact Velocities

Statistical Measure of Percent Difference	Ervine & Falvey (1987) Method (outliers removed)	Differential Method (outliers removed)	Dimensional Method (outliers removed)
Mean	68.4%	41.9%	4.1%
Maximum	115.9%	74.3%	38.5%
Minimum	32.7%	18.8%	-16.4%
Standard Deviation	23.9%	17.8%	14.2%

Of the three methods considered, it appears that the dimensional method is the most accurate, with a mean percent difference of 4.1% from the observed data.

The graphical analysis consisted of a set of three scatter plots, with the predicted impact velocities on the abscissa and the observed impact velocities on the ordinate. Perfect correlation would be obtained if the experimental points plot adjacent to or on a 45° line extending from the origin. Figures 5.10 - 5.12 present the comparison scatter plots.

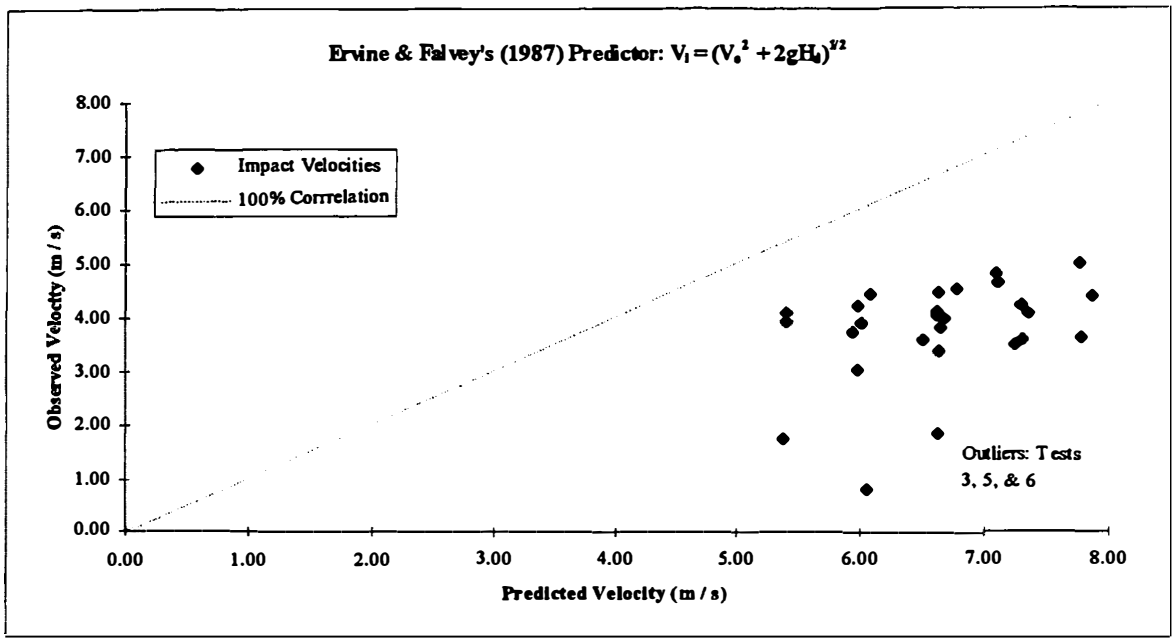

Figure 5.10 Correlation graph for Ervine & Falvey's predictor

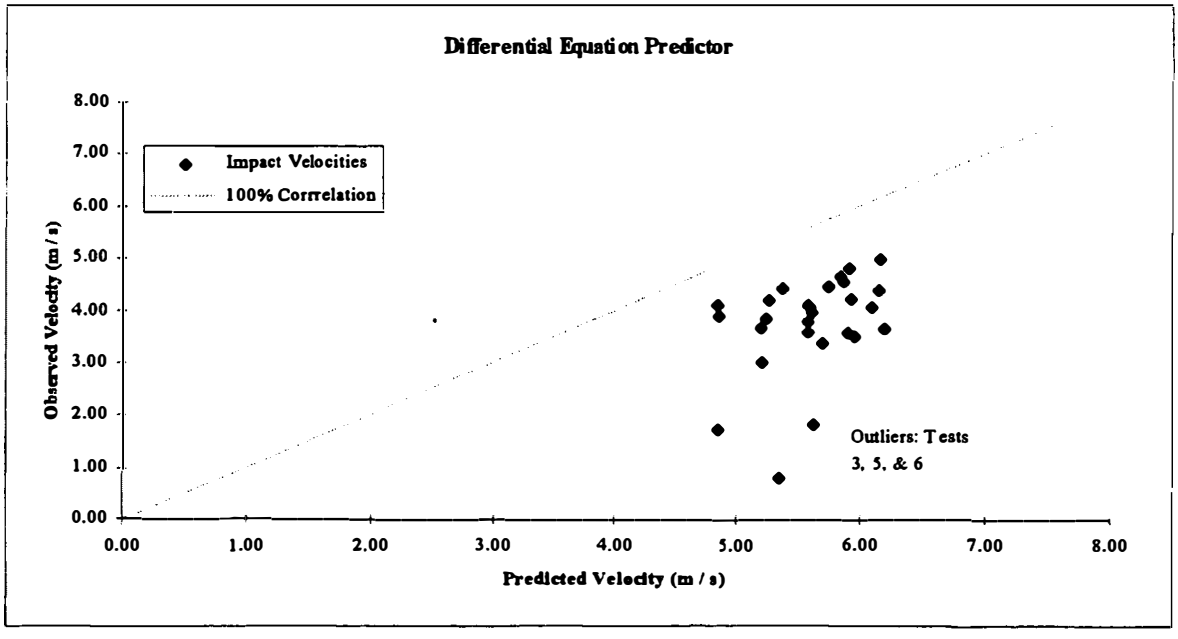

Figure 5.11 Correlation graph for differential equation predictor

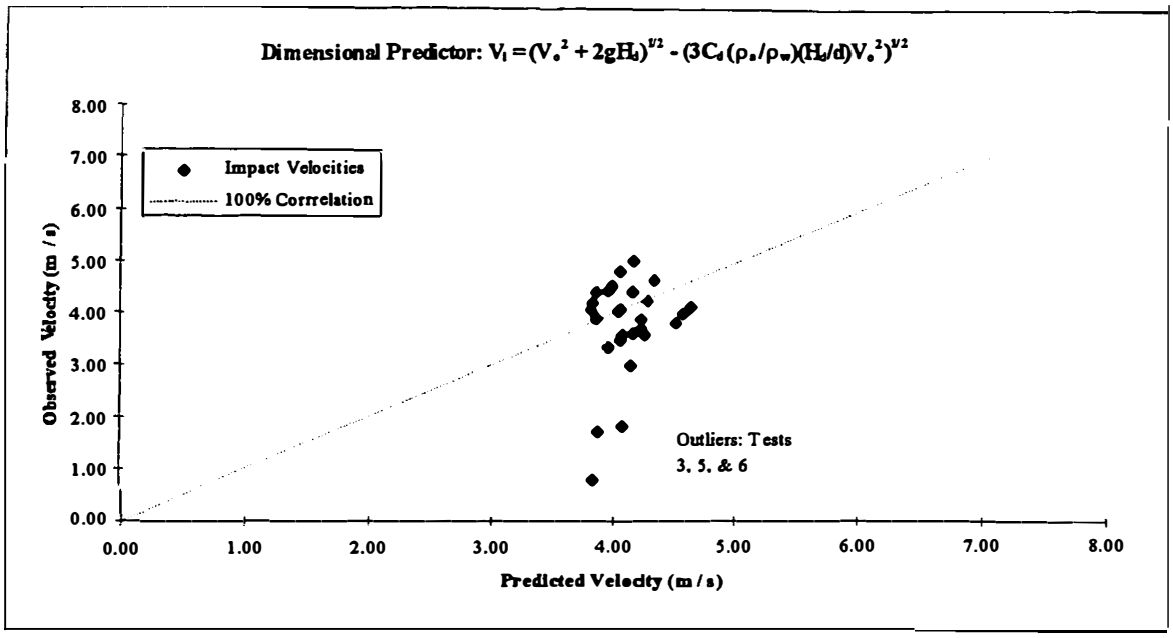

Figure 5.12 Correlation graph for dimensional equation predictor

The most accurate prediction technique of the three considered appears to be the dimensional equation technique as the main data cluster centers about the 45° line. The differential equation technique and the Ervine and Falvey (1987) technique tend to overestimate the impact velocity of the developed jet. Three outliers were identified in the measured impact velocity database; Tests 3, 5, and 6. When these three points were removed from the numerical analysis, the average percent difference between the velocities predicted by the dimensional equation method and those observed in the model fell from 27.4% to 4.1%. Similar reductions in the average percent difference between predicted and measured impact velocities were obtained for the other methods as well.

Although the trend analysis presented in Section 5.2 did not indicate a relation between the issuance angle and the impact velocity, an analysis was performed by replacing the drop height, H_d, by the first-order approximation of the jet trajectory

length, $H_d \sec(\phi)$ in the dimensional method. The modified dimensional method prediction equation is now expressed as:

$$V_i = \sqrt{V_o^2 + 2gH_d \sec(\phi)} - \sqrt{3C_d\left(\frac{\rho_a}{\rho_w}\right)\left(\frac{H_d \sec(\phi)}{d}\right)V_o^2} \qquad (5.3)$$

where

C_d = drag coefficient (nondimensional),

ρ_a = air density (M/L^3),

ρ_w = water density (M/L^3),

H_d = the vertical distance from the outlet to the surface of the pool (L),

d = diameter of a sphere having the same volume as a water drop (L),

g = acceleration due to gravity (L/T^2),

V_o = initial velocity of the jet (L/T),

V_i = impact velocity of the jet at the plunge pool surface (L/T), and

ϕ = the issuance angle of the jet (°).

Once the predicted impact velocities were calculated with the modified dimensional impact velocity equation, numerical and graphical analyses similar to the ones conducted for the three other prediction methods were performed. The results of the numerical analysis is presented in Table 5.4 and the results of the graphical analysis are illustrated in Figure 5.13.

Table 5.4 Additional Numerical Analysis of Measured & Predicted Impact Velocities

Statistical Measure of Percent Difference	Modified Dimensional Method (outliers removed)
Average	5.6%
Maximum	45.4%
Minimum	-16.0%
Standard Deviation	15.3%

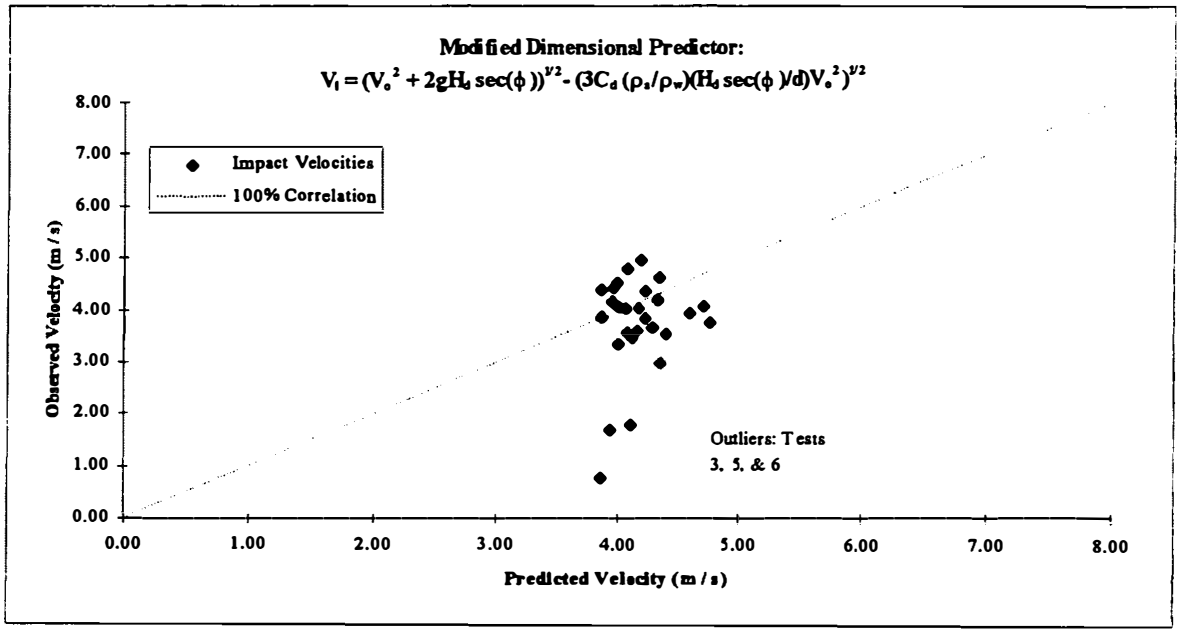

Figure 5.13 Correlation graph for modified dimensional equation predictor

As indicated in Table 5.4 and Figure 5.13, the substitution of the first-order approximation of the jet trajectory length for the vertical drop height in the prediction equation does not substantially improve the predictive capability of the original dimensional method. In fact, the substitution slightly lowers the predictive capability of the dimensional method from an average error of 4.1% to an average error of 5.6%.

5.4 Validity of Water Drop Diameter Assumption

An analysis was performed to determine the validity of the water drop diameter sizing assumption used in the dimensional prediction method. By algebraically manipulating the dimensional impact velocity prediction equation, Equation 3.16, an expression was formulated that calculated the diameter of a constituent water drop within the developed jet as a function of initial velocity, impact velocity, drop height, drag coefficient, and the densities of air and water. The water drop diameter is

$$d_i = \frac{3C_d\left(\frac{\rho_a}{\rho_w}\right)H_d V_o^2}{V_o^2 + 2gH_d - 2V_i\sqrt{V_o^2 + 2gH_d} + V_i^2} \tag{5.4}$$

where

C_d = drag coefficient (nondimensional),

ρ_a = air density (M/L^3),

ρ_w = water density (M/L^3),

H_d = the vertical distance from the outlet to the surface of the pool (L),

d_i = diameter of a water drop at impact with the plunge pool (L),

g = acceleration due to gravity (L/T^2),

V_o = measured initial velocity of the jet (L/T), and

V_i = measured impact velocity of the jet at the plunge pool surface (L/T).

The water particle impact diameters were calculated for all 27 tests using Equation 5.4. Table 5.5 presents the results of a comparison of the assumed and computed water particle diameters. The average calculated water drop diameter for 100% correlation was 6.11 mm ± 2.56 mm, discounting the aforementioned outliers. (The largest computed impact diameter was 10.57 mm and the smallest was 2.29 mm, outliers removed.) Since the computed diameters were of the same order of magnitude as the assumed value, 6.00 mm, it appears that the diameter sizing assumption used in the dimensional impact velocity predictor is reasonable.

Table 5.5 Diameter Assumption Analysis

Test #	Assumed Equivalent Drop Diameter d (mm)	Drop Diameter for 100% Correlation d* (mm)
1	6.00	3.50
2	6.00	3.68
3	6.00	1.01
4	6.00	5.78
5	6.00	1.69
6	6.00	1.06
7	6.00	10.05
8	6.00	10.57
9	6.00	8.94
10	6.00	3.59
11	6.00	4.17
12	6.00	6.34
13	6.00	7.53
14	6.00	4.16
15	6.00	10.50
16	6.00	4.53
17	6.00	6.00
18	6.00	9.19
19	6.00	3.38
20	6.00	2.29
21	6.00	8.56
22	6.00	4.03
23	6.00	5.98
24	6.00	8.65
25	6.00	6.84
26	6.00	4.34
27	6.00	3.99

Average Computed Drop Diameter for 100% Corr. (outliers removed) (mm)	Std. Deviation Of Computed Drop Diameter for 100% Corr. (outliers removed) (mm)
6.11	2.56

Maximum Computed Drop Diameter for 100% Corr. (outliers removed) (mm)	Mminmum Computed Drop Diameter for 100% Corr. (outliers removed) (mm)
10.57	2.29

5.5 Potential Errors

With any experiment, potential errors exist when measurements are taken. This project is no exception. Specifically, errors may exist in all four measured quantities; volumetric discharge, initial velocity, impact velocity, and plunge pool velocities. The source of these inaccuracies may be human error, which is unmeasurable, or instrument error, which can be estimated. Table 5.6 shows the estimated accuracies of each of the instruments used in this project.

Table 5.6 Instrument Accuracies

Probe	Used to determine	Approximate accuracy
Orifice Plate	Volumetric Discharge, Q	±2%
Pitot Tube	Initial Velocity, V_o	±5%
Back-Flushing Pitot-Static Tube	Impact Velocity, V_i	±8%
Air Concentration Probe	Impact Velocity, V_i	±15%
Acoustic Doppler Velocimeter	Plunge Pool Velocities, V	±2%

By summing the estimated accuracies of the back-flushing pitot-static tube and the air concentration probe, the cumulative possible error in the impact velocity measurement is ±23%.

CHAPTER 6

CONCLUSIONS & RECOMMENDATIONS

In an effort to improve the state-of-the-art for the prediction of scour at the foundation and abutment areas of overtopping dams, an experimental study was performed. The goal of the study was to predict the impact velocity of a turbulent, developed jet at the point of incidence with the plunge pool. In order to achieve the stated study objectives, the following tasks were accomplished:

- A comprehensive literature review was performed.
- Based upon the review, three viable prediction methods were derived; Ervine and Falvey's (1987) method, the dimensional technique, and the differential equation technique.
- A sidewall orifice assembly was developed to simulate a free-trajectory, developed, overtopping jet.
- A model test facility was designed and constructed.
- Instrumentation was developed and/or acquired, including an orifice plate with manometer, a simple pitot tube at the orifice, a back-flushing pitot-static tube, an air concentration probe, and an acoustic Doppler velocimeter, to directly measure appropriate variables in the model facility.
- Twenty-seven independent tests were conducted to gather data for the evaluation of the performance of the two velocity prediction techniques.
- The test data were analyzed and a prediction technique was recommended.

6.1 Conclusions

After consideration of the literature reviewed, theoretical analysis, and results of the experimental program, the following findings are concluded:

1. Two types of overtopping jets occur naturally; undeveloped jets and developed jets.

2. The characteristics of developed jets differ than those of the undeveloped jets studied by Ervine and Falvey (1987). Undeveloped jets contain a solid core of non-aerated water surrounded by a shell of discreet water particles, while developed jets consist solely of discreet water particles.

3. Aerodynamic drag is a significant decelerating force on the developed jet in the atmosphere due to the absence of a solid core of non-aerated water.

4. Three impact velocity prediction techniques were identified and evaluated. The dimensional technique predicted impact velocities that were accurate to ±4.1%, the differential technique impact velocities were accurate ±41.9%, and Ervine and Falvey's (1987) technique impact velocities were accurate to ±68.4%.

5. Issuance angle did not effect impact velocity when the angle was less than or equal to 30° (measured from the vertical).

6. The vertical drop height has a significant correlation to the measured impact velocity.

7. The substitution of a first-order approximation to the jet trajectory length into the dimensional equation technique was not effective in improving the accuracy of the technique.

8. The water drop diameter sizing assumption of 6 mm used in the dimensional and differential prediction methods was validated.

6.2 Recommendations

Due to the complexity and difficulties experienced in this study, further research should be performed before implementing the results of the study to full-size overtopping dams. The following specific recommendations are made:

1. Validate the dimensional equation technique with tests performed on a larger, preferably near-prototype scale. Aeration effects may change at near-prototype scale and the possibility of the free-falling jet reaching terminal velocity with greater vertical drop height exists.

2. Investigate the water drop diameter sizing assumption further. A method to determine the size, or distribution of sizes, of the discreet water particles within a developed jet could lead to greater accuracy of the dimensional equation and differential equation techniques.

3. Improve the instrumentation used for measuring velocities and air concentrations in high velocity, turbulent conditions. The uncertainty in the probe measurements must be considered when using the results of this study. When taken as a whole, the uncertainty of the probes used to measure impact velocity can lead to errors on the order of ±23%.

BIBLIOGRAPHY

Abramovich, G.N., (1963)., *The Theory of Turbulent Jets*, English translation published by M.I.T. Press, Massachusetts.

Albertson, M.L., Dai, Y.B., Johnson, R.A., and Rouse, H. (1950)., Diffusion of Submerged Jets, *Transactions of the ASCE*, Vol 115.

Belatos, S. and Rajaratnam, N., (1973)., Plane Turbulent Impinging Jets, *Journal of Hydraulic Research.*, Vol. 11 No. 1.

Bormann, Noel E., Julien, Pierre Y., (May 1, 1991)., Scour Downstream of Grade-Control Structures, *ASCE Journal of Hydraulic Engineering.* V. 117, No. 5.

Cheremisinoff, Nicholas P., (1979)., *Applied Fluid Flow Measurement*, Marcel, Dekker, Inc.

Cola, R., (1965)., Energy Dissipation of a High Velocity Vertical Jet Entering a Basin, *Inter. Assc. Hydr. Res. - Proceedings.*, 11th Congress, Vol. 1, paper no. 1.52

Ervine, D.A., and Falvey, H.T., March (1987)., Behavior of Turbulent Water Jets in the Atmosphere and in Plunge Pools, *Proceeding of the Institution of Civil Engineers, Part 2*, 83.

Frizell, Kathleen H., Ehler, David G., and Mefford, Brent W., (1994)., Developing Air Concentration and Velocity Probes for Measuring Highly Aerated, High-Velocity Flow, *Fundamentals and Advancements in Hydraulic Measurements and Experimentation*, ASCE.

George, Robert L., December (1980)., *Impinging Jets*, Engineering and Research Center, U.S. Dept of the Interior.

Gilley, J.R., and von Bernuth, R.D., (1984)., Sprinkler Droplet Size Distributions Estimations from Single Leg Test Data, *Transactions of the American Society of Agricultural Engineers.*, Vol. 27 No. 5.

Goertler, H., (1942.), Berechnung von Aufgaben der freien Turbulenz auf Grund eines neuen Naherungsansatzes, *Z.A.M.M.*, 22.

Hinkle, S.E., (1991)., A Modified Empirical Drag Coefficient For Water Drop Ballistics, *Transactions of the American Society of Agricultural Engineers.*, Vol. 7 No. 6.

Julien, P.Y., Stein, O.R., Alonso, C.V., (1993)., Mechanics of Jet Scour Downstream of a headcut, *Journal of Hydraulic Research.*, Vol. 31 No. 6.

Lajos, T., Preszler, L., and Blahó, M., (1978)., The Estimation Of The Error At The Flow Rate Measurement By Pitot-Static Tube, *Flow Measurement of Fluids*, North-Holland Publishing Co.

Lohrmann, Atle, Cabrera, Ramon, and Kraus, Nicholas C., (1994)., Acoustic-Doppler Velocimeter (ADV) For Laboratory Use, *Fundamentals and Advancements in Hydraulic Measurements and Experimentation*, ASCE.

Myers, G.E., Schauer, J.J., and Eustis, R.H., (1961), The plane turbulent wall jet I, Jet development and friction factor. *Tech. Rep., 1, Department of Mechanical Engineering, Stanford University.*

Rajaratnam, N., (1976)., *Turbulent Jets*, Elsevier Scientific Publishing Co.

Seginer, Ido, (1965)., Tangential Velocity of Sprinkler Drops, *Transactions of the American Society of Agricultural Engineers.*, Vol. 8 No. 1.

Serafim, J.L., and Coutinho-Rodrigues, J.M., (1989)., Statistics of dam failures: a preliminary report, *International Water Power and Dam Construction.*, Vol 41 No. 4.

Stearns, R.F., Johnson, R.R., Jackson, R.M., and Larson, C.A., (1951)., *Flow Measurement with Orifice Meters*, D. Van Nostrand Company, Inc.

Stein, O.R., Julien, P.Y., (1993)., Criterion Delineating The Mode Of Headcut Migration, *Journal of Hydraulic Engineering.*, Vol. 119 No.1.

Tollimien, W., (1926.), Berechung turbulenter Ausbreitungsvorgänge, *Zeitschrift für angewandle Mathematik und Mechanik, Vol. 6.*, (English translation, N.A.C.A., TM 1085, 1945.)

Verhoff, A., (1963.), The two-dimensional turbulent wall jet with and without an external stream, Report 626, *Princeton Univ.*

Wang, P.K., and Pruppacher, H.R., (1977)., Acceleration to Terminal Velocity of Cloud and Raindrops, *Journal of Applied Meteorology.*, Vol. 16 No. 3

Ylidez, D., and Uzucek, E., (1994)., Prediction of scour depth from free falling flip bucket jets, *International Water Power and Dam Construction.*, Vol 46 No. 11.

Zijnen, B.G. Van der Hegge, (1958)., Measurements of the velocity distribution in a plane turbulent jet of air, *Appl. Sci. Res.*, *Sect. A*, 7.

APPENDIX A

IMPACT VELOCITY PREDICTION PROGRAM

The computer program that predicts the velocity of a turbulent, developed jet at the point of impact with the surface of the plunge pool was written with Microsoft Visual Basic for Applications, contained within Microsoft Excel for Windows version 5.0c. The program requires that the user have an operable copy of Microsoft Excel for Windows version 5.0c or later.

After the user has started Excel, the file "TRAJECT.XLS" should be loaded. This workbook file contains three pages. The first page, labeled "Interface", is the user interface for the program. The second page, labeled "Graphs", plots the predicted jet trajectory after the program has been run. The third page, labeled "Code Page", contains the code for the velocity prediction program. Figures A.1 and A.2 show sample views of the "Interface" and "Graphs" pages.

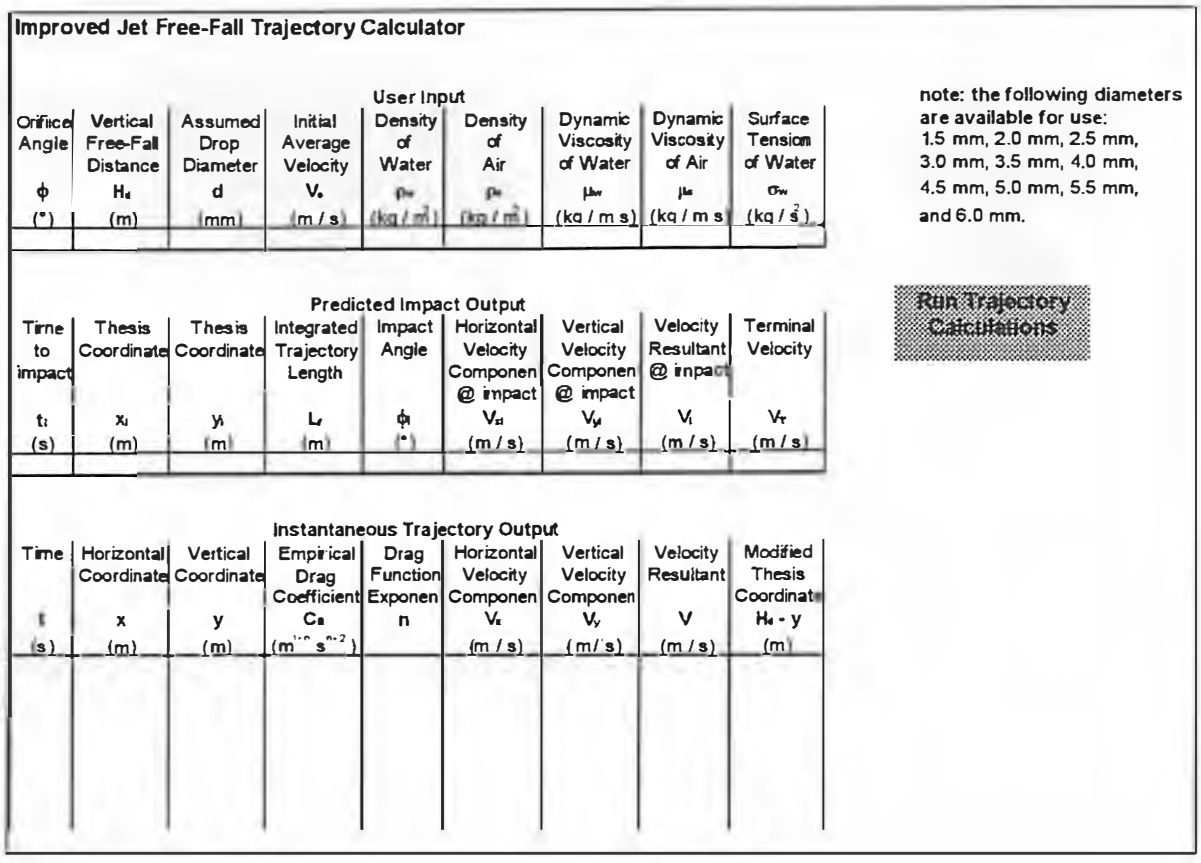

Figure A.1 "Interface" page of computer program

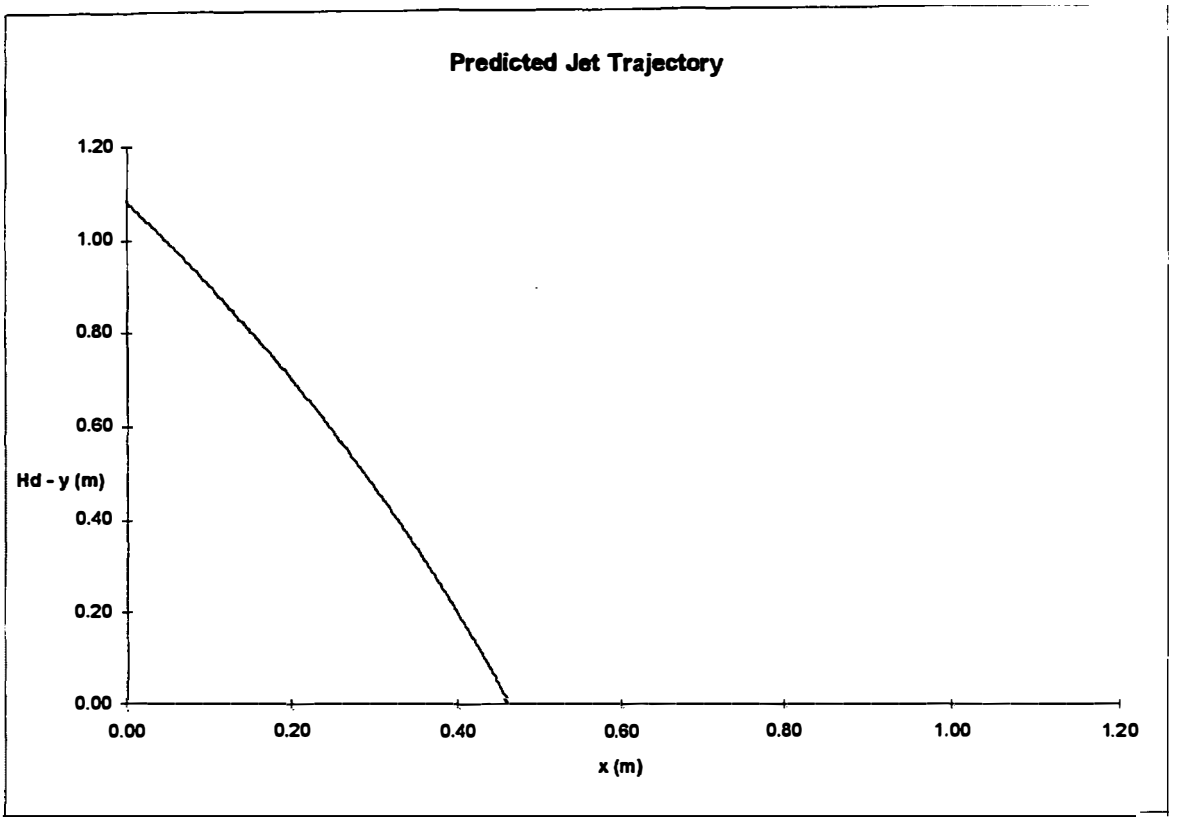

Figure A.2 Sample output of the "Graphs" page of the computer program

To use the program, all the user has to do is switch to the "Interface" page, type in the values of the nine requested variables underneath the "User Input" label, and click the "Run Trajectory Calculations" button with the cursor arrow. The program will notify the user once it has completed its calculations. The results of the program are printed in the spreadsheet cells underneath the "Predicted Impact Output" label. The values printed under the "Instantaneous Trajectory Output" label are used by the program to graph the predicted trajectory of the jet and should not be altered. A complete listing of the program code is shown below:

```
'Set global options
   Option Explicit      'Forces all variables to be explicitly declared
   Option Base 1        'The default first element of an array is 1

'Declare module level variables.
   Dim ax As Double          'X component of acceleration (internal)
   Dim ay As Double  'Y component of acceleration (internal)
   Dim Bo As Double          'Bond number (internal)
   Dim b0 As Double          'Empirical coefficient (internal)
   Dim b1 As Double          'Empirical coefficient (internal)
   Dim b2 As Double          'Empirical coefficient (internal)
   Dim b3 As Double          'Empirical coefficient (internal)
   Dim b4 As Double          'Empirical coefficient (internal)
   Dim b5 As Double          'Empirical coefficient (internal)
   Dim b6 As Double          'Empirical coefficient (internal)
   Dim b7 As Double          'Empirical coefficient (internal)
   Dim Cn() As Double        'Modified drag coefficient (output)
   Dim d  As Double          'Diameter of water drop (input)
   Dim dt As Double          'Time increment (internal)
   Dim g As Double           'Gravitational acceleration (internal)
   Dim Hd As Double          'Vertical Drop Height (input)
   Dim k As Double           'Iteration counter (internal)
   Dim k1 As Double          'Iteration counter (internal)
   Dim Lf As Double          'Integrated fall length (output)
   Dim n() As Double         'Drag function exponent (output)
   Dim P As Double           'Physical property number (internal)
   Dim phi As Double         'Diffuser angle (input)
   Dim phi1 As Double        'Impact angle (output)
   Dim PI As Double          'Mathematical constant (internal)
   Dim pa As Double          'Density of air (input)
   Dim pw As Double          'Density of water (input)
   Dim Ret As Double         'Reynolds number @ terminal velocity (internal)
   Dim s() As Double         'Discreet path lengths (internal)
   Dim sigma As Double       'Surface tension of water (input)
   Dim time() As Double      'Time counter (output)
   Dim ua As Double          'Dynamic viscosity of air (input)
   Dim uw As Double          'Dynamic viscosity of water (input)
   Dim V() As Double         'Resultant fall velocity array (output)
   Dim Vt As Double          'Instantaneous terminal velocity (output)
   Dim Vx() As Double        'X component of fall velocity (output)
   Dim Vy() As Double        'Y component of fall velocity (output)
   Dim x() As Double         'Horizontal distance from orifice (output)
   Dim Xf As Double          'Used to compute Yf (internal)
   Dim y() As Double         'Vertical distance from orifice (output)
   Dim Yf As Double          'Used to compute Ret (internal)
```

```
Dim DialogStyle
Dim Response

Sub InputLoader()  'Loads data from spreadsheet & sets constants
  g = 9.8066
  d = Worksheets("Interface").Cells(10, 4) * 0.001
  dt = 0.001
  Hd = Worksheets("Interface").Cells(10, 3)
  Lf = 0
  pa = Worksheets("Interface").Cells(10, 7)
  phi = Worksheets("Interface").Cells(10, 2)
  PI = 3.14159625
  pw = Worksheets("Interface").Cells(10, 6)
  sigma = Worksheets("Interface").Cells(10, 10)
  ua = Worksheets("Interface").Cells(10, 9)
  uw = Worksheets("Interface").Cells(10, 8)
  b0 = -5.00015
  b1 = 5.23778
  b2 = -2.04914
  b3 = 0.475294
  b4 = -0.0542819
  b5 = 0.00238449
  Bo = (d ^ 2 * (pw - pa) * g) / sigma
  P = (sigma ^ 3 * pa ^ 2) / (ua ^ 4 * (pw - pa) * g)
  Xf = Log(0.75 * Bo * P ^ (1 / 6))
  Yf = b0 + b1 * Xf + b2 * Xf ^ 2 + b3 * Xf ^ 3 + b4 * Xf ^ 4 + b5 * Xf ^ 5
  Ret = P ^ (1 / 6) * Exp(Yf)
  Vt = (Ret * ua) / (d * pa)
  If d = 0.0015 Then
    b6 = 1.596
    b7 = 0.209
  ElseIf d = 0.002 Then
    b6 = 1.718
    b7 = 0.142
  ElseIf d = 0.0025 Then
    b6 = 1.756
    b7 = 0.203
  ElseIf d = 0.003 Then
    b6 = 1.772
    b7 = 0.33
  ElseIf d = 0.0035 Then
    b6 = 1.797
    b7 = 0.472
  ElseIf d = 0.004 Then
    b6 = 1.825
```

```
    b7 = 0.631
  ElseIf d = 0.0045 Then
    b6 = 1.85
    b7 = 0.796
  ElseIf d = 0.005 Then
    b6 = 1.905
    b7 = 0.917
  ElseIf d = 0.0055 Then
    b6 = 1.954
    b7 = 1.016
  ElseIf d = 0.006 Then
    b6 = 2.024
    b7 = 1.058
  End If
End Sub

Sub DimArray()     'Sizes and initializes all arrays
  ReDim Cn(2000)
  ReDim n(2000)
  ReDim s(2000)
    s(1) = 0
  ReDim time(2000)
    time(1) = 0
  ReDim V(2000)
    V(1) = Worksheets("Interface").Cells(10, 5)
  ReDim Vx(2000)
    Vx(1) = V(1) * Sin(phi * PI / 180)
  ReDim Vy(2000)
    Vy(1) = V(1) * Cos(phi * PI / 180)
  ReDim x(2000)
    x(1) = 0
  ReDim y(2000)
    y(1) = 0
End Sub

Sub OutputResults()  'Outputs the results of the program to the spreadsheet
  For k1 = 1 To k - 1
    Worksheets("Interface").Cells(k1 + 28, 2) = time(k1)
    Worksheets("Interface").Cells(k1 + 28, 3) = x(k1)
    Worksheets("Interface").Cells(k1 + 28, 4) = y(k1)
    Worksheets("Interface").Cells(k1 + 28, 5) = Cn(k1)
    Worksheets("Interface").Cells(k1 + 28, 6) = n(k1)
    Worksheets("Interface").Cells(k1 + 28, 7) = Vx(1)
    Worksheets("Interface").Cells(k1 + 28, 8) = Vy(k)
    Worksheets("Interface").Cells(k1 + 28, 9) = V(k1)
```

```
      Worksheets("Interface").Cells(k1 + 28, 10) = Hd - y(k1)
    Next k1
    Worksheets("Interface").Cells(20, 2) = time(k - 1)
    Worksheets("Interface").Cells(20, 3) = x(k - 1)
    Worksheets("Interface").Cells(20, 4) = y(k - 1)
    Worksheets("Interface").Cells(20, 5) = Lf
    Worksheets("Interface").Cells(20, 6) = phi1
    Worksheets("Interface").Cells(20, 7) = Vx(k - 1)
    Worksheets("Interface").Cells(20, 8) = Vy(k - 1)
    Worksheets("Interface").Cells(20, 9) = V(k - 1)
    Worksheets("Interface").Cells(20, 10) = Vt
End Sub

Sub Trajectory()   'Main Algorithm
    InputLoader
    DimArray
    For k = 1 To 1999
        V(k) = Sqr(Vx(k) ^ 2 + Vy(k) ^ 2)
        n(k) = b6 + b7 * (V(k) / Vt)
        If V(k) > Vt Then n(k) = b6 + b7
        Cn(k) = g / Vt ^ n(k)
        ax = - Cn(k) * V(k) ^ (n(k) - 1) * Vx(k)
        ay = g - Cn(k) * V(k) ^ (n(k) - 1) * Vy(k)
        Vx(k + 1) = Vx(k) + ax * dt
        Vy(k + 1) = Vy(k) + ay * dt
        x(k + 1) = x(k) + Vx(k) * dt + 1 / 2 * ax * dt ^ 2
        y(k + 1) = y(k) + Vy(k) * dt + 1 / 2 * ay * dt ^ 2
        s(k + 1) = Sqr((x(k + 1) - x(k)) ^ 2 + (y(k + 1) - y(k)) ^ 2)
        time(k + 1) = time(k) + dt
        If y(k + 1) > Hd Then
            k = k + 1
            Exit For
        End If
    Next k
    V(k) = Sqr(Vx(k) ^ 2 + Vy(k) ^ 2)
    phi1 = Atn((x(k) - x(k - 1)) / (y(k) - y(k - 1))) * (180 / PI)
    For k1 = 2 To k
        Lf = Lf + s(k1)
    Next k1
    OutputResults
    Beep
    MsgBox "Trajectory calculations finished."
End Sub
```

APPENDIX B

ORIFICE ASSEMBLY DESIGN TEST SERIES

Between April and July, 1994, a test series was conducted to design the orifice assembly used in the dam overtopping model. The following paragraphs are brief accounts of the results of eighteen tests performed during the test series.

Development Test No. 1 (4/14/94): This was the initial orifice assembly design. The orifice assembly used a hole pattern in a triangular shape (large end upstream) with 265 in^2 of open hole area. The blades on the orifice assembly were set at a uniform 1.6 in opening. The resulting jet was skewed significantly toward the west wall of the test facility (upstream) and was observed to be extremely non-uniform.

Development Test No. 2 (5/3/94): For this test, the hole pattern in the delivery pipe was widened to 374 in^2 of open surface area. This had the effect of reducing jet skewness toward the upstream wall. However, the non-uniformity of the jet was not improved.

Development Test No. 3 (5/5/94): The hole pattern in the delivery pipe was opened further (391 in^2). No noticeable changes were observed.

Development Test No. 4 (5/6/94): The hole pattern was opened again (396 in^2). The jet skewness was reduced slightly and the jet became more uniform (but not by a significant amount).

Demonstration (5/16/94): For this site visitation, the hole pattern was opened more (401 in^2). The blades on the orifice assembly were closed by 0.1 in such that the opening was a uniform 1.5 in. There was no observable change in the uniformity of the jet and skewness was seen to increase.

Development Test No. 5 (5/17/94): The hole pattern was closed to a different configuration (391 in^2). This had the effect of decreasing the skewness of the jet and increasing the non-uniformity of the jet.

Development Test No. 6 (5/18/94): The blades on the orifice assembly were closed to a uniform 1.4 in. There were no discernible changes in the properties of the jet, but the available outlet pressure changed from 2 psi to 3 psi.

Development Test No. 7 (5/19/94): The blades on the orifice assembly were closed further to a uniform 1.3 in. This had no observable effect on the jet system.

Development Test No. 8 (5/23/94): The hole pattern was opened up (400 in^2). Jet skewness increased and the uniformity of the jet improved.

Development Test No. 9 (5/24/94): The hole pattern was changed, but the same surface area as Test No. 8 was kept. The blades on the orifice assembly were opened to a uniform 1.4 in. This had no discernible change in the jet.

Development Test No. 10 (5/25/94): The orifice opening was changed to a trapezoidal configuration (1.4 in on the downstream end and 1.2 in on the upstream end). This didn't effect the jet appreciably.

Development Test No. 11 (5/27/94): The hole pattern was closed to a different configuration (386 in^2). This was done to recreate Test No. 4 so that the early portion of testing could be compared with the later testing to decide which hole pattern to further develop. Unfortunately, there was no discernible difference between this test and Test No. 10.

Development Test No. 12 (6/1/94): The hole pattern was changed, but kept the same open hole area (386 in^2). The blades on the orifice assembly were closed to a uniform 1.2 in. Again, there were no discernible changes between this test and last.

Development Test No. 13 (6/694): The hole pattern for this test was reversed end-to-end (same pattern as Test No. 120. The blades on the orifice assembly were also opened to a uniform 1.6 in. This had the effect of increasing the skewness of the jet and making the jet less uniform.

Development Test No. 14 (6/8/94): The hole pattern used in Test No. 12 was replicated, but this time pressure taps were installed on quarter-lengths on the back side of the orifice assembly. The jet remained the same as in Test No. 12, but this time, an idea of the pressure distribution inside the orifice assembly was gained. The downstream tap read 7.68 ft (H_2O), the middle tap read 6.87 ft (H_2O), and the upstream tap read 4.35 ft (H_2O). Further testing will try to refine this pressure distribution so that it is more uniform.

Development Test No. 15 (6/24/94): After researching the topic of pressure manifold design, manifold theory was applied via an iterative technique to redesign the diffuser pattern. The end result was a much more uniform pattern with 398 in^2 of surface area. This straightened the jet more and had a profound impact on the jets uniformity. The downstream pressure tap read 7.45 ft (H_2O), the middle tap read 6.875 ft (H_2O), and the upstream tap read 4.968 ft (H_2O).

Development Test No. 16 (6/30/94): The hole pattern was closed somewhat on the upstream end (363.5 in^2). This increased the skewness of the jet. The downstream pressure tap read 7.205 ft (H_2O), the middle tap read 6.455 ft (H_2O), and the upstream tap read 4.058 ft (H_2O).

Development Test No. 17 (7/16/94): The hole pattern was closed further on the upstream end (325.9 in^2). This further increased the skewness of the jet and made the jet

less uniform. The downstream pressure tap read 7.965 ft (H_2O), the middle tap read 7.175 ft (H_2O), and the upstream tap read 4.508 ft (H_2O).

Development Test No. 18 (7/19/94): The hole pattern was returned to the Test No. 15 condition and a 0.5 in "orifice rib" was placed one-third of the length of the orifice assembly downstream from the upstream end. This had a dramatic effect on the pressure distribution inside the orifice assembly. The downstream pressure tap read 6.115 ft (H_2O), the middle tap read 5.435 ft (H_2O), and the upstream tap read 5.228 ft (H_2O). The uniformity of the jet was noticeably improved, in fact, it now appears completely uniform. However, there is still a slight upstream skew to the jet.

Table B.1 summarizes the orifice assembly development testing series. The table includes the test number, test date, volumetric discharge, initial jet issuance angle, orifice hole area, orifice blade opening width, orifice blade setting, supply pipeline pressure, and head tap readings. Following these quantities, the table has three subjective ratings of jet uniformity, skewness, and finally, a ranking. The ranking quantifies the relative performance of each configuration, which generally improved as testing continued.

Table B.1 Orifice Design Summary

Development Test #	Test Date	Maximum Discharge (ft^3/s)	Jet Issuance Angle (° - vertical)	Orifice Hole Area (in^2)	Orifice Blade Opening (in)	Orifice Blade Setting	Upstream Pressure (psi)	Right Tap Orifice Head (ft H_2O)	Mid Tap Orifice Head (ft H_2O)	Left Tap Orifice Head (ft H_2O)	Jet Uniformity	Jet Skewness From Centerline	Jet Ranking
1	4/14/94	5.082	0	274.8	1.6	Uniform	—	—	—	—	extremely non-uniform	extremely to the right	10
2	5/3/94	6.338	60	374.0	1.6	Uniform	—	—	—	—	extremely non-uniform	right, slightly better than 1	9 - tied
3	5/5/94	7.511	60	391.0	1.6	Uniform	—	—	—	—	unchanged from 2	unchanged from 2	9 - tied
4	5/6/94	7.003	60	396.0	1.6	Uniform	—	—	—	—	non-uniform, better than Demo	right, slightly better than Demo	5
Demo	5/16/94	—	60	401.0	1.5	Uniform	2.0	—	—	—	unchanged from 4	right, worse than 4	6
5	5/17/94	6.425	30	391.0	1.5	Uniform	2.0	—	—	—	non-uniform, worse than 8	right, worse than 8	8 - tied
6	5/18/94	6.386	30	391.0	1.4	Uniform	3.0	—	—	—	unchanged from 5	unchanged from 5	8 - tied
7	5/19/94	6.206	30	391.0	1.3	Uniform	3.0	—	—	—	unchanged from 5	unchanged from 5	8 - tied
8	5/23/94	6.403	30	400.0	1.3	Uniform	3.2	—	—	—	non-uniform, better than 7	right, worse than 7	7 - tied
9	5/24/94	6.167	30	400.0	1.4	Uniform	3.1	—	—	—	unchanged from 8	unchanged from 8	7 - tied
10	5/25/94	6.284	30	400.0	left = 1.2 right = 1.4	Trapezoidal	3.3	—	—	—	unchanged from 8	unchanged from 8	7 - tied
11	5/27/94	6.347	30	386.0	1.4	Uniform	3.0	—	—	—	unchanged from 8	unchanged from 8	7 - tied
12	6/1/94	6.492	30	386.0	1.2	Uniform	4.1	—	—	—	unchanged from 8	unchanged from 8	7 - tied
13	6/8/94	6.341	30	386.0	1.6	Uniform	3.4	—	—	—	extreme, worse than 1	extreme right, worse than 1	11
14	6/16/94	6.441	30	386.0	1.6	Uniform	2.9	7.680	6.870	4.530	unchanged from 12	unchanged from 12	7 - tied
15	6/24/94	6.479	25	398.0	1.6	Uniform	2.5	7.450	6.875	4.968	slight, better than 16	slightly right, better than 16	2
16	6/30/94	6.420	25	363.5	1.6	Uniform	2.6	7.205	6.455	4.058	slight, worse than 15	right, worse than 15	3
17	7/6/94	6.420	25	325.9	1.6	Uniform	2.8	7.965	7.175	4.508	slight, worse than 16	right, worse than 16	4
18	7/19/94	6.420	25	398.0	1.6	Uniform	2.1	6.115	5.435	5.228	semi-uniform, better than 15	barely right, better than 15	1

A total of nineteen different configurations were used in the development of the dam foundation overtopping model facility. Figures B.1 through B.19 illustrate the hole patterns used in the delivery pipeline for each of the tests.

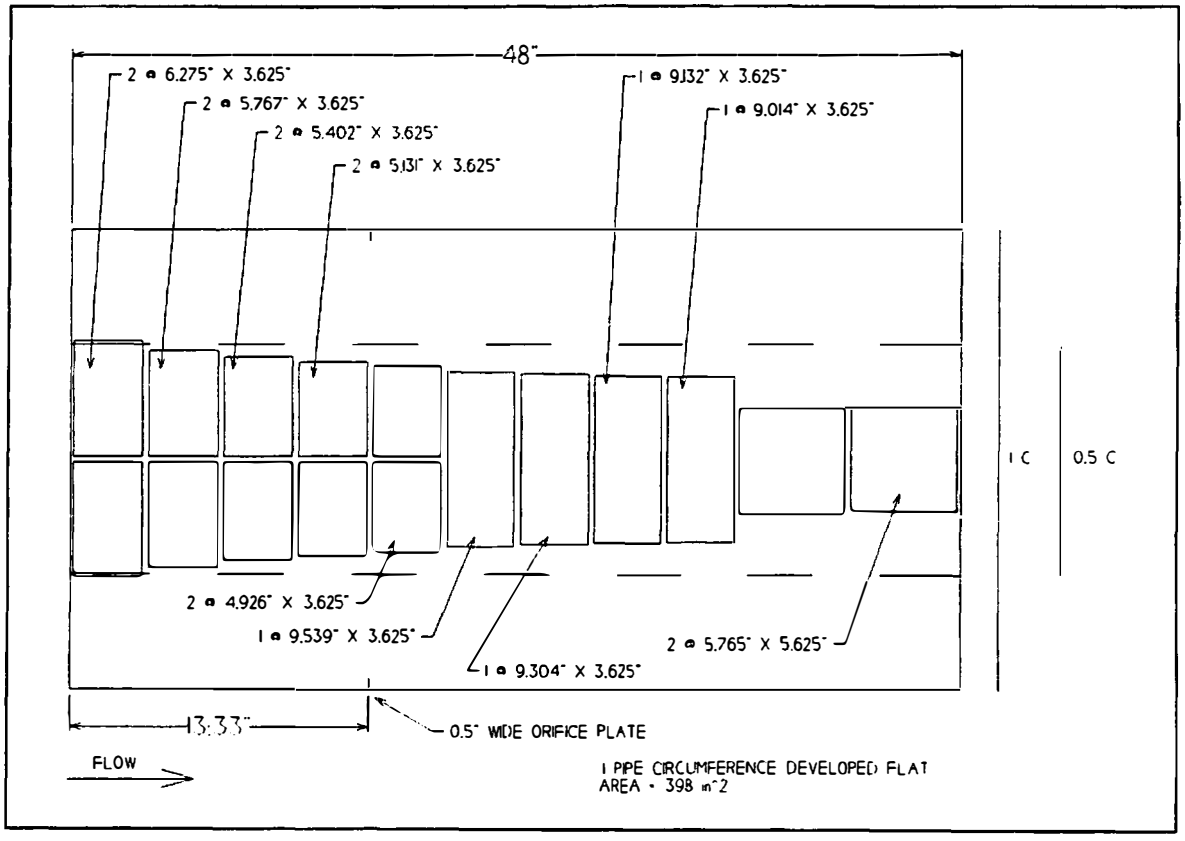

Figure B.1 Orifice hole pattern: Development Test 1

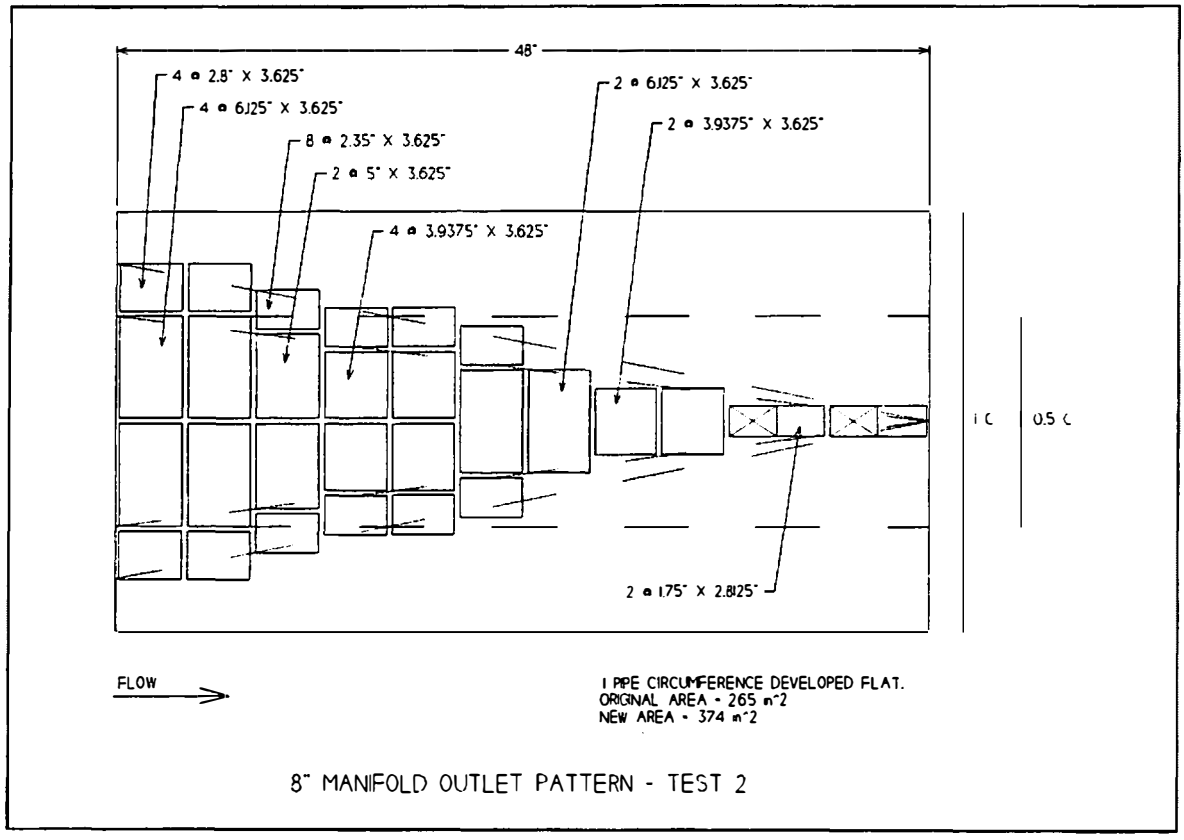

Figure B.2 Orifice hole pattern: Development Test 2

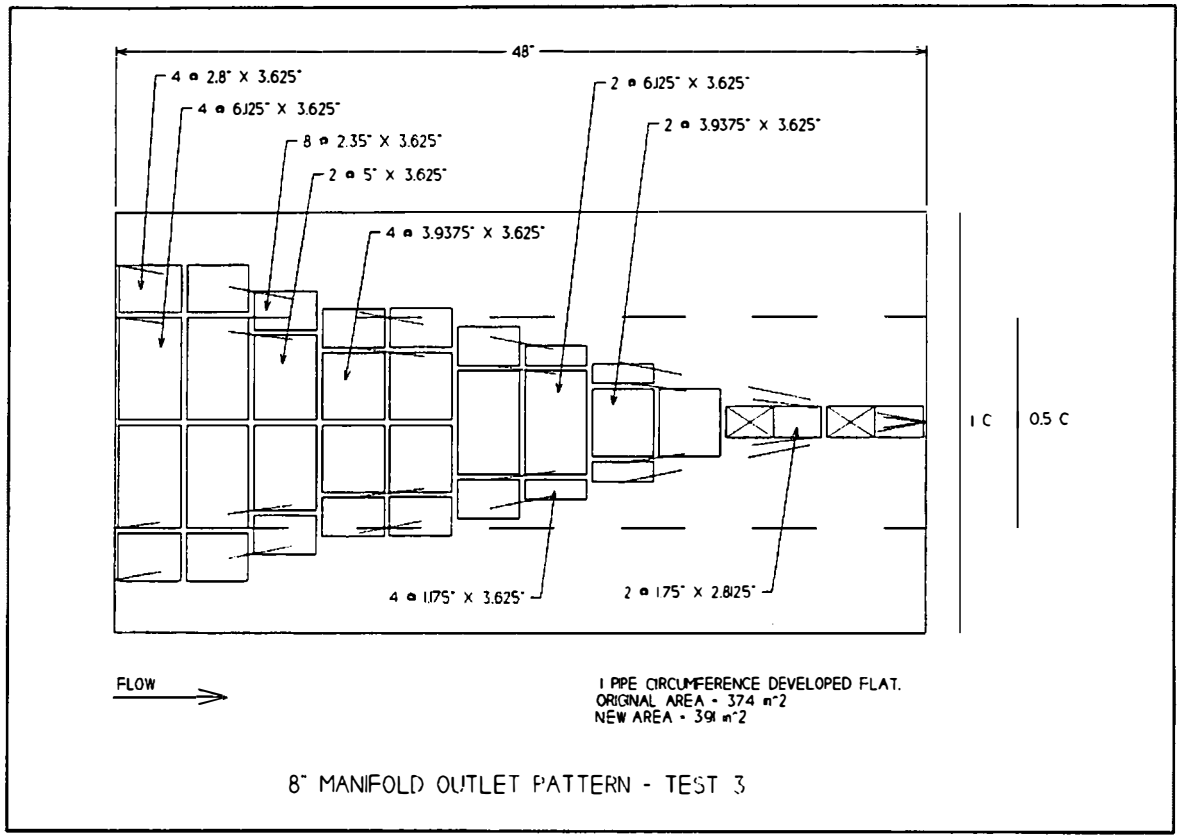

Figure B.3 Orifice hole pattern: Development Test 3

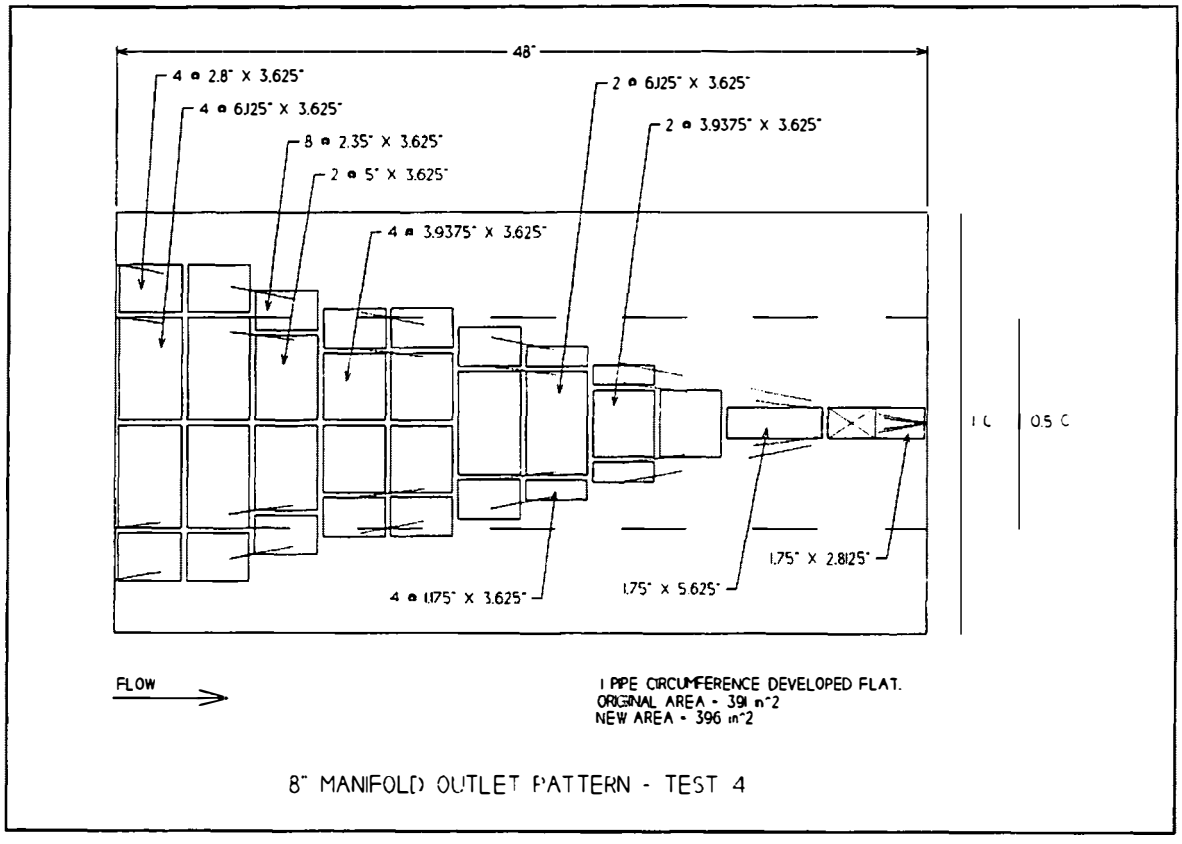

Figure B.4 Orifice hole pattern: Development Test 4

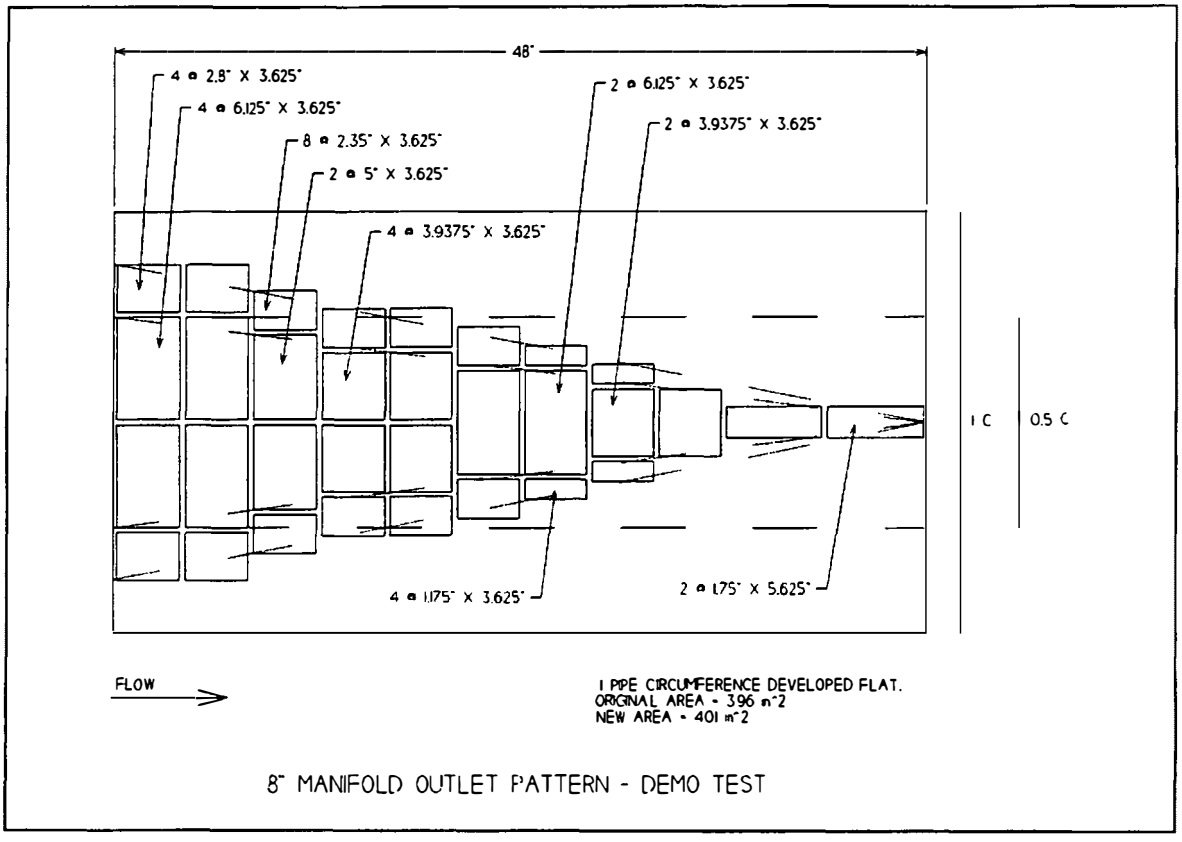

Figure B.5 Orifice hole pattern: Demo Test

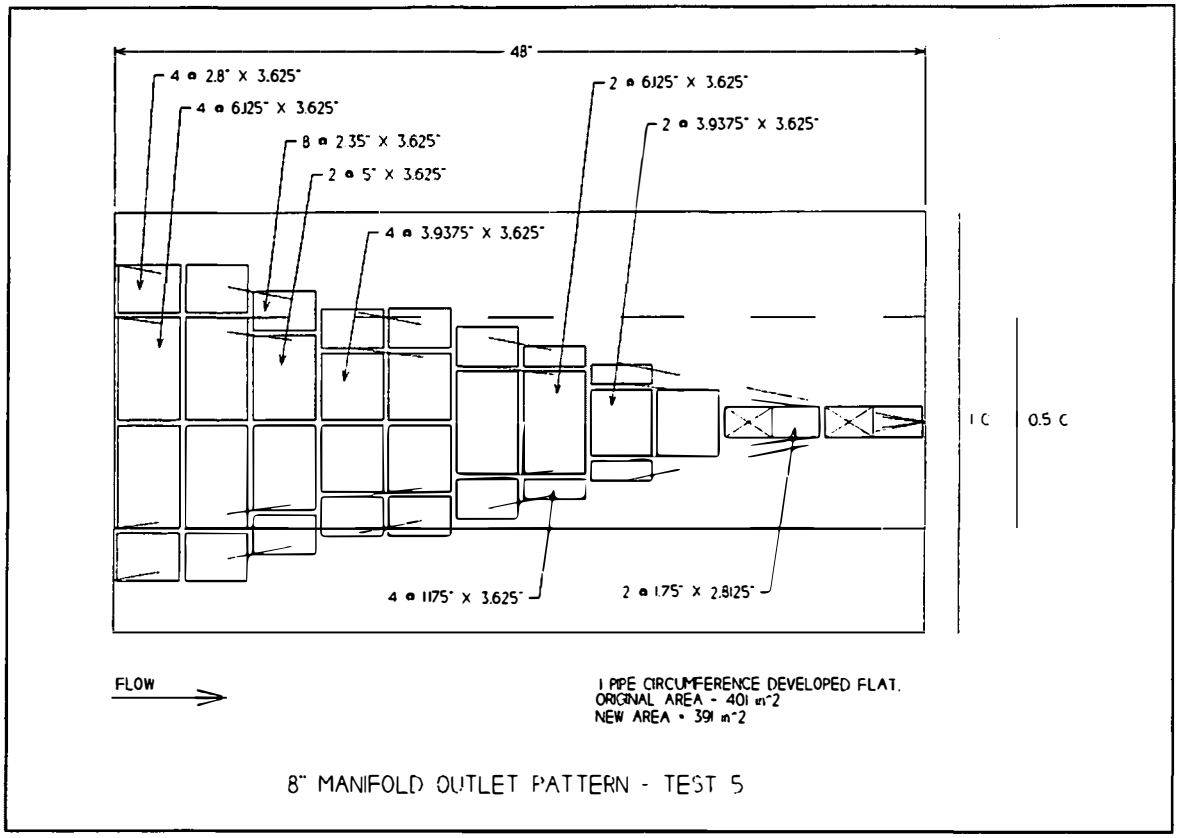

Figure B.6 Orifice hole pattern: Development Test 5

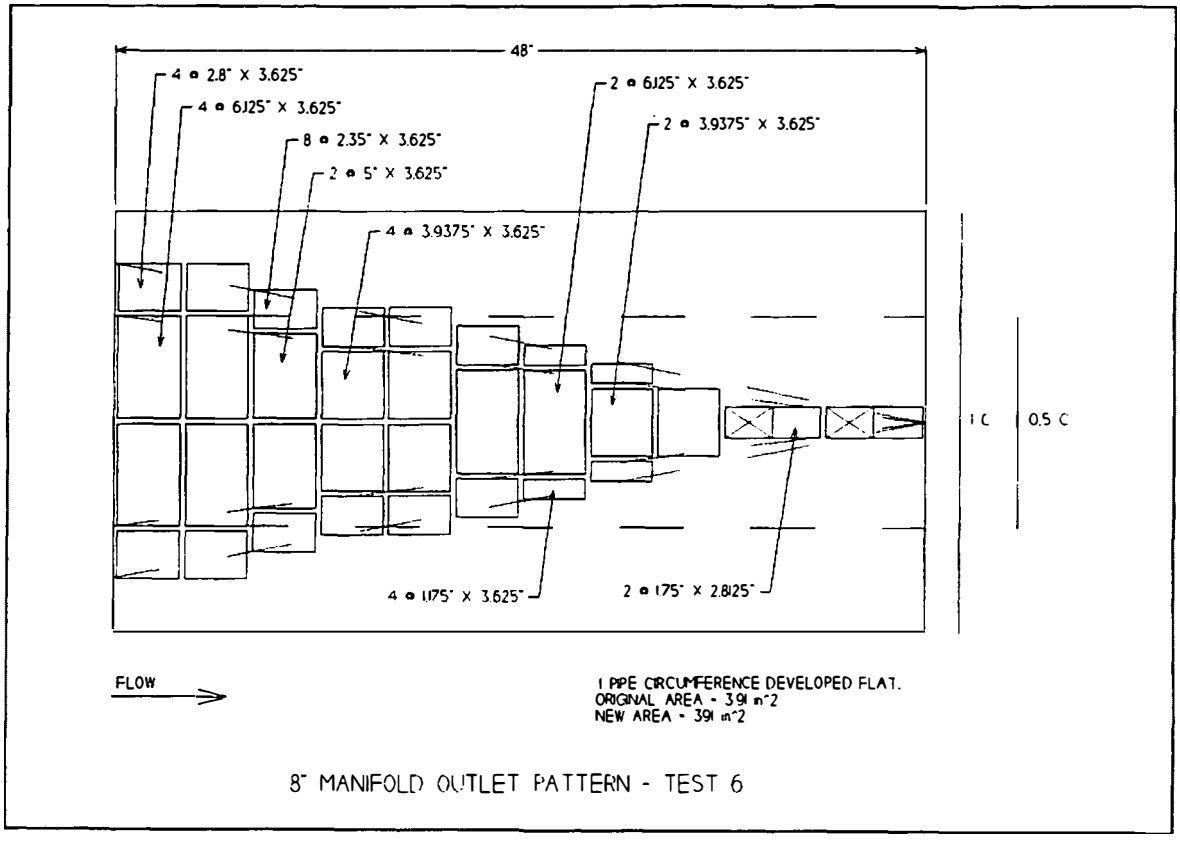

Figure B.7 Orifice hole pattern: Development Test 6

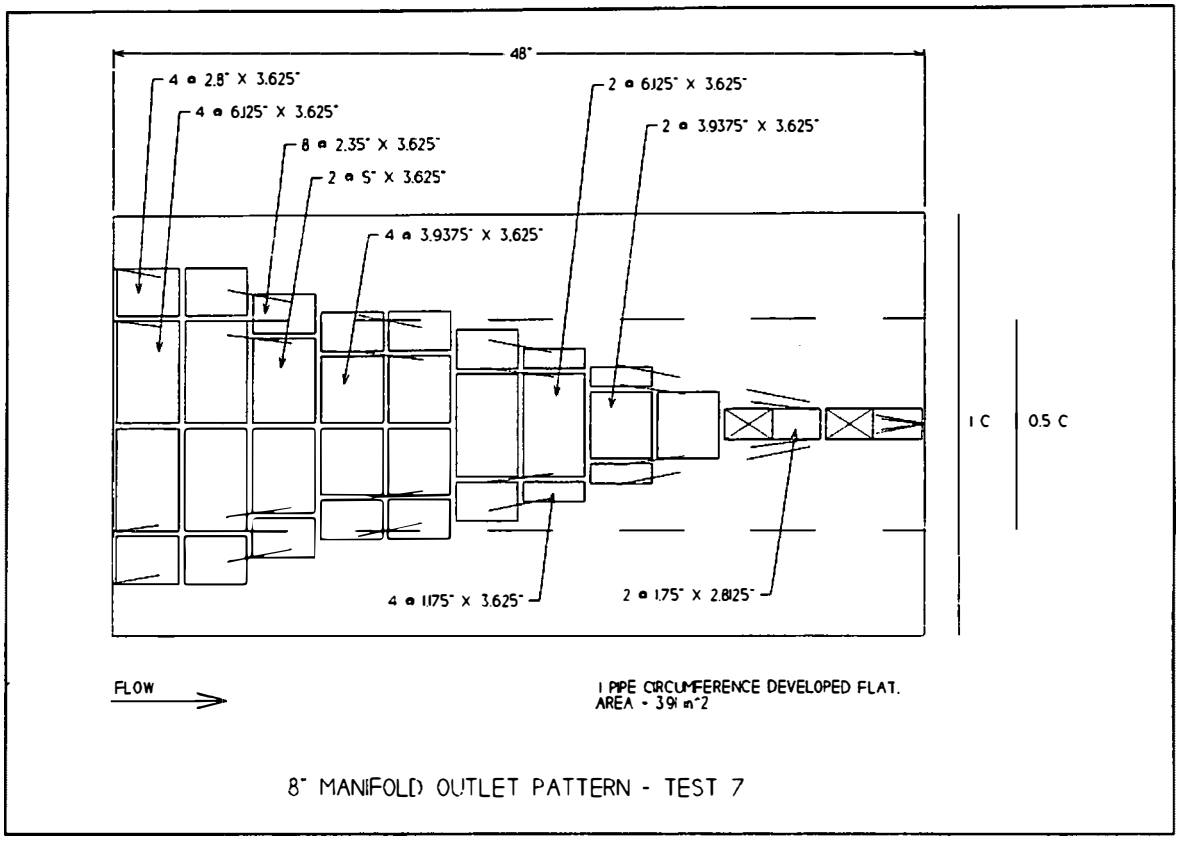

Figure B.8 Orifice hole pattern: Development Test 7

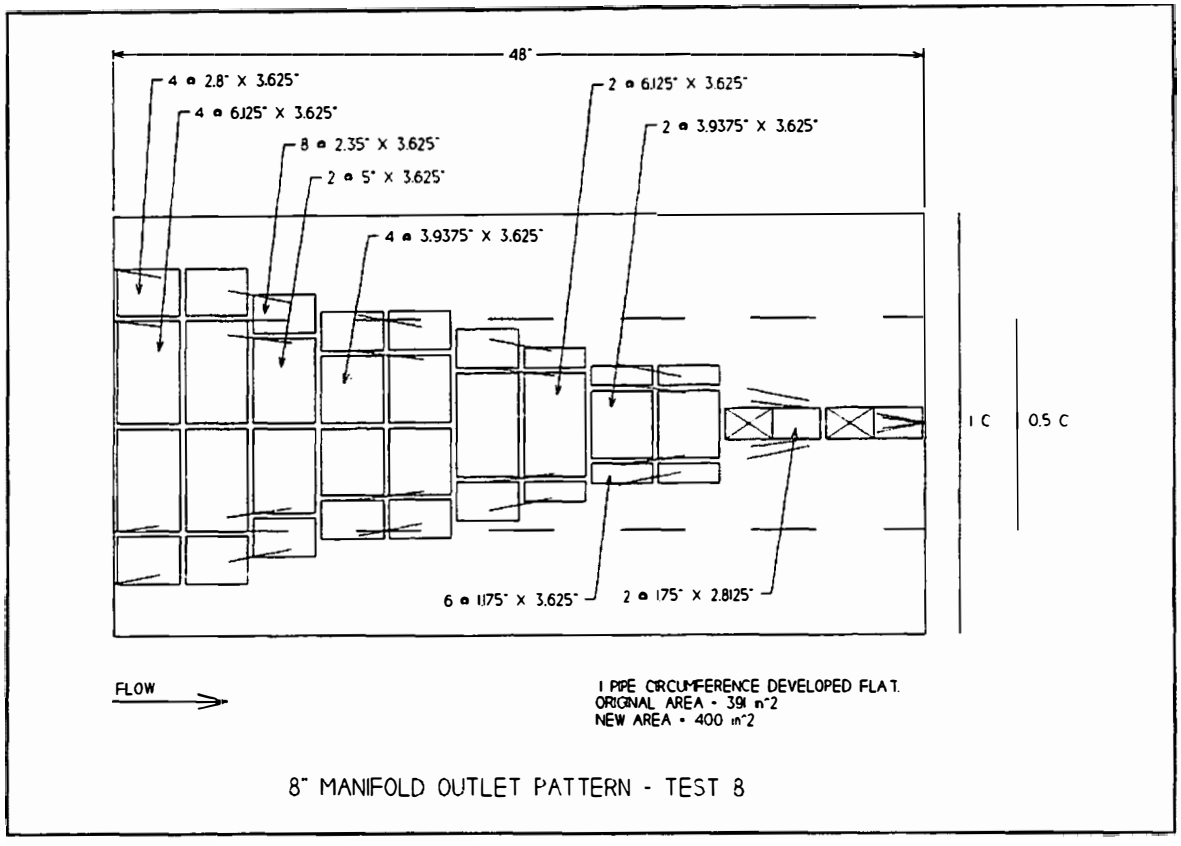

Figure B.9 Orifice hole pattern: Development Test 8

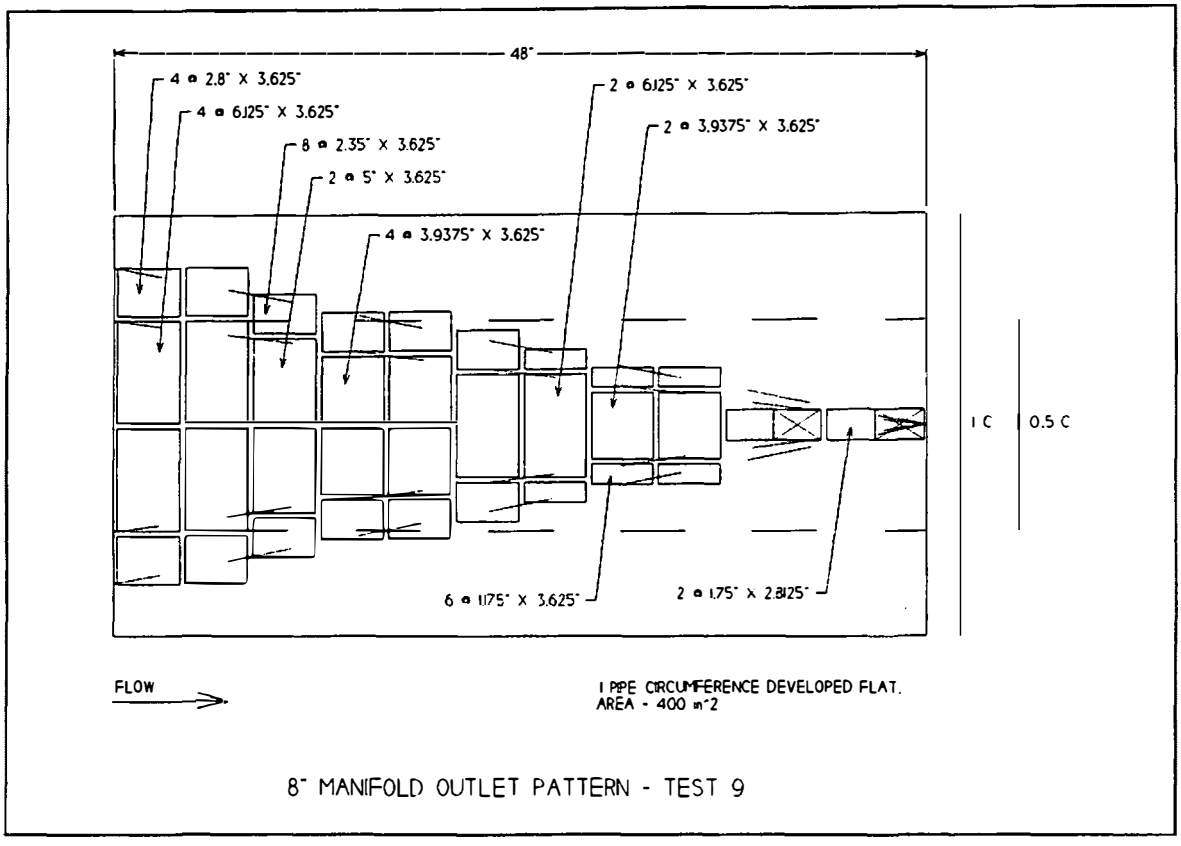

Figure B.10 Orifice hole pattern: Development Test 9

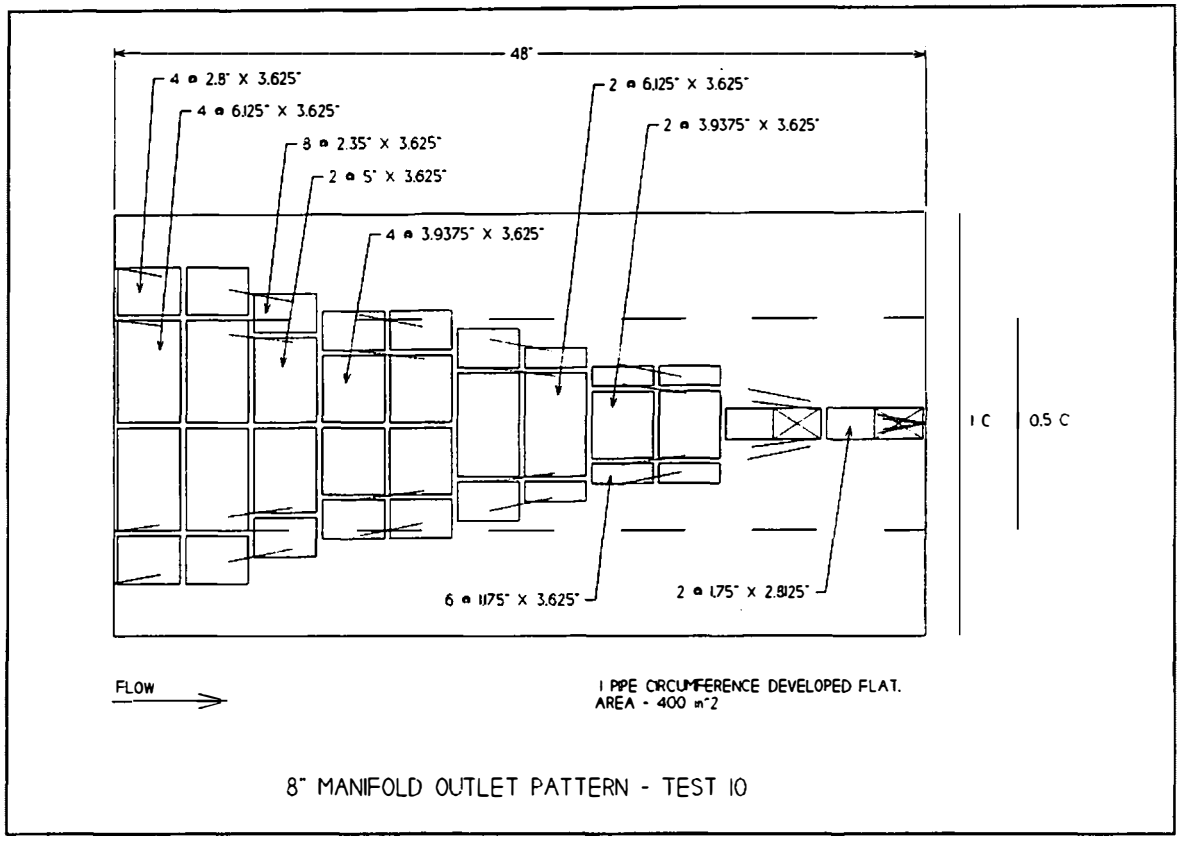

Figure B.11 Orifice hole pattern: Development Test 10

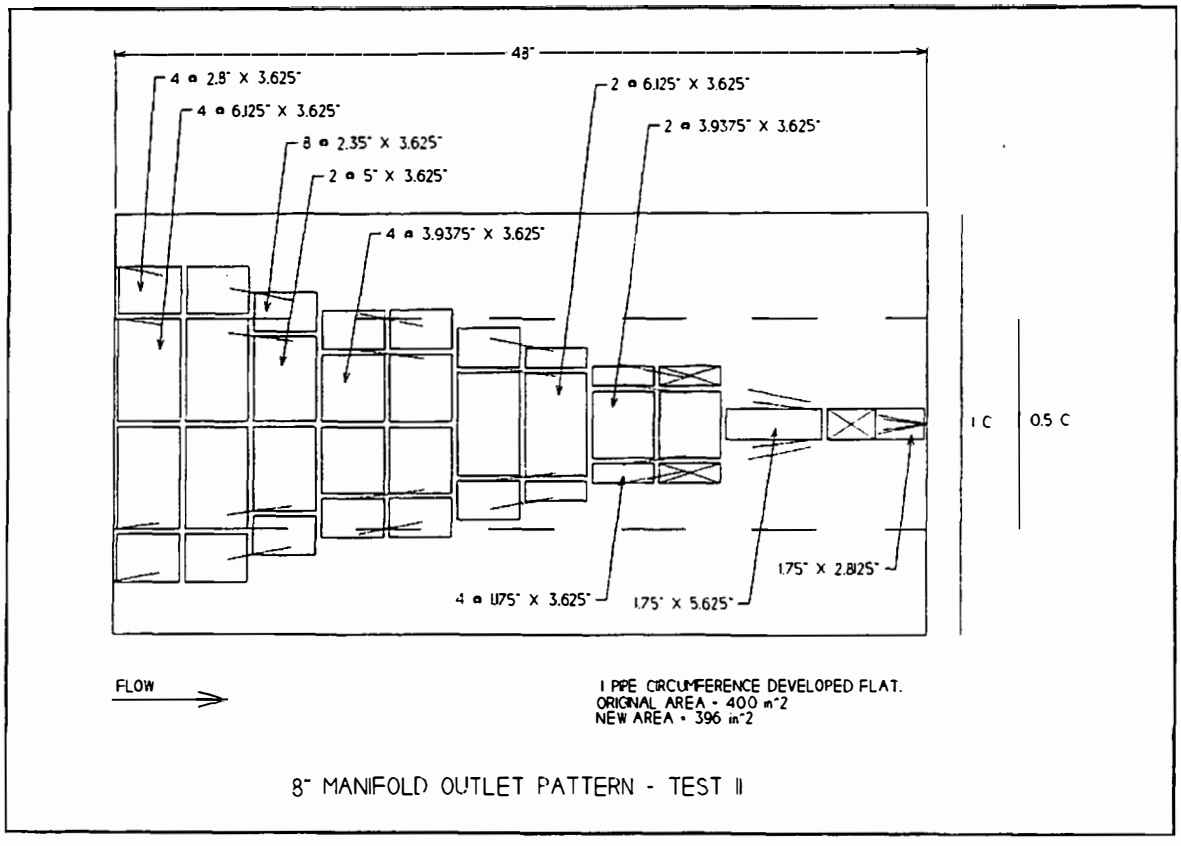

Figure B.12 Orifice hole pattern: Development Test 11

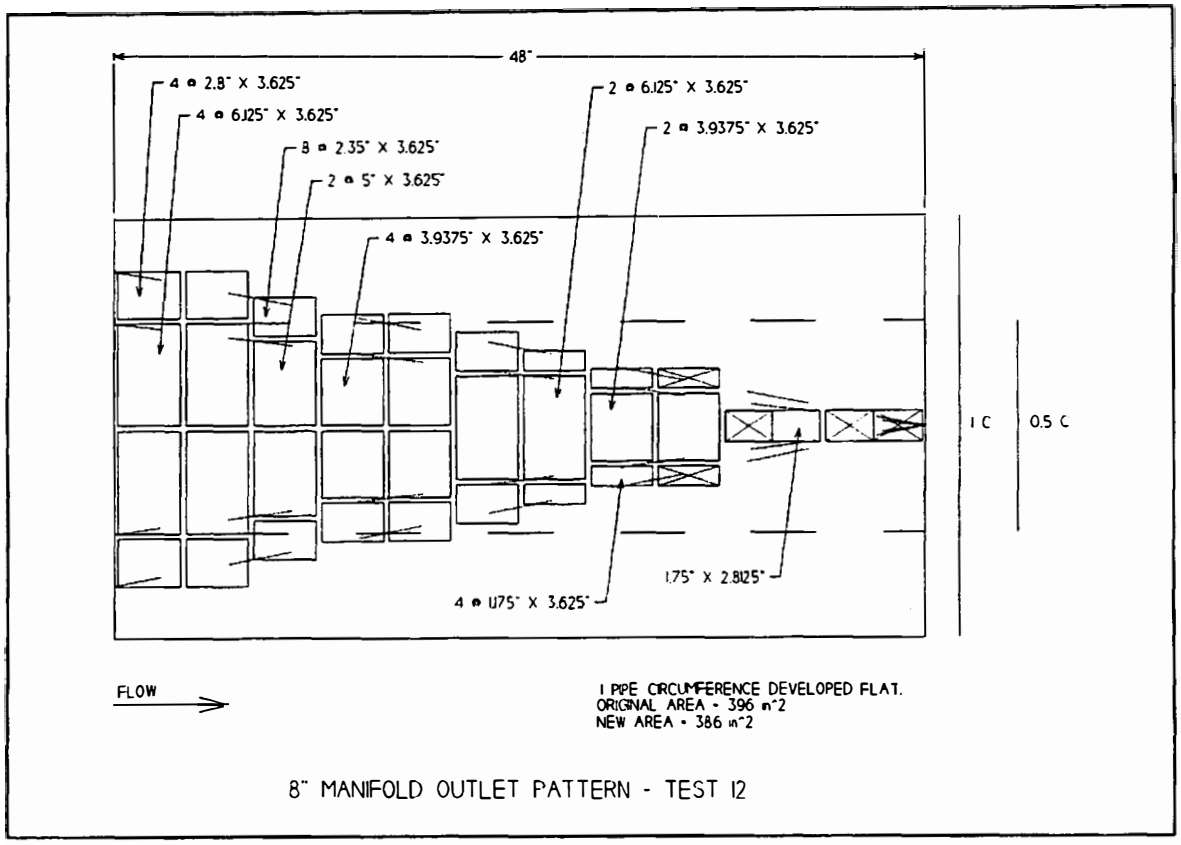

Figure B.13 Orifice hole pattern: Development Test 12

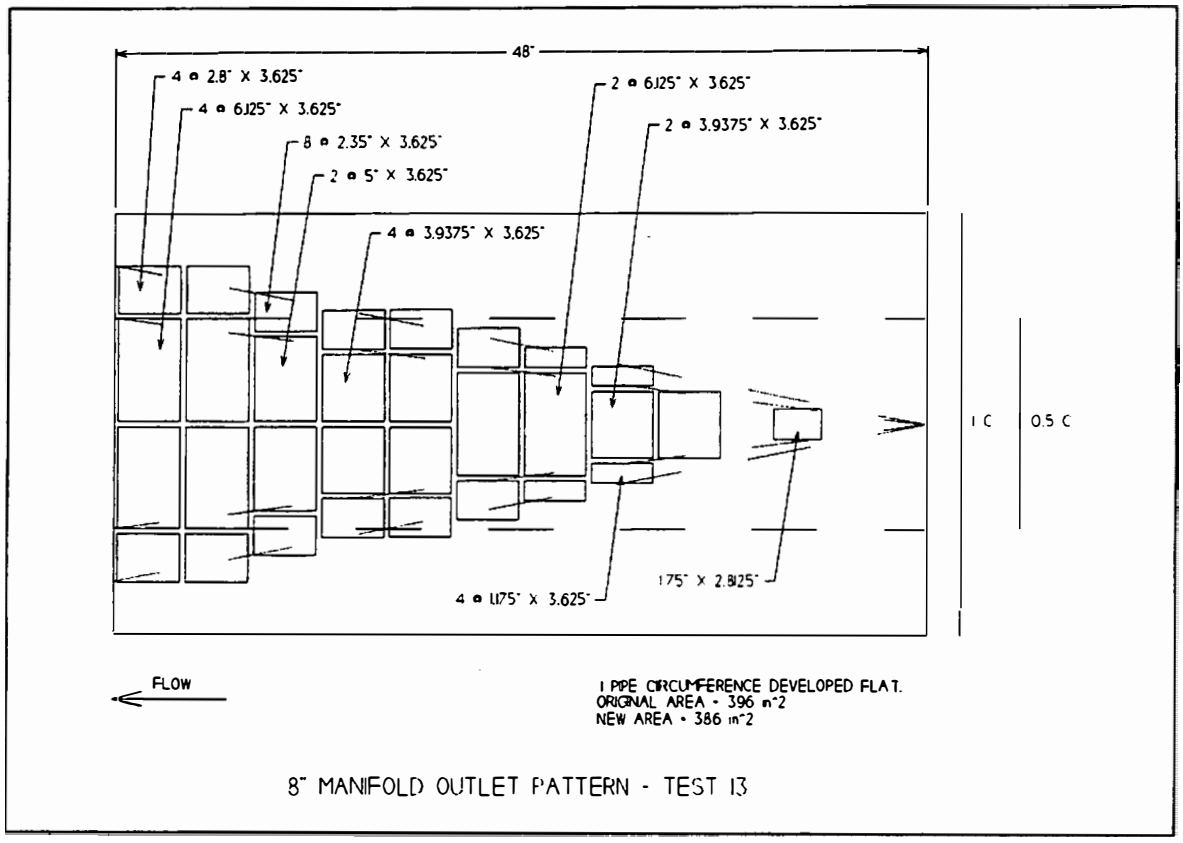

Figure B.14 Orifice hole pattern: Development Test 13

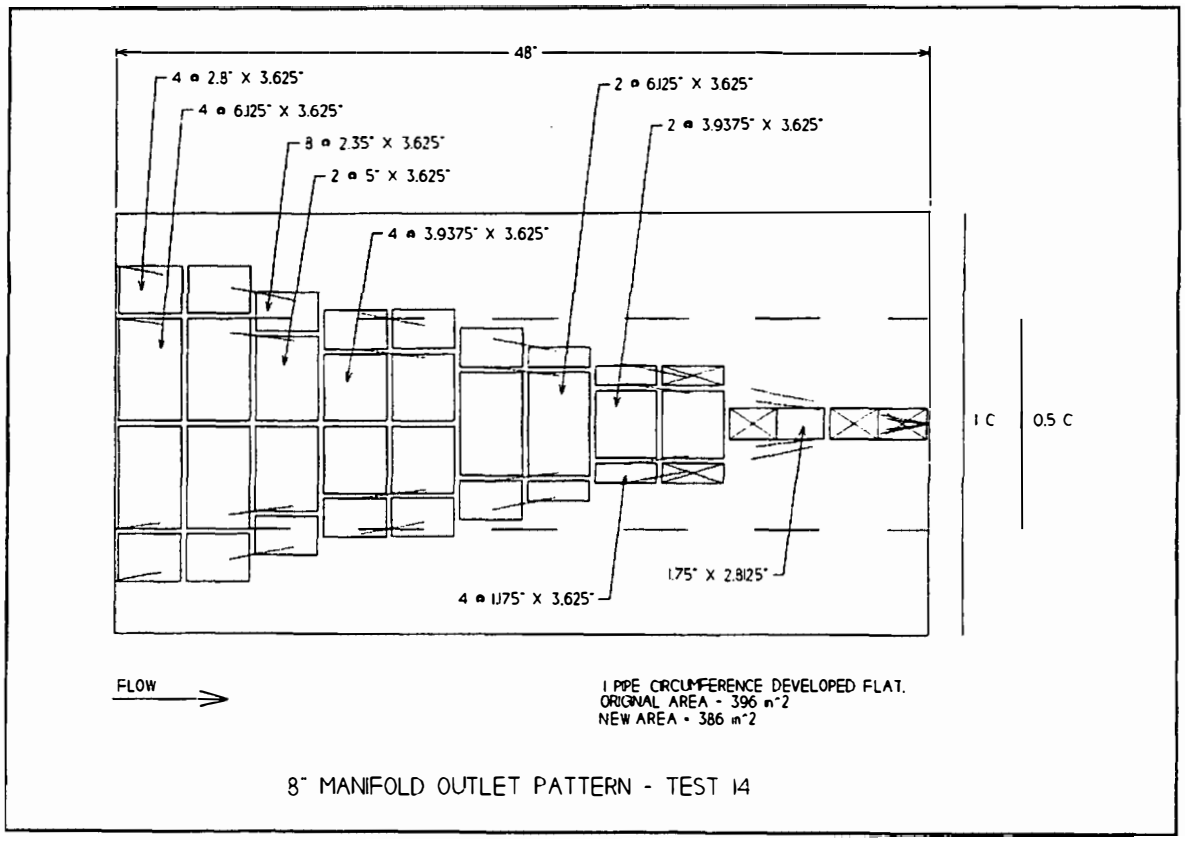

Figure B.15 Orifice hole pattern: Development Test 14

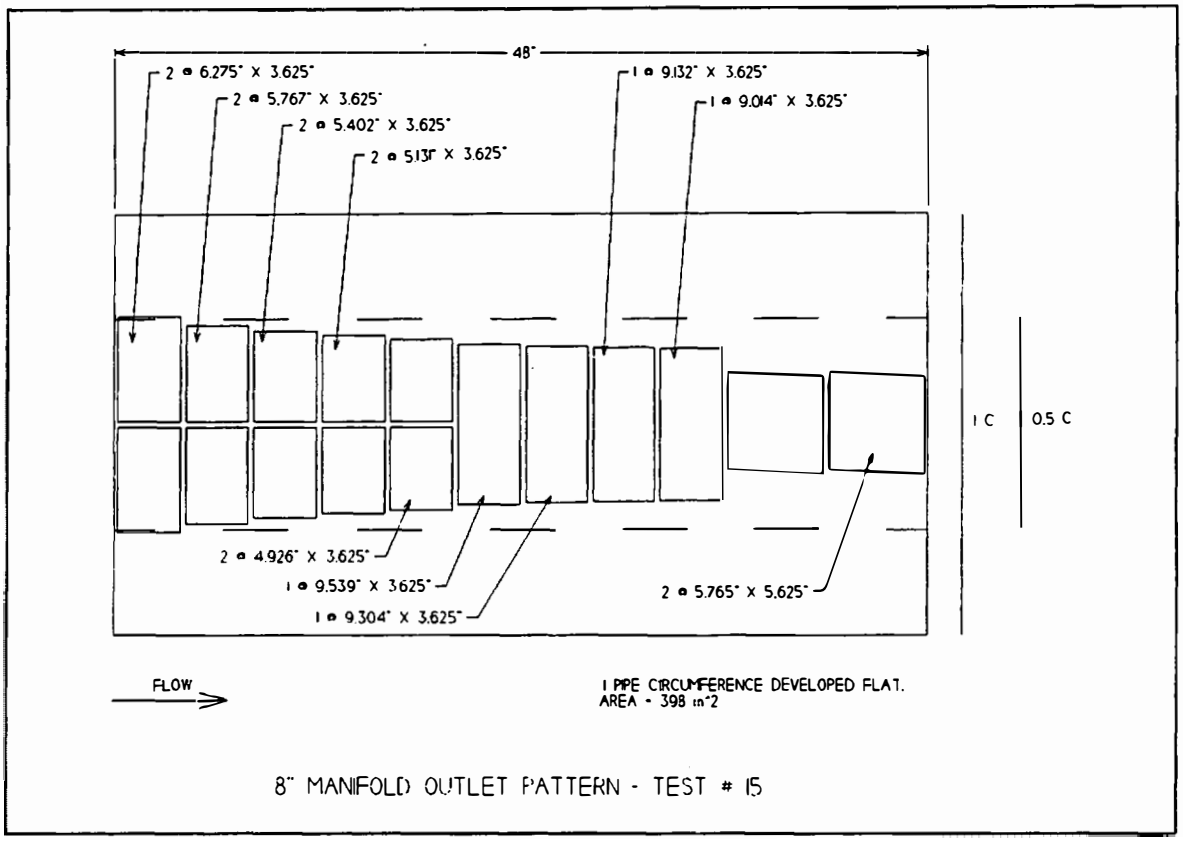

Figure B.16 Orifice hole pattern: Development Test 15

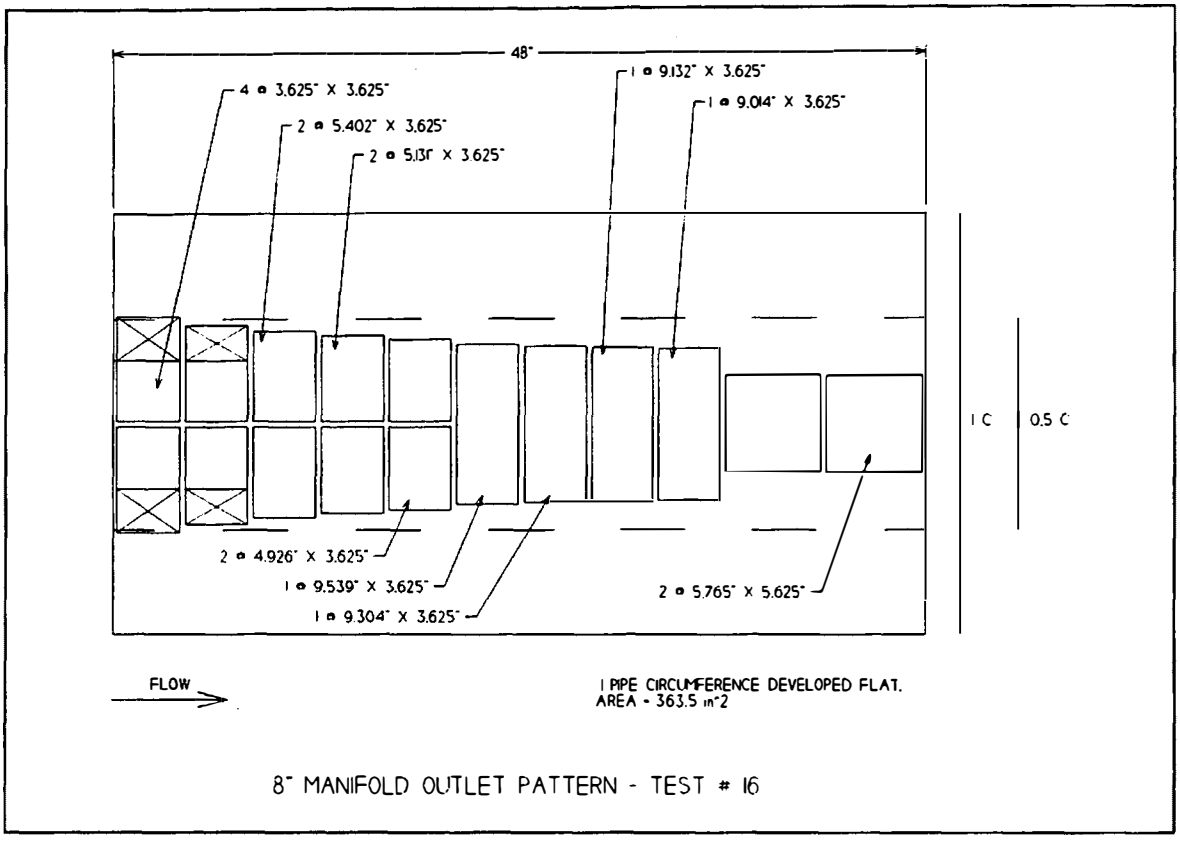

Figure B.17 Orifice hole pattern: Development Test 16

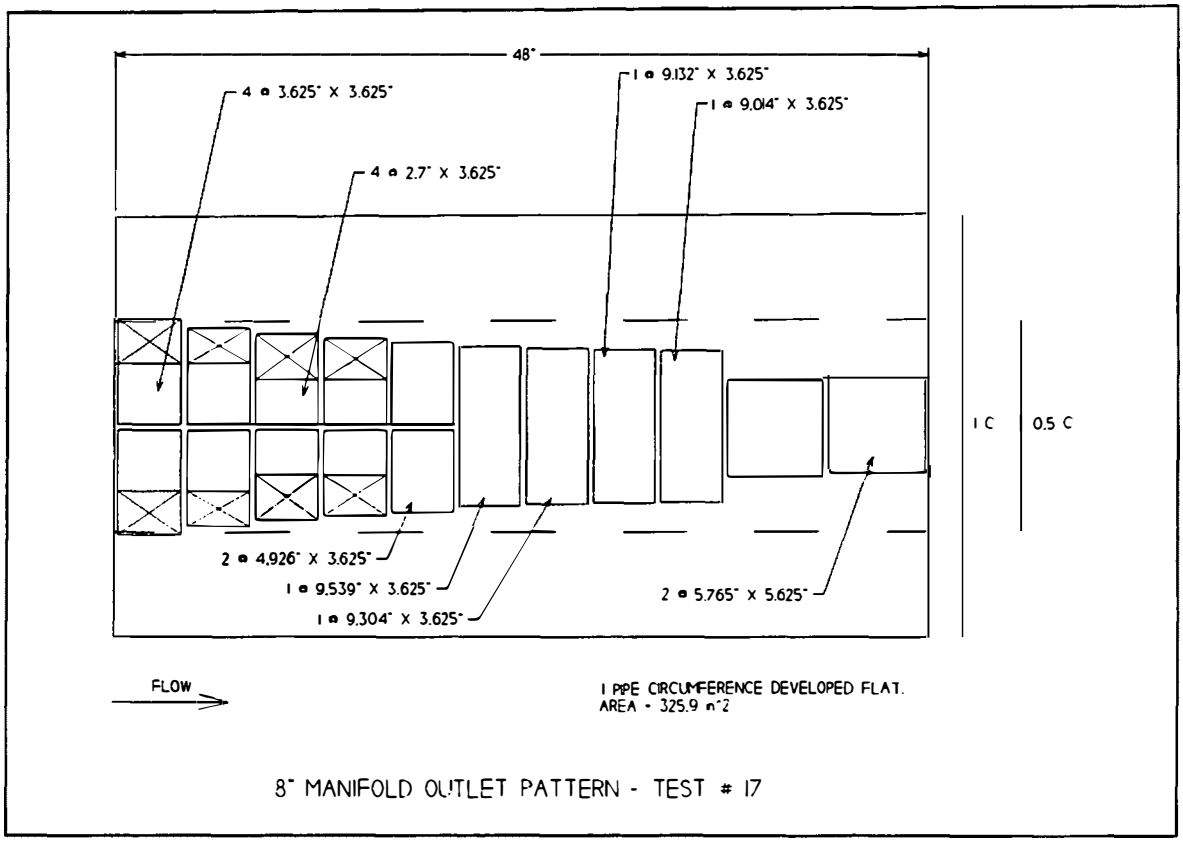

Figure B.18 Orifice hole pattern: Development Test 17

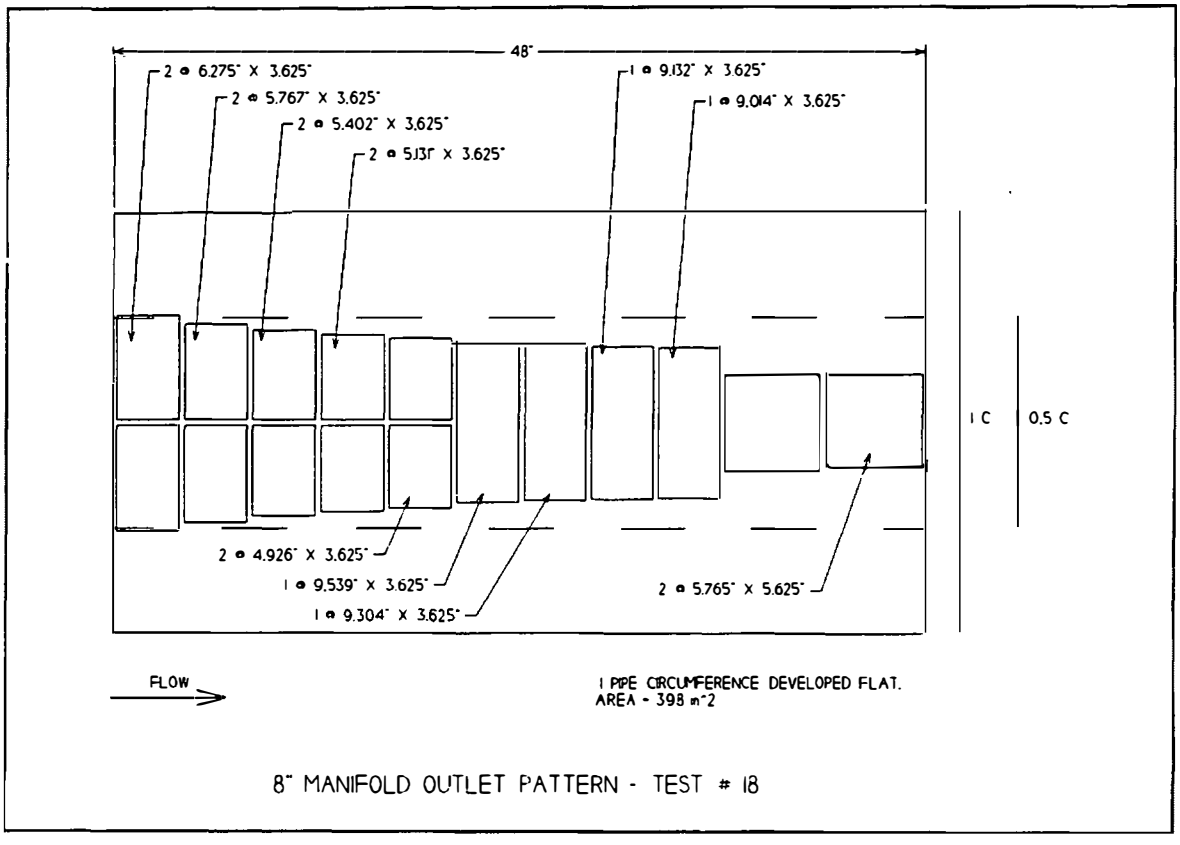

Figure B.19 Orifice hole pattern: Development Test 18

APPENDIX C

BACK-FLUSHING PITOT-STATIC SYSTEM CALIBRATION

During February and March, 1995, the instruments comprising the back-flushing pitot-static tube system were calibrated. These instruments were: a Stathium PM399 pressure transducer, a back-flushing pitot-static probe, and an air concentration meter. The last two instruments were developed for use in the dam overtopping model by researchers at the United States Bureau of Reclamation Hydraulics Labs, located in Denver, Colorado. The following paragraphs explain how each of the three instruments were calibrated.

C.1 Calibration of Stathium PM399 Pressure Transducer

The pressure transducer enables the measurement of pressure differentials between the static and dynamic port lines of the back-flushing pitot-static probe. The pressure transducer provides a constant output voltage that is linearly related to the instantaneous pressure differential. Calibration of the pressure transducer was accomplished by attaching one port of the transducer to a vertical water standpipe and leaving the other port open to the atmosphere. Output voltages were then sampled for a number of different water column heights. A linear regression analysis was performed on

this data to develop a water pressure (head) vs. voltage calibration equation. Table C.1 presents the calibration data used in formulating the calibration equation.

Table C.1 Transducer Calibration Data

Sample Number	Transducer Output Voltage (volts)	Water Pressure (ft H_2O)
1	0.2533	0.07
2	0.4730	1.14
3	0.5778	1.65
4	0.6661	2.08
5	0.7749	2.61
6	0.8776	3.11
7	0.9741	3.58
8	1.0789	4.09
9	1.1795	4.58
10	1.2884	5.11
11	1.3828	5.57

A linear regression analysis was performed on the data from Table C.1 in order to determine the pressure transducer calibration equation. The calibration equation, along with the calibration data and regression line are presented in Figure C.1.

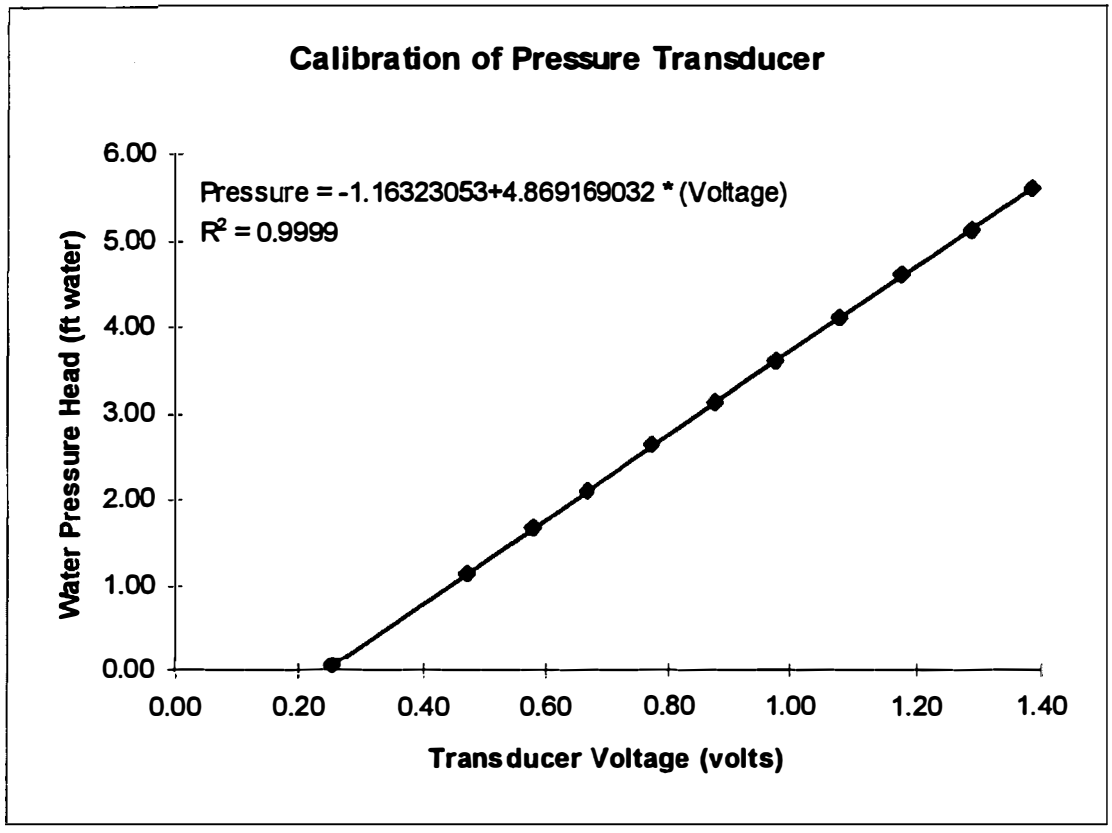

Figure C.1 Transducer calibration with regression line

C.2 Calibration Of Back-Flushing Pitot-Static Probe

The back-flushing pitot-static probe is placed in the developed jet to obtain point readings of the jet's stagnation pressure. As discussed in Section 4.4, these readings can be converted into velocity readings provided the probe tip is calibrated for the different two-phase (air-water) densities. Stagnation pressures were measured at a wide range of air-water concentrations. This data was used to generate a family of pressure differential vs. impingement velocity calibration curves can be generated, one for each air concentration.

The back-flushing pitot probe calibration apparatus, located at the United States Bureau of Reclamation Hydraulics Labs in Denver, Colorado, consists of an inverted "U" shaped water pipe system, two rotometers, and a pressure regulator. Water and air volumes entering the system are measured using the rotometers, and the air pressure is set with the pressure regulator. Water is supplied to the pipe system on the up leg of the system. Air is supplied to the system on the down leg. For the back-flushing pitot-probe calibration, a 10 cm long tip of pipe that is smaller in diameter than the main "U" pipe is attached to the end of the piping system to provide backpressure and obtain a relatively uniform jet of two-phase air-water mixture leaving the pipe.

The back-flushing pitot-static probe was placed within one tip diameter of the end and centered within the two phase jet. Water velocity impinging on the total pressure port of the probe was assumed to be equal to the water velocity internal to the calibration apparatus tip. The water velocity was determined as the water discharge divided by the area of the tip minus the area of entrained air. Data taken during the calibration procedure included the following:

1. air and water flow rates for each data point, measured using their respective rotometers,
2. the transducer output voltage for each data point, measured with a voltmeter,
3. the barometric pressure and temperature at the time of testing, and
4. the inside diameter of the smaller diameter pipe through which the air-water mixture jet exits.

After collecting the calibration data at the United States Bureau of Reclamation Labs, a data analysis was performed to determine the aforementioned pressure differential vs. impingement velocity curves. The data analysis consisted of the following steps:

1. Use the measured barometric pressure, the air temperature, and the water rotometer calibration table to determine a temperature correction factor for not using the water rotometer at standard (sea-level) pressure.

2. Add the temperature correction factor to the measured temperature to obtain the pressure-corrected temperature.

3. Calculate the correction multiplier for the air rotometer by using the ideal gas law

$$\frac{P_s V_s}{T_s} = \frac{P_x V_x}{T_x} \quad \therefore \quad \left(\frac{V_x}{V_s}\right) = \left(\frac{P_s}{P_x}\right)\left(\frac{T_x}{T_s}\right) \tag{C.1}$$

where

P_s = metering pressure from calibration table (M/LT),

P_x = measured barometric pressure (M/LT),

T_s = metering temperature from calibration table (ϕ),

T_x = pressure-corrected temperature (ϕ),

V_s = volume at calibration temperature and pressure (L^3), and

V_x = volume at testing conditions (L^3).

4. Calculate the area of the outlet pipe

$$A = \pi \frac{d^2}{4} \tag{C.2}$$

where

A = outlet area of pipe (L^2), and

d = inside diameter of pipe outlet (L).

5. Calculate the uncorrected water velocities at each sampling point

$$V_{H20\_U} = \frac{Q_{H2O}}{A} \tag{C.3}$$

where

V_{H2O_U} = uncorrected water velocity (L/T), and

Q_{H2O} = volumetric flow rate of pure water (L^3/T).

6. Calculate the pressure and temperature corrected air flow rates at each sampling point.

$$Q_{air\_C} = \left(\frac{V_x}{V_s}\right) Q_{air\_U} \tag{C.4}$$

where

Q_{air_C} = corrected air volumetric flow rate (L^3/T), and

Q_{air_U} = uncorrected air volumetric flow rate (L^3/T).

7. Calculate the total two-phase air-water flow rate for each sampling point

$$Q_{2P} = Q_{air\_C} + Q_{H2O} \tag{C.5}$$

where

Q_{2P} = volumetric two-phase air-water flow rate (L^3/T).

8. Calculate the concentration of water in the two-phase flow for each sampling point.

$$\mathrm{H_2O\ concentration} = \frac{Q_{H2O}}{Q_{2P}} \tag{C.6}$$

9. Calculate the corrected water velocities for each sampling point

$$V_{H2O\_C} = \frac{V_{H20\_U}}{\mathrm{H_2O\ concentration}} \tag{C.7}$$

where

V_{H2O_C} = corrected water velocity (L/T).

10. Use the transducer calibration equation to convert the output voltages into pressure differential readings.

11. Correct the pressure differential readings by subtracting the pressure reading for a combined air-water flow rate of zero.

12. Calculate the air concentrations at each point.

$$\text{Air concentration} = 1 - \mathrm{H_2O\ concentration} \tag{C.8}$$

13. Group the corrected pressure differential readings and the corrected water velocity readings by air concentration.

14. Use the grouped readings from the previous step to determine power function equations for each air concentration group with regression analysis. In general, these equations will take the form:

$$V = c_1 P^{c_2} \tag{C.9}$$

where

V = velocity reading (L/T),

P = pressure differential reading (M/LT),

c_1 = a dimensionless regression coefficient, and

c_2 = another dimensionless regression coefficient.

The calibration curves that were calculated from the regression analysis performed on the collected calibration data are presented in Figure C.2.

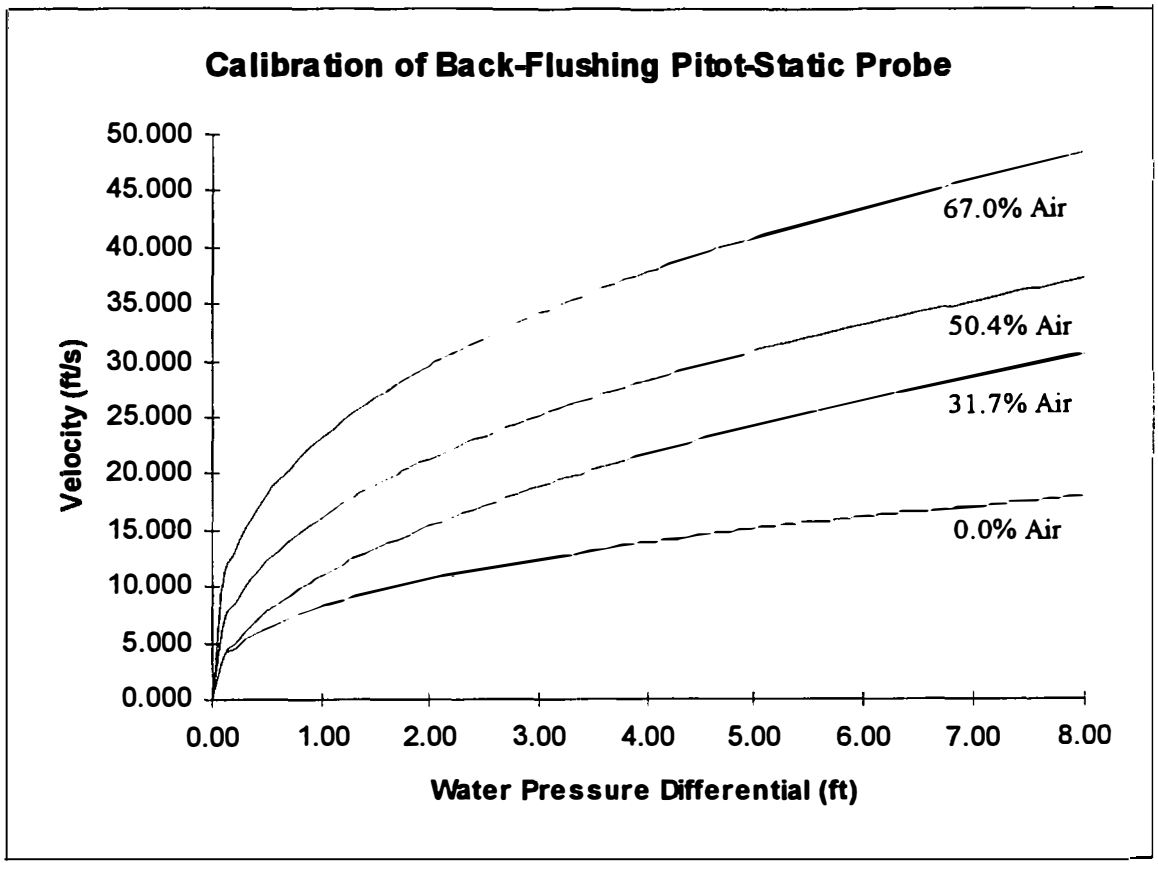

Figure C.2 Calibration curves

The equations describing each of the calibration curves are given in Table C.2

Table C.2 Regression Equations

% Air in 2-phase flow:	regression coefficient: c_1	regression coefficient: c_2	coefficient of determination: R^2
0.00	8.22146	0.372636	0.9707
31.7	10.8828	0.494712	0.9760
50.4	16.1688	0.398368	0.9439
67.0	23.1457	0.351839	0.9362

C.3 Calibration Of Air Concentration Meter

The air concentration meter is used in conjunction with the back-flushing pitot-static probe to determine which calibration curve from Figure C.2 is used to compute velocity from measured water pressure differential. In the case the measured air concentration lies between calibration curves, a linear interpolation is performed between the two curves to determine the calculated velocity.

Calibration of the air concentration meter is performed with the same apparatus used for calibrating the back-flushing pitot-static probe, except in this case, air concentrations are measured instead of pressure differentials. The calibration procedure used is identical to that used for the back-flushing pitot-static probe up through step 8. The following steps are then performed:

9. Calculate the air concentrations at each point using Equation C.8

10. Use the measured air concentrations and the calculated air concentrations from the previous step to determine a calibration equation with regression analysis. The polynomial regression equation will take the form:

$$A = k_1 + k_2(a) + k_3(a)^2 + k_4(a)^3 \qquad \text{(C.10)}$$

where

A = corrected air concentration (%),

a = measured air concentration (%), and

$k_1 - k_4$ = dimensionless regression coefficients.

The calibration data along with the calculated regression line are presented in Figure C.3.

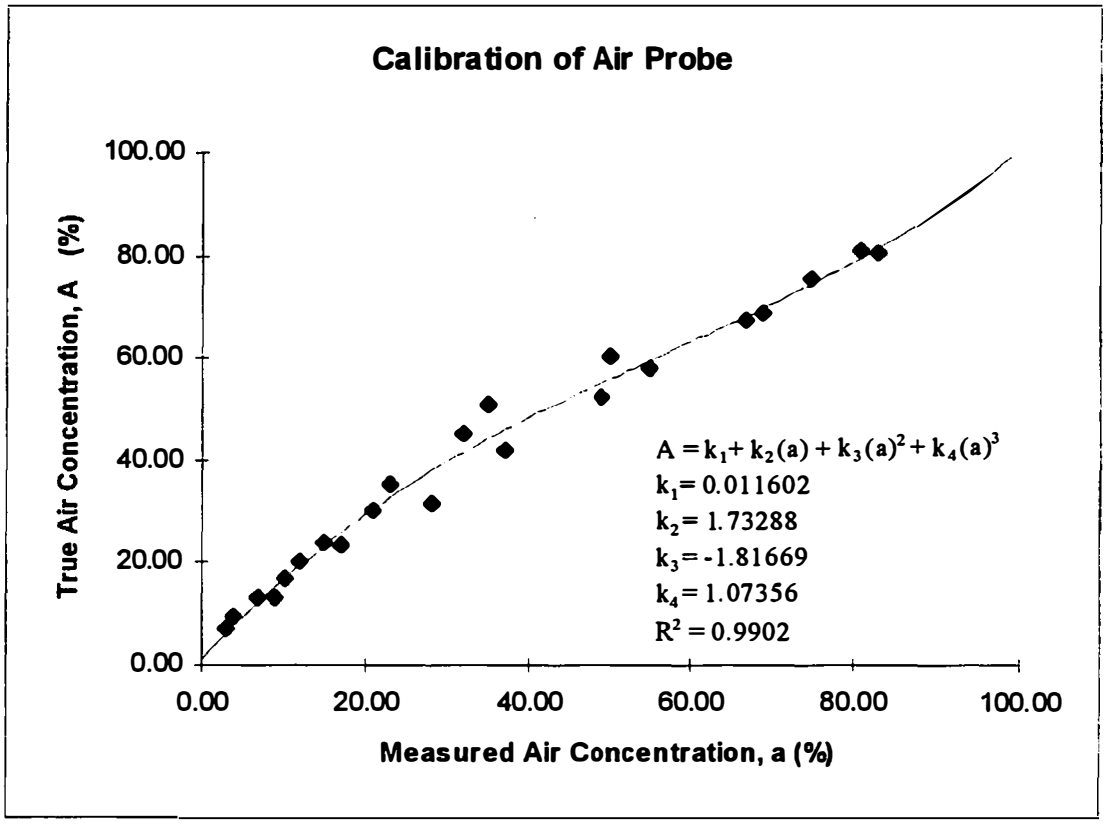

Figure C.3 Air concentration probe calibration data

APPENDIX D

JET ISSUANCE UNIFORMITY ANALYSIS

A graphical analysis was performed on pitot tube measurements taken at the orifice assembly to determine if the developed jet was sufficiently uniform at issuance to ensure the suitability of a numerical average in quantifying the initial velocity of the jet. Scatter plots were formed with the dimensionless horizontal position relative to the orifice opening on the abscissa and measured velocity in ($^{ft}/_{s}$) on the ordinate. Examination of the scatter plots (illustrated in Figures D.1 - D.27) reveals that the discreet velocity measurements were split evenly above and below the mean. As such, a numerical average of the velocity data for each test is justified.

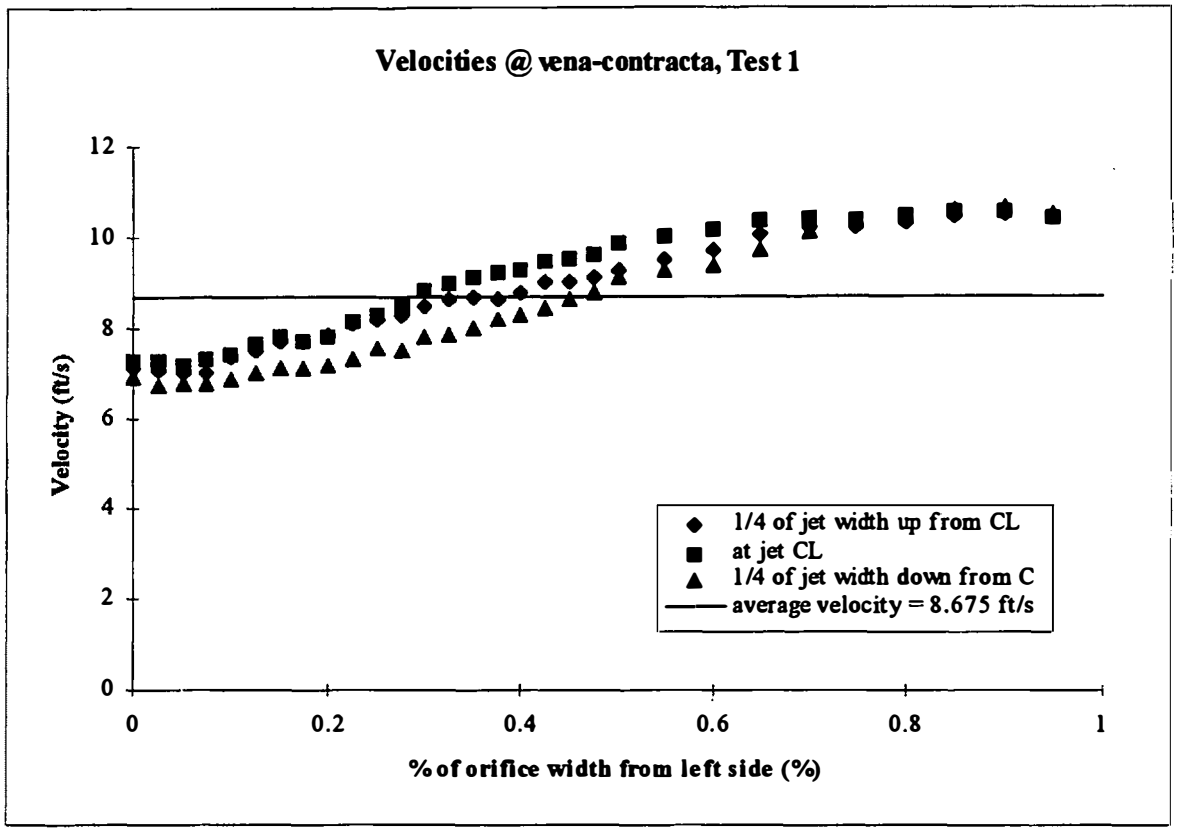

Figure D.1 Velocities @ vena-contracta, Test 1

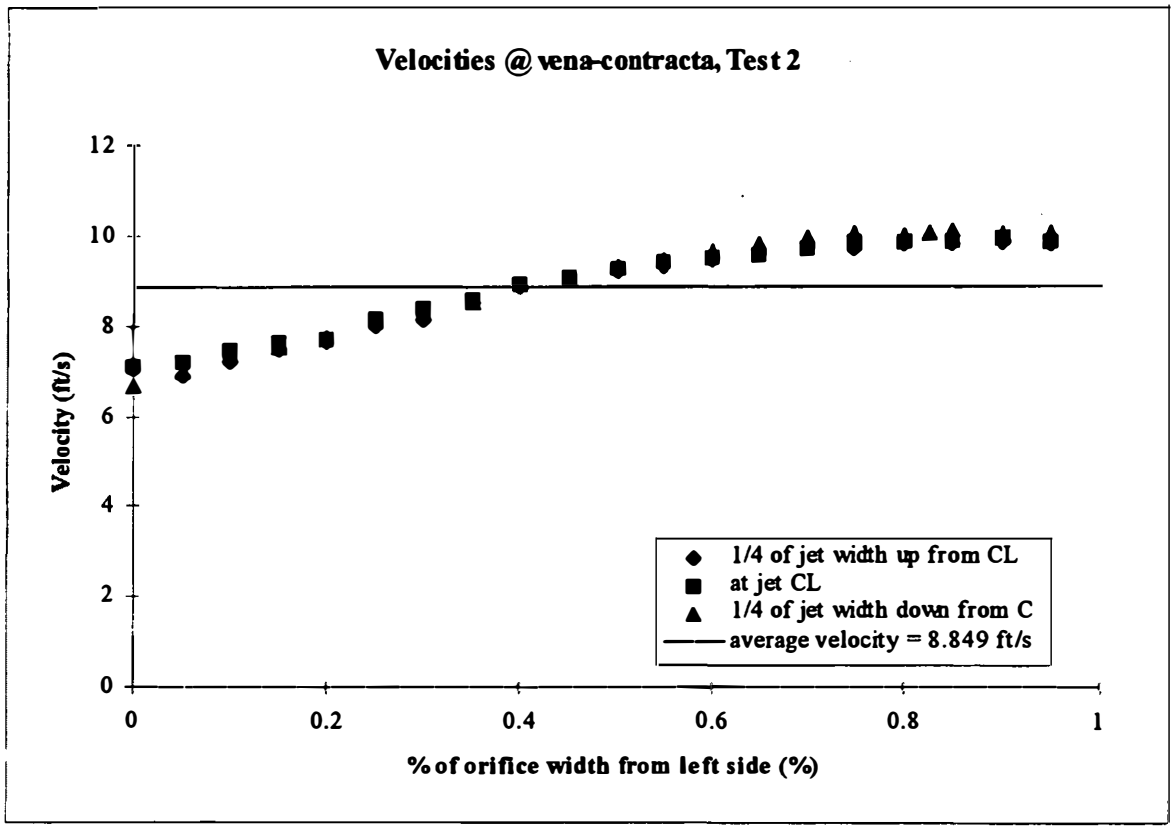

Figure D.2 Velocities @ vena-contracta, Test 2

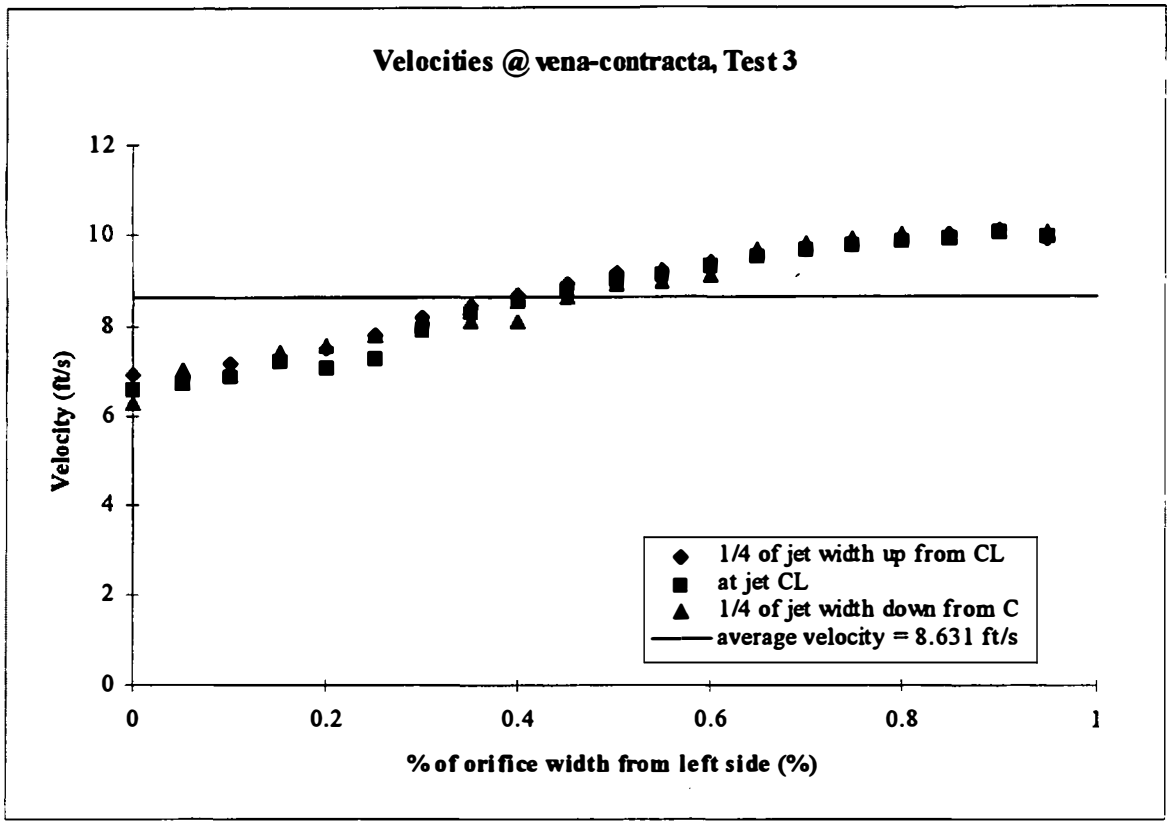

Figure D.3 Velocities @ vena-contracta, Test 3

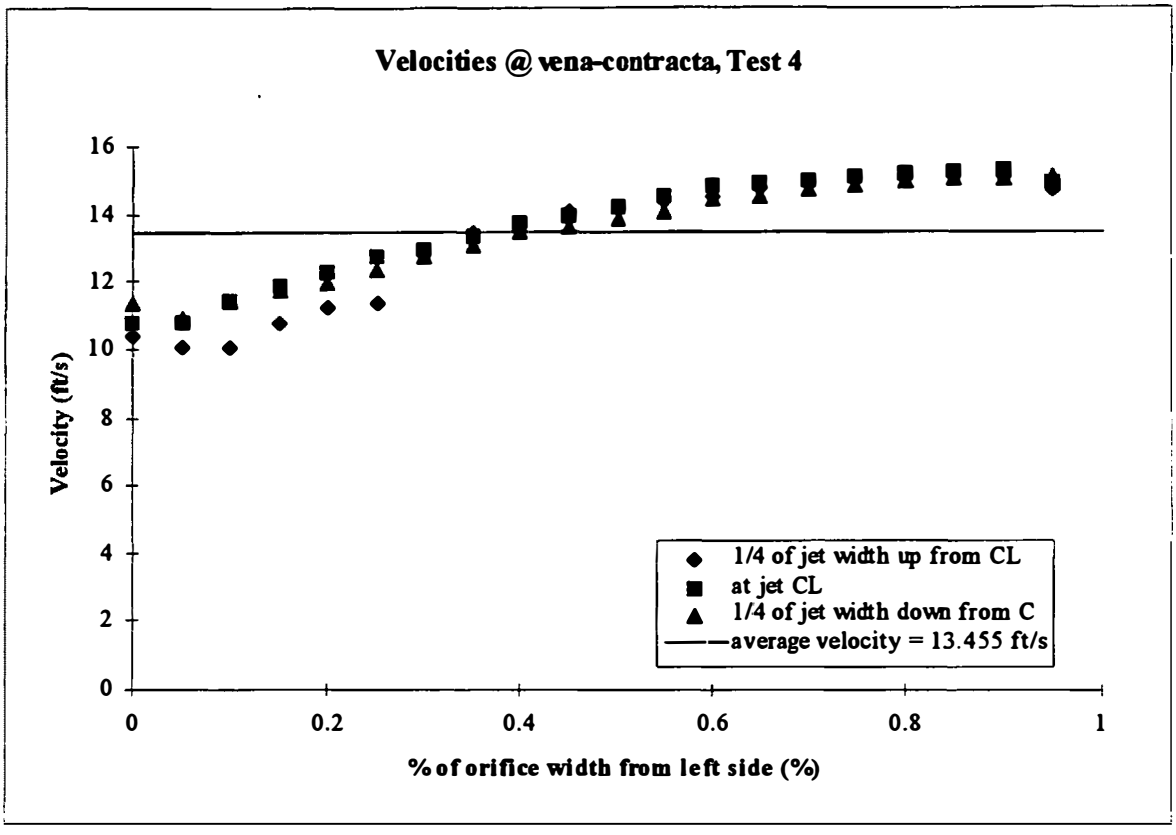

Figure D.4 Velocities @ vena-contracta, Test 4

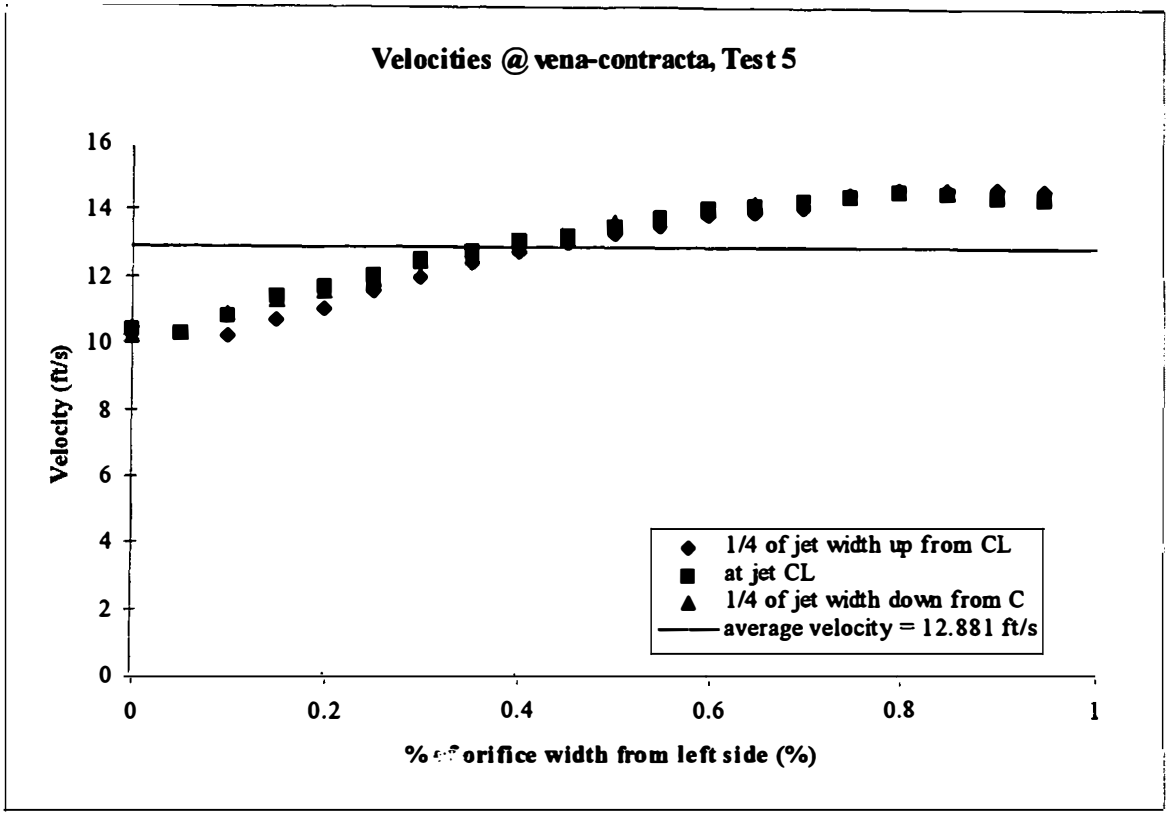

Figure D.5 Velocities @ vena-contracta, Test 5

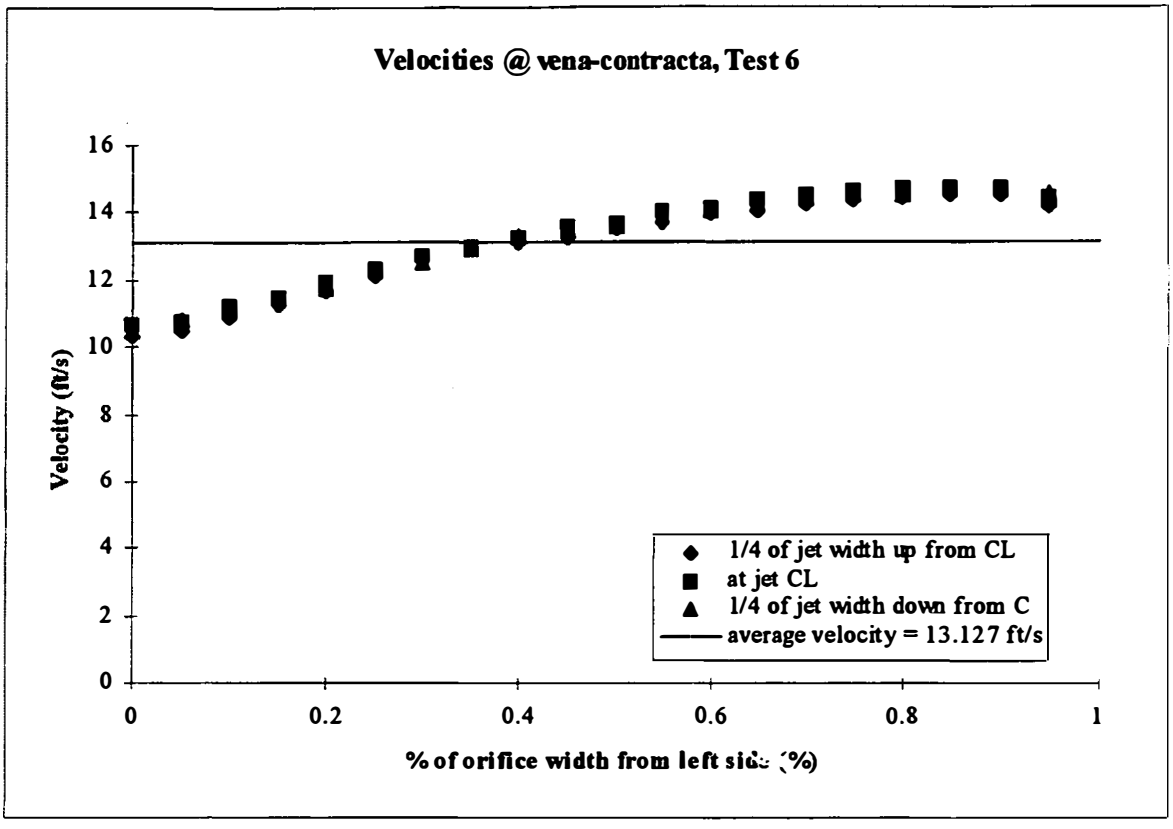

Figure D.6 Velocities @ vena-contracta, Test 6

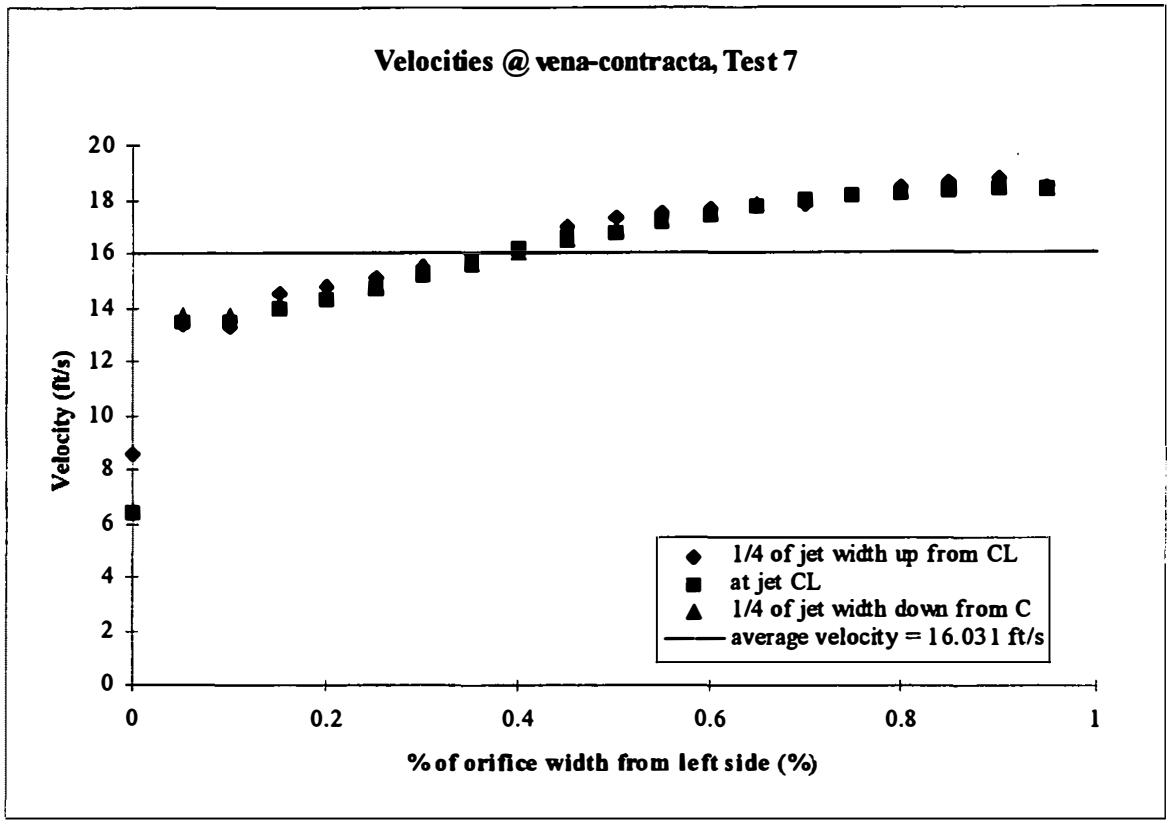

Figure D.7 Velocities @ vena-contracta, Test 7

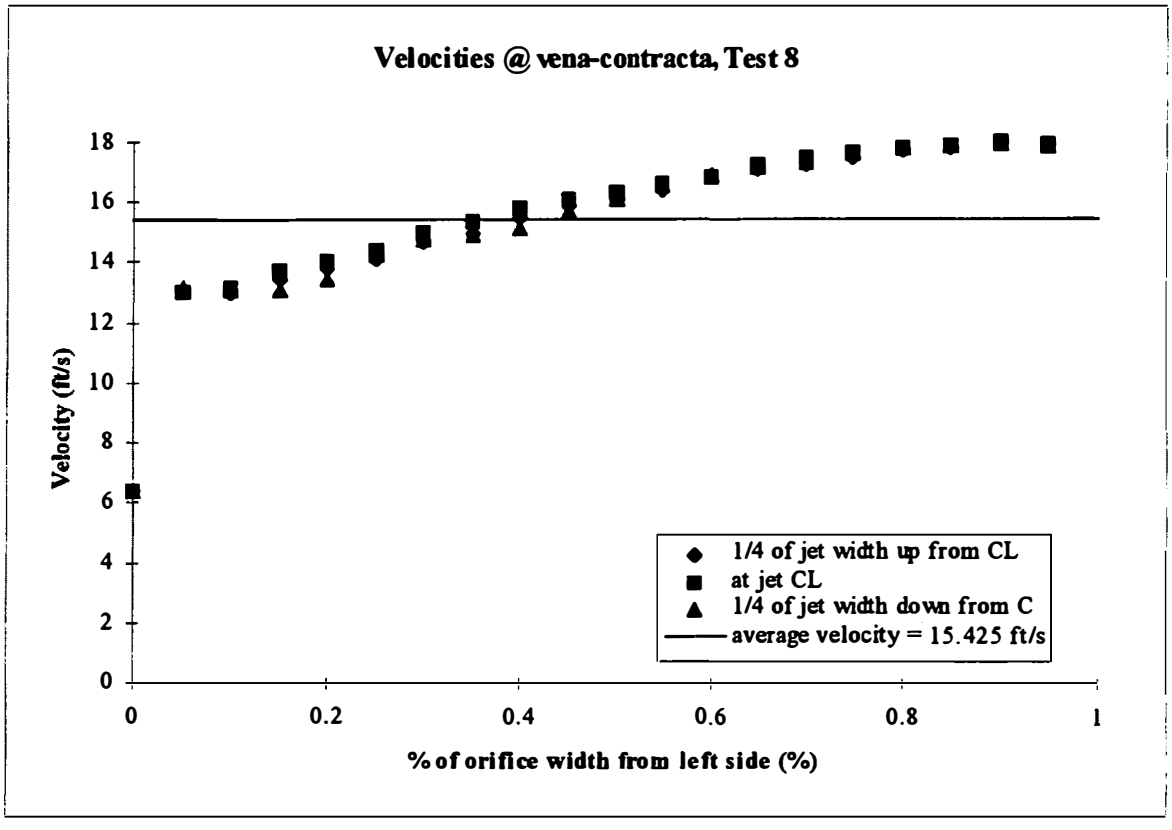

Figure D.8 Velocities @ vena-contracta, Test 8

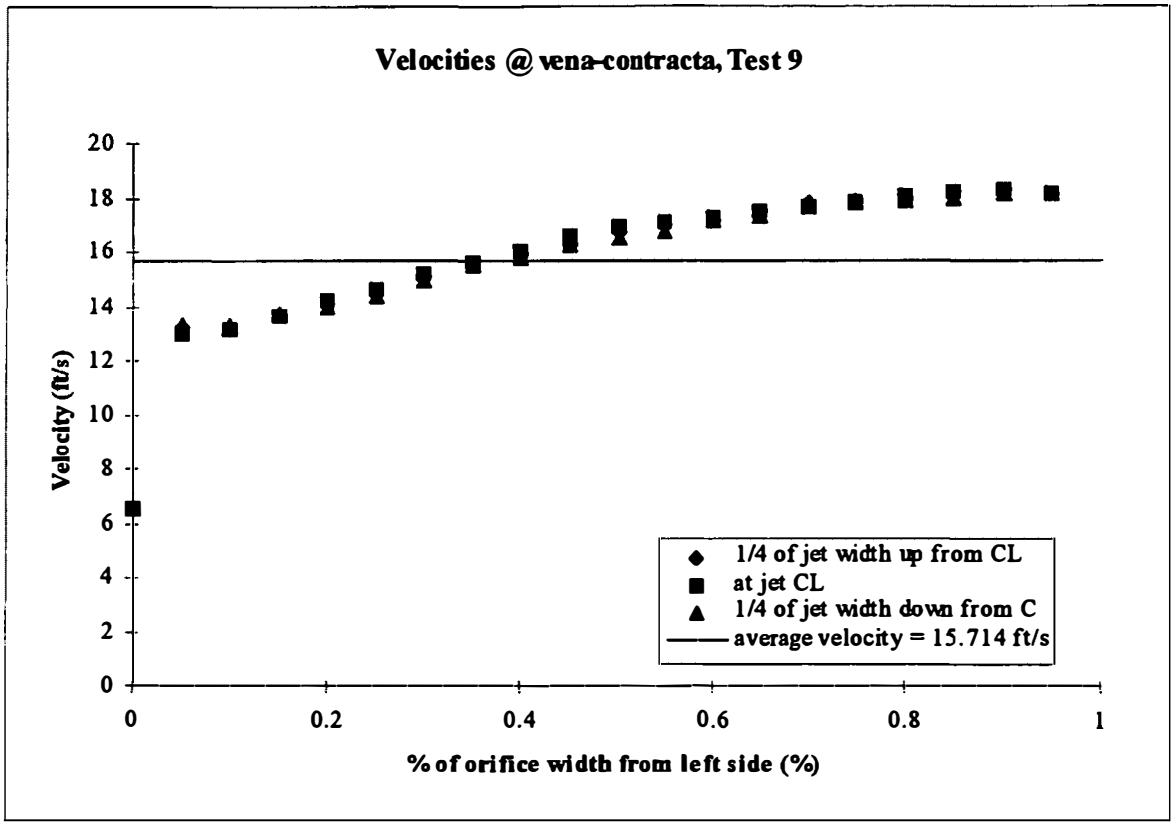

Figure D.9 Velocities @ vena-contracta, Test 9

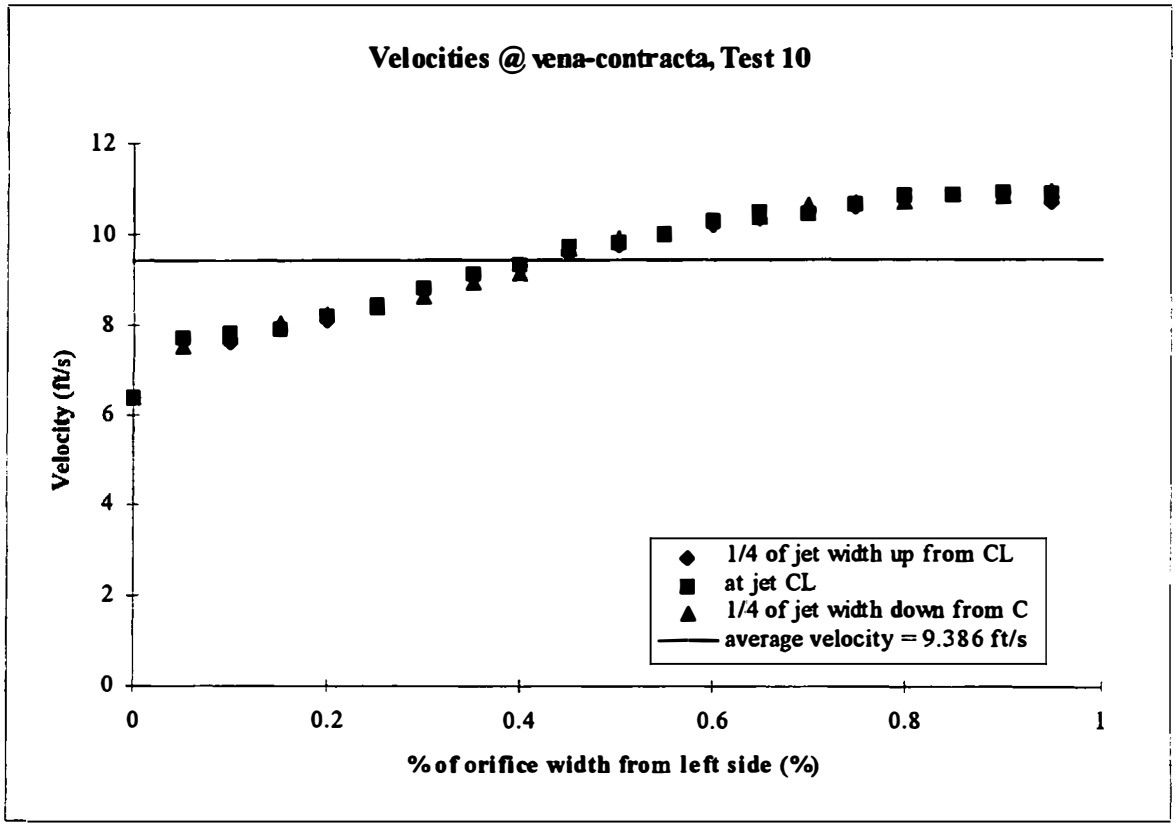

Figure D.10 Velocities @ vena-contracta, Test 10

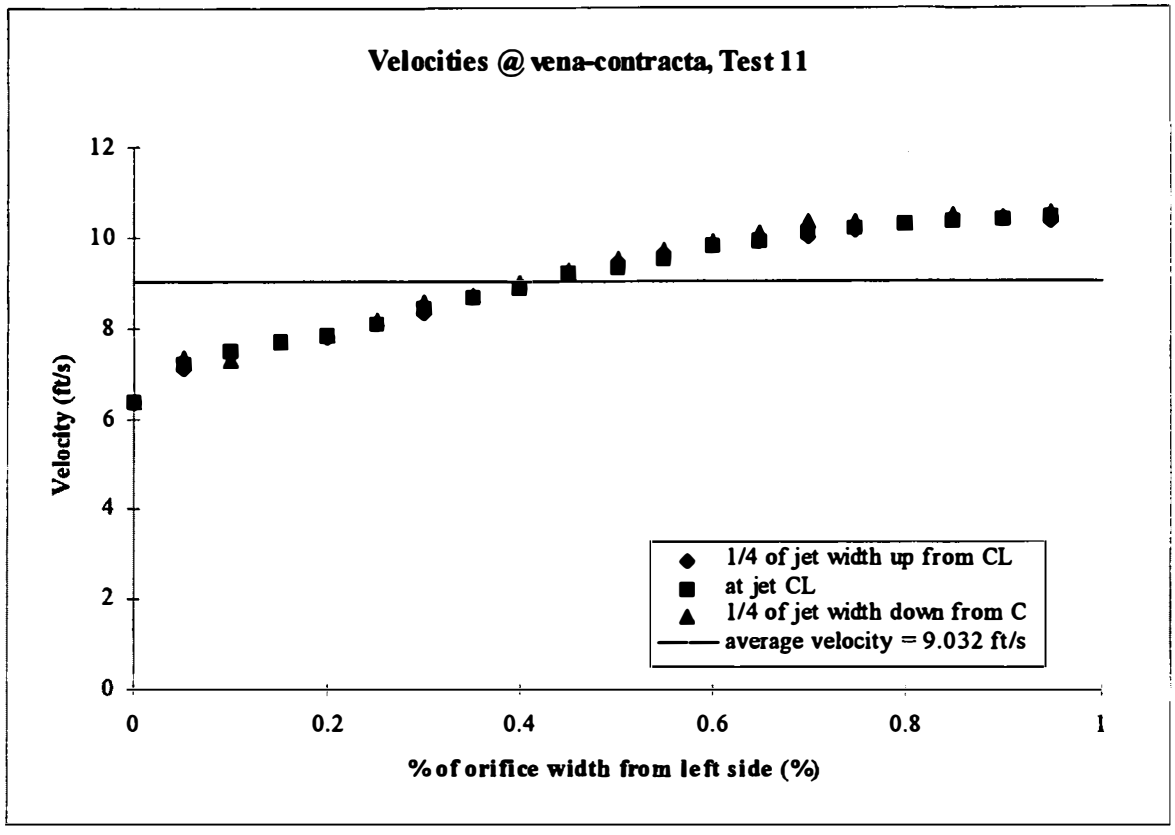

Figure D.11 Velocities @ vena-contracta, Test 11

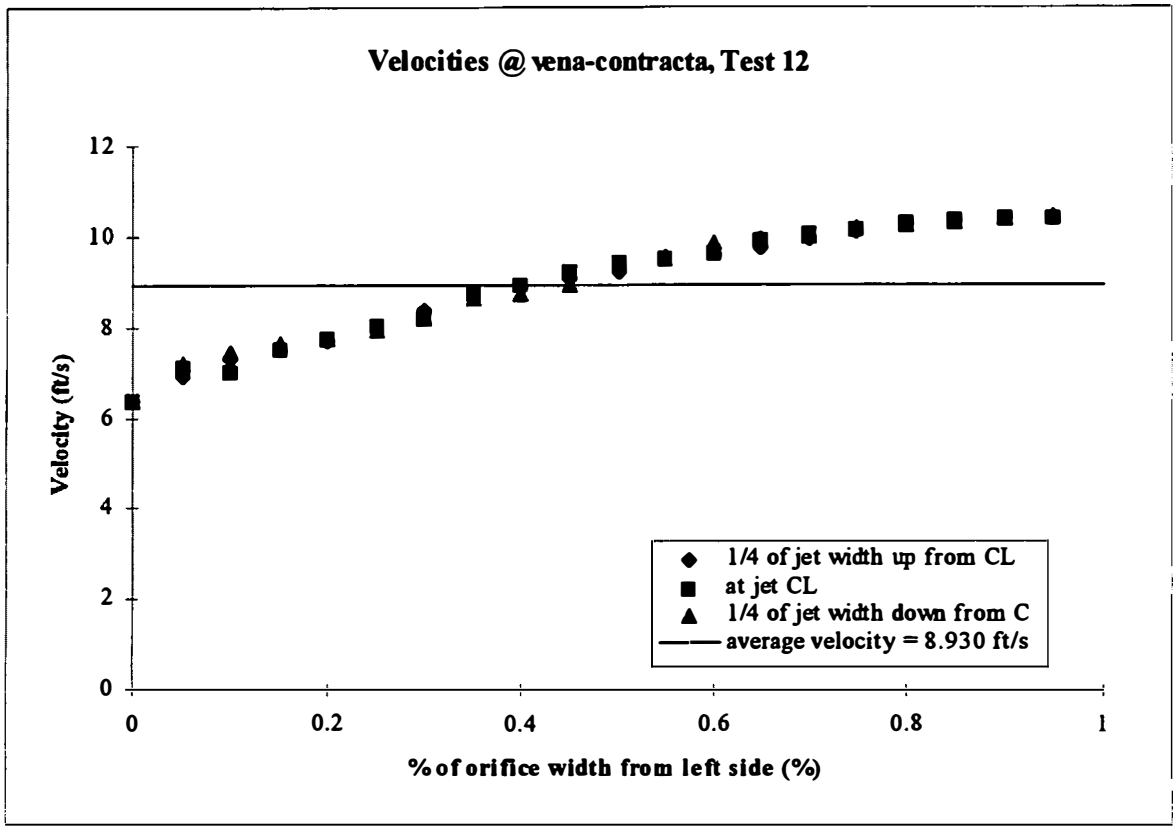

Figure D.12 Velocities @ vena-contracta, Test 12

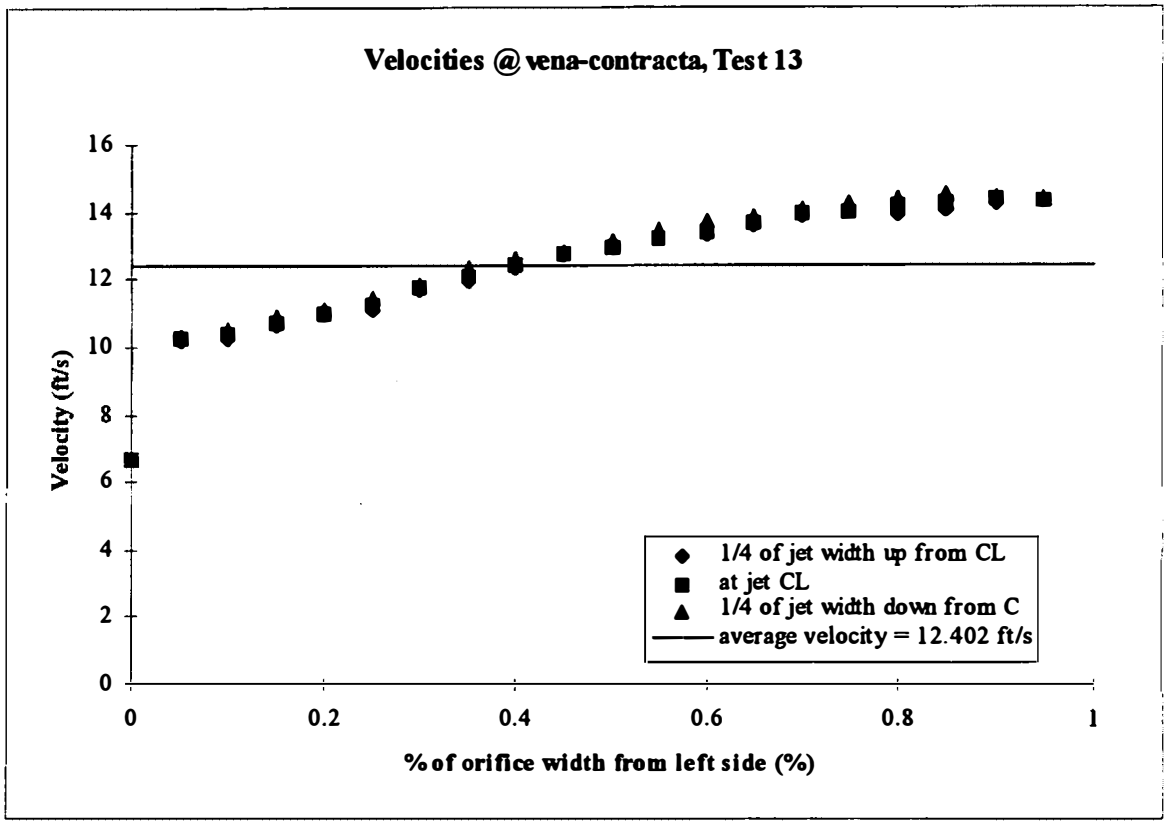

Figure D.13 Velocities @ vena-contracta, Test 13

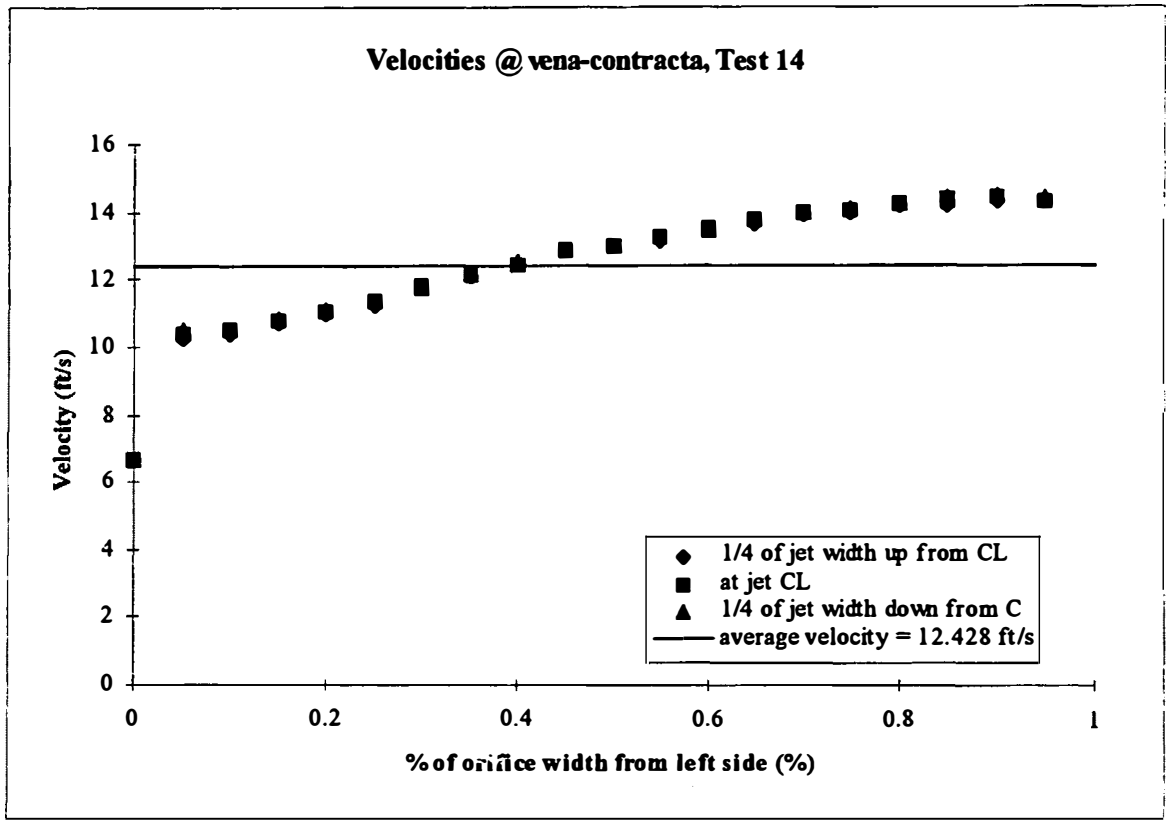

Figure D.14 Velocities @ vena-contracta, Test 14

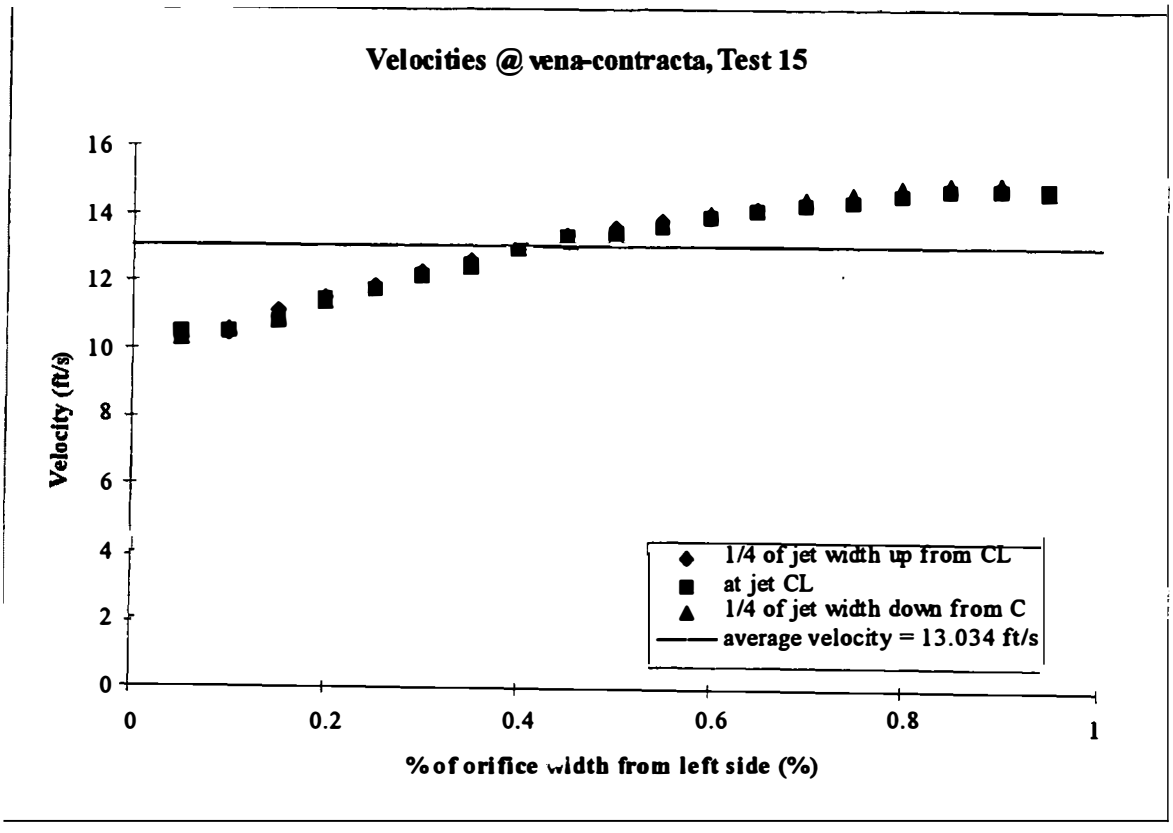

Figure D.15 Velocities @ vena-contracta, Test 15

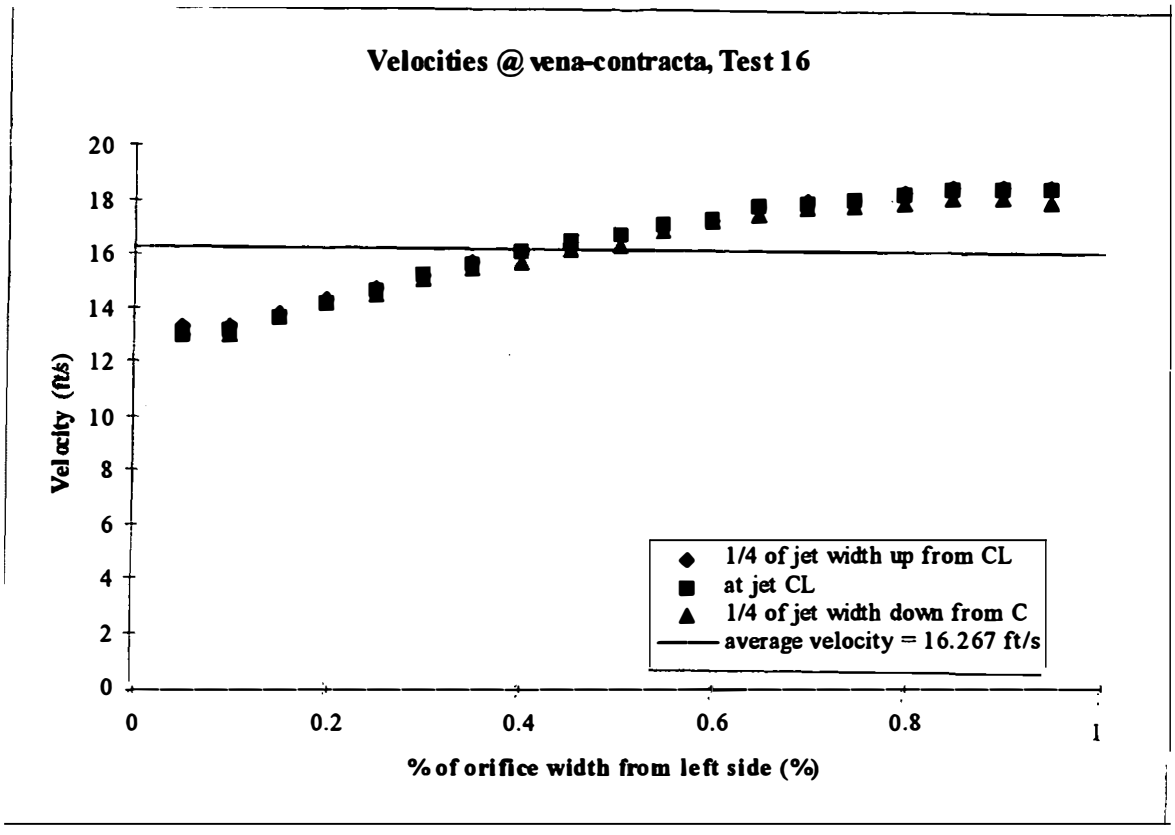

Figure D.16 Velocities @ vena-contracta, Test 16

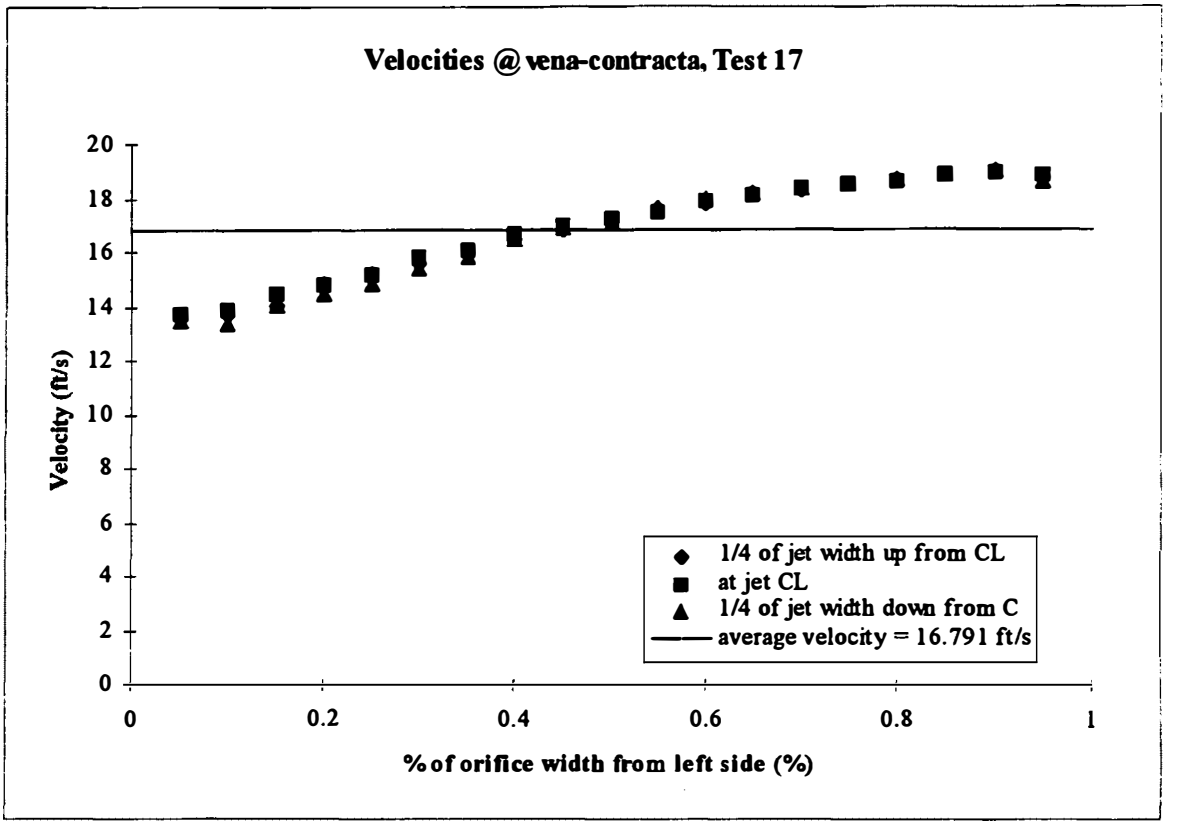

Figure D.17 Velocities @ vena-contracta, Test 17

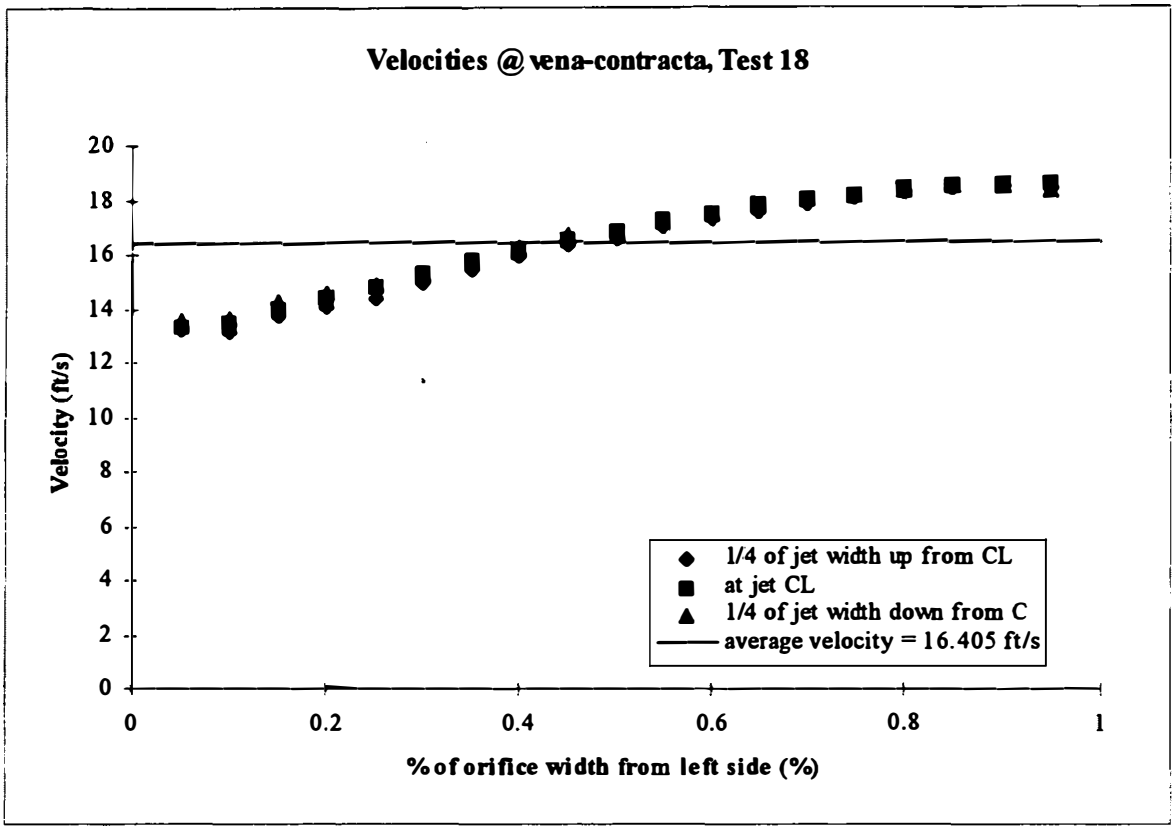

Figure D.18 Velocities @ vena-contracta, Test 18

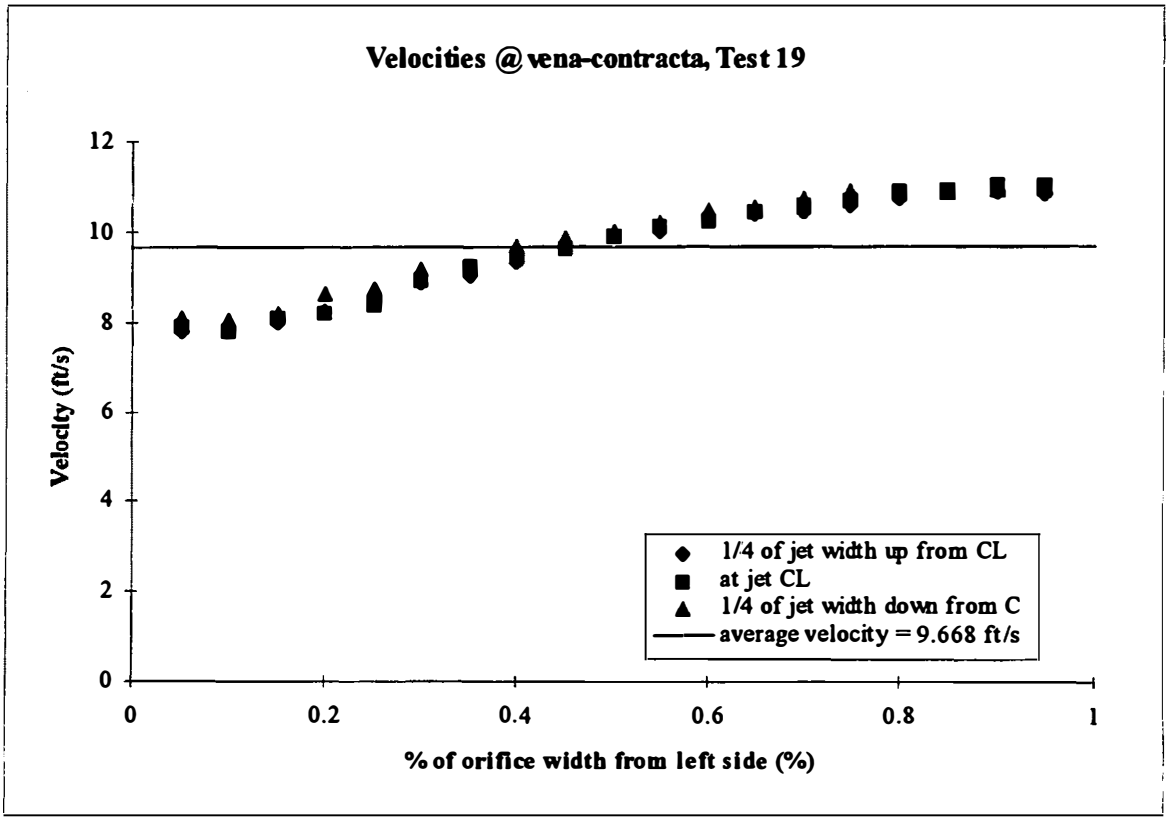

Figure D.19 Velocities @ vena-contracta, Test 19

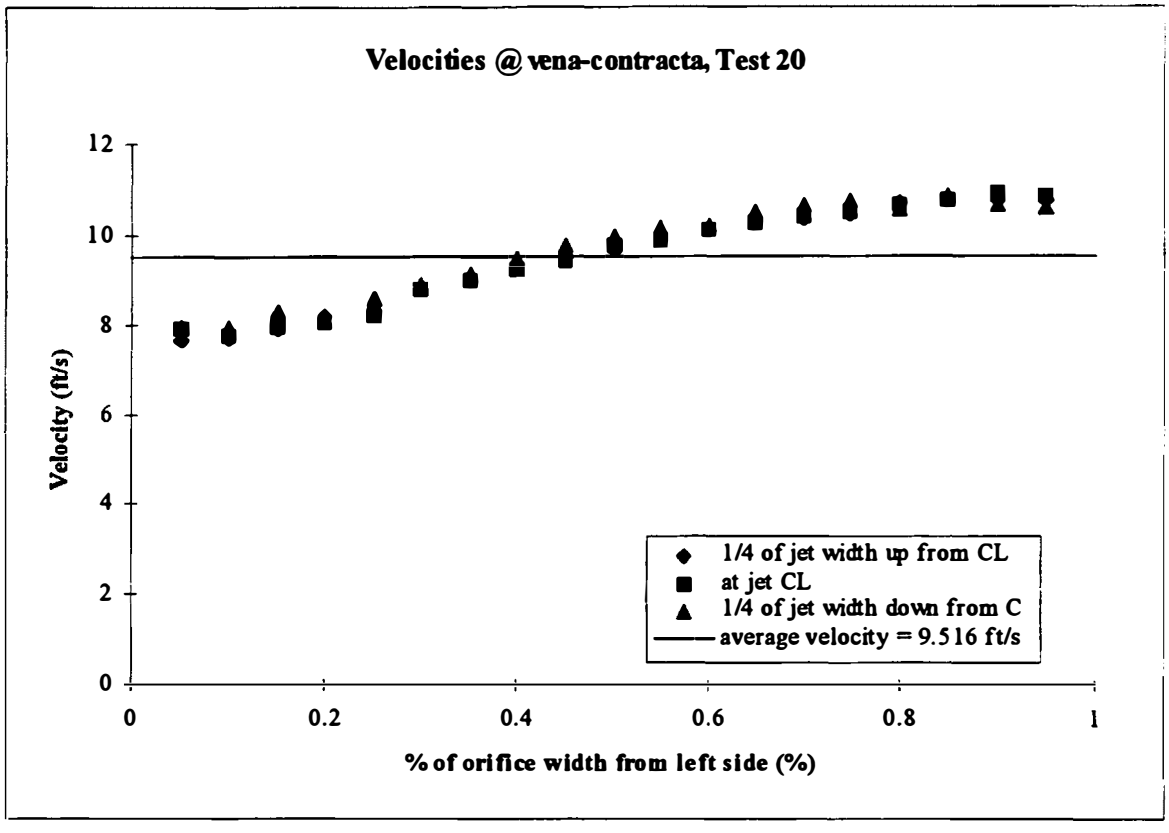

Figure D.20 Velocities @ vena-contracta, Test 20

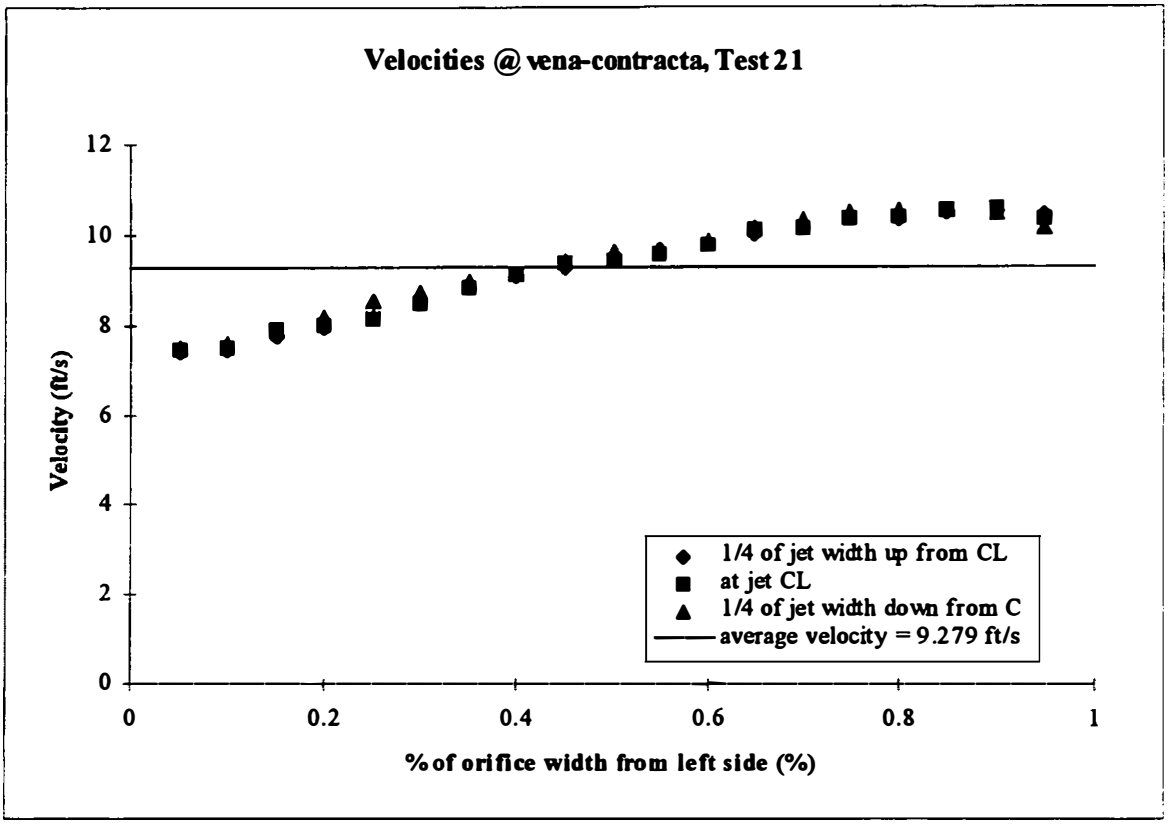

Figure D.21 Velocities @ vena-contracta, Test 21

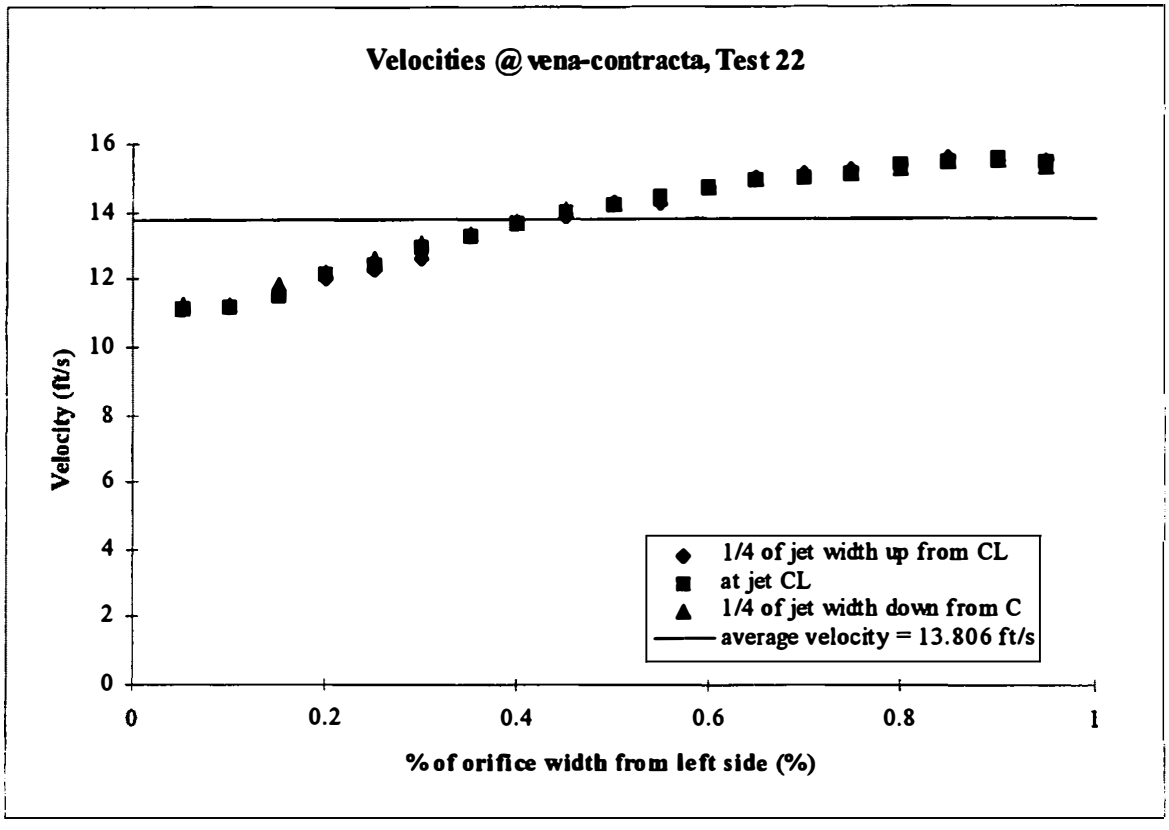

Figure D.22 Velocities @ vena-contracta, Test 22

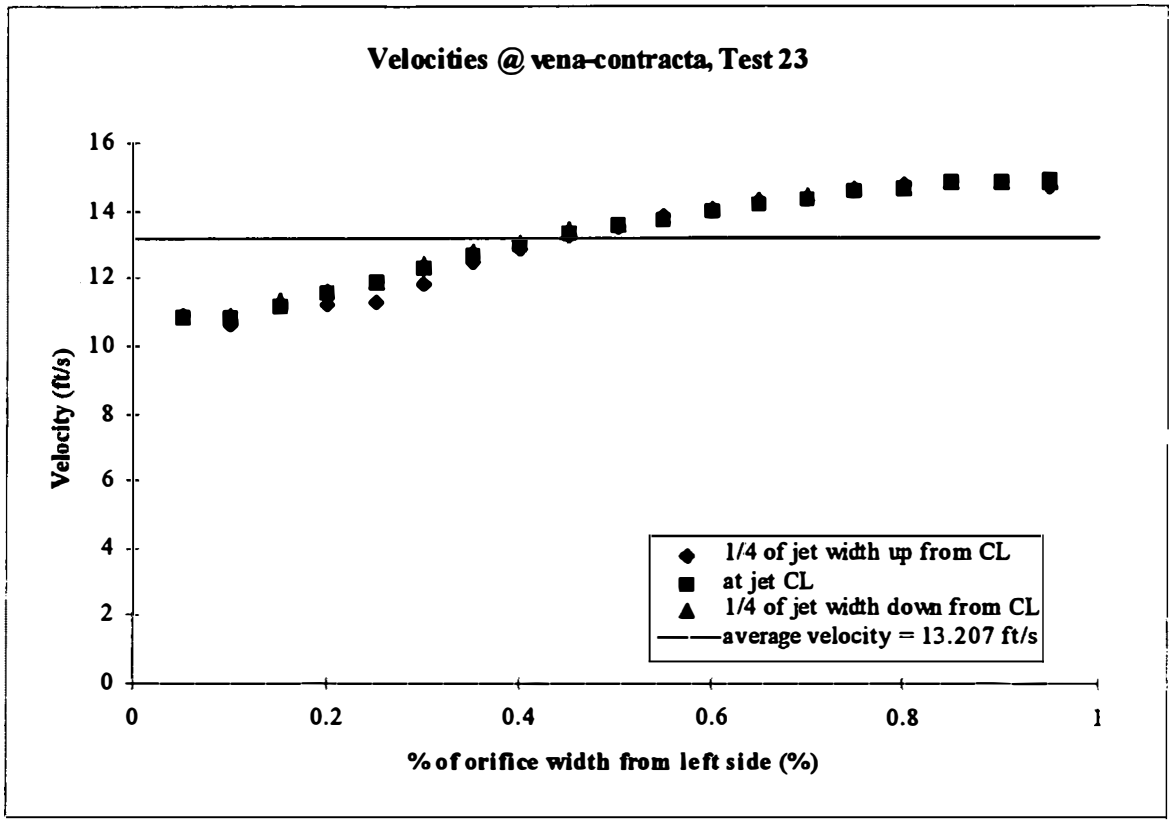

Figure D.23 Velocities @ vena-contracta, Test 23

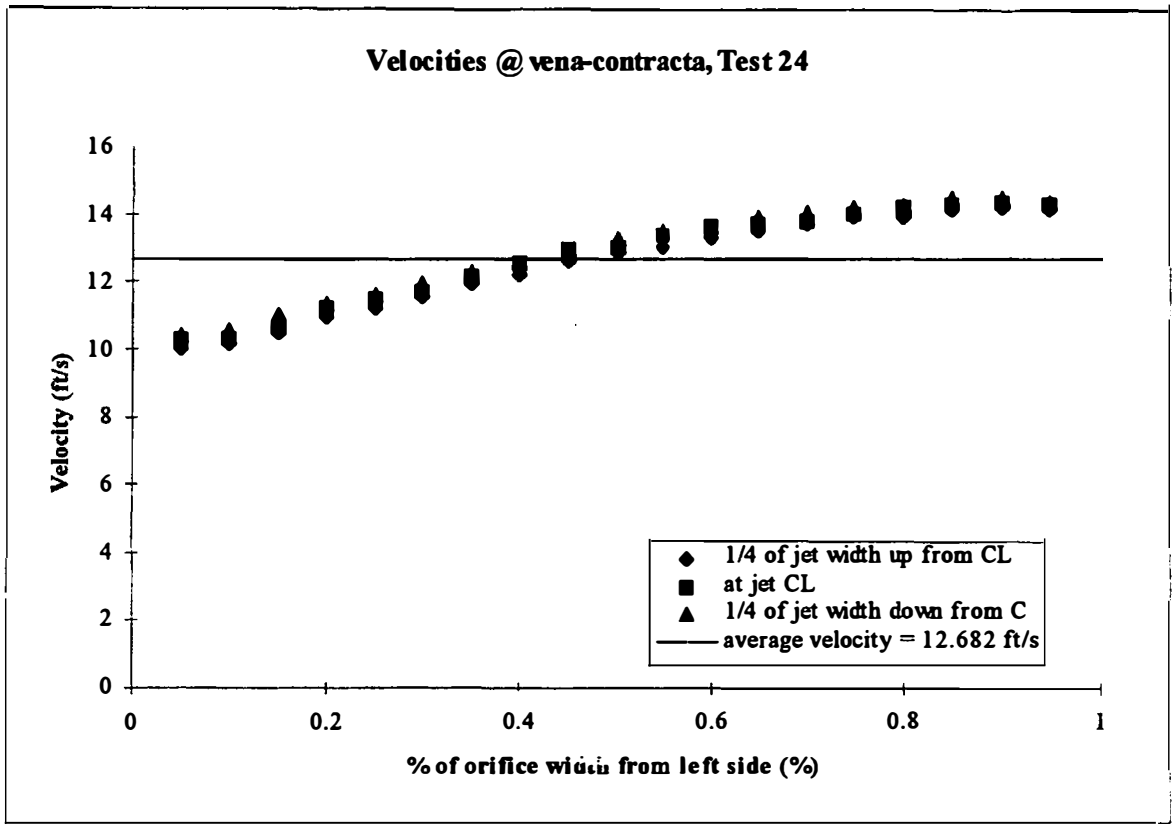

Figure D.24 Velocities @ vena-contracta, Test 24

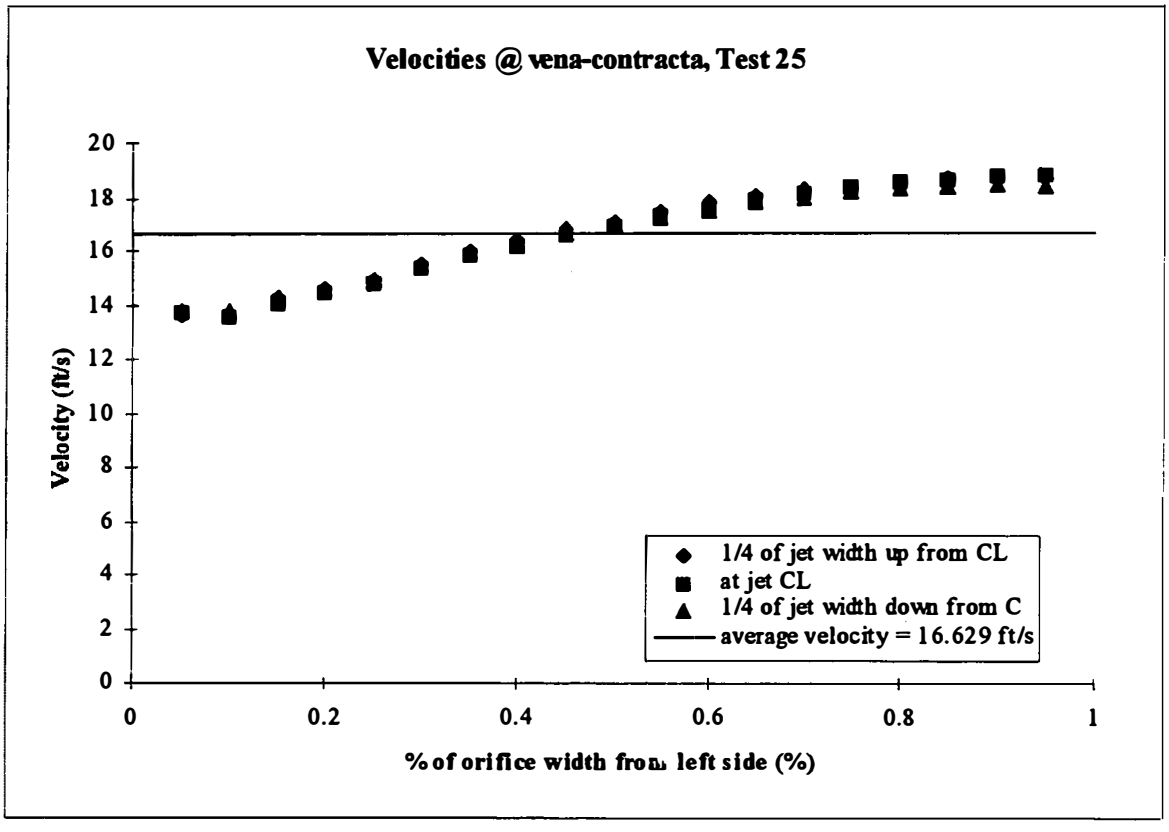

Figure D.25 Velocities @ vena-contracta, Test 25

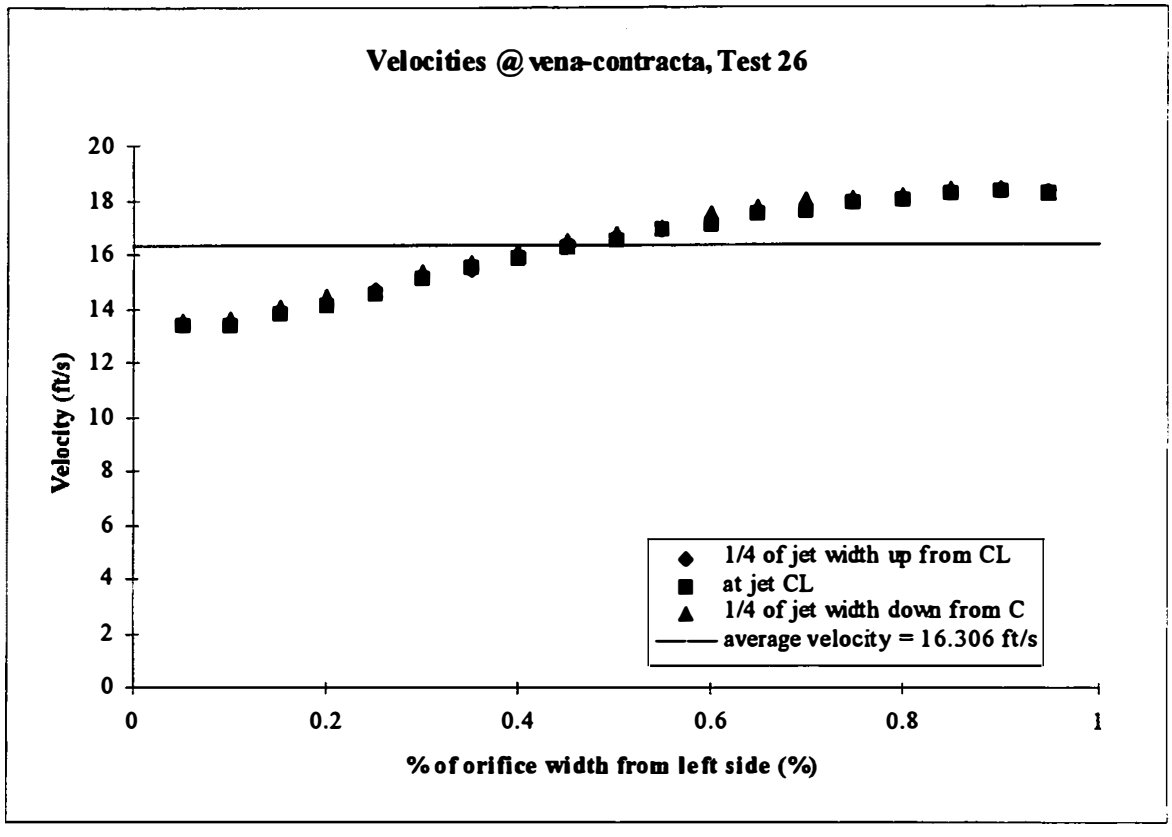

Figure D.26 Velocities @ vena-contracta, Test 26

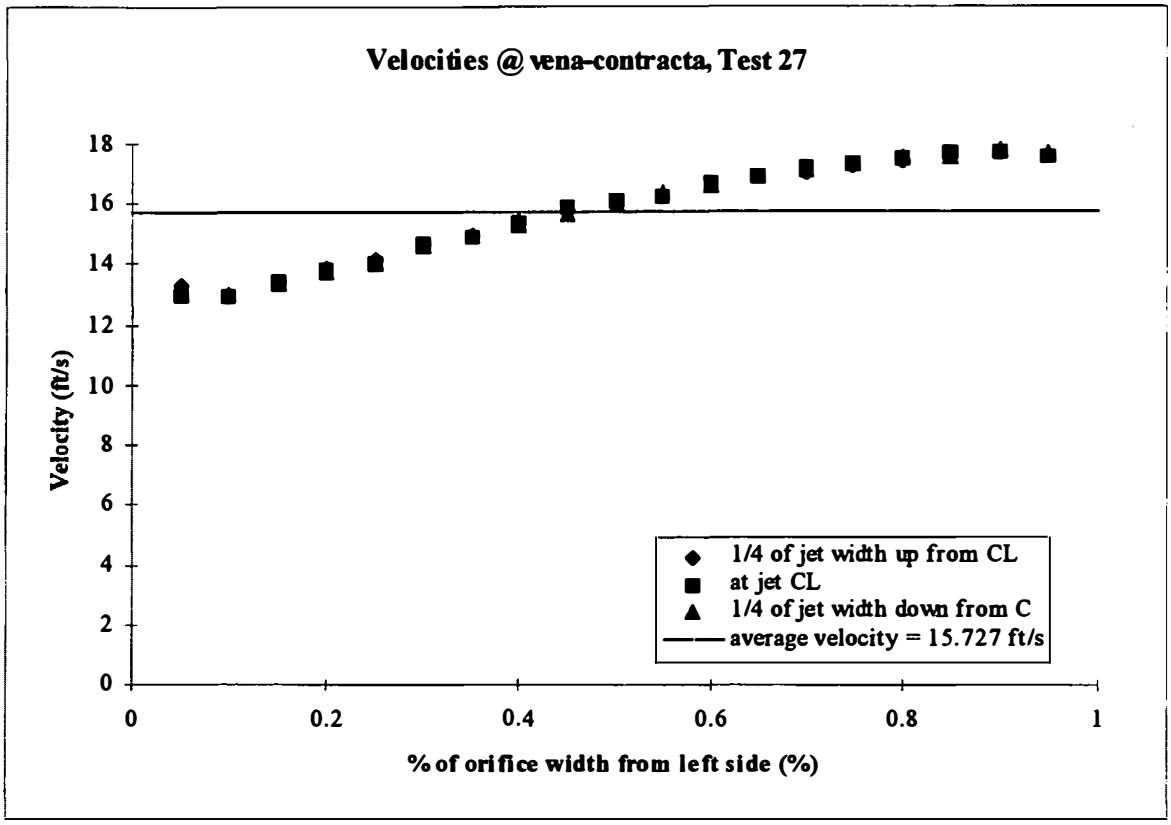

Figure D.27 Velocities @ vena-contracta, Test 27